

Precise Predictions for LHC Cross Sections and Phenomenology beyond NLO

Zur Erlangung des akademischen Grades eines
DOKTORS DER NATURWISSENSCHAFTEN
von der Fakultät für Physik des
Karlsruher Instituts für Technologie (KIT)

genehmigte

DISSERTATION

von

Dipl.-Phys. Robin Roth
aus Karlsruhe

Tag der mündlichen Prüfung: 30. Juni 2017

Referent: Prof. Dr. Dieter Zeppenfeld

Korreferent: Prof. Dr. Matthias Steinhauser

Abstract

Diboson production allows to study the interactions between electroweak bosons in the form of triple gauge couplings. A deviation of these interactions from the Standard Model can be parametrized by anomalous couplings in the framework of Effective Field Theory.

In this thesis, additional jet radiation in WZ and WH production is studied. The observable x_{jet} is introduced to distinguish jet-dominated events from those with two hard vector bosons. Using this observable, phase space regions sensitive to anomalous triple gauge couplings are identified and a dynamical jet veto is proposed to enhance the sensitivity of anomalous coupling searches. Compared to a traditional fixed- p_T jet veto, the dynamical veto avoids logarithms of the veto scale and includes, as a by-product, more relevant phase space. This increases the statistics and therefore improves the sensitivity in anomalous coupling searches. For an accurate description of high- p_T diboson events higher-order corrections are necessary. In this work, the LoopSim method is used to compute corrections at \bar{n} NLO in the strong coupling, which is an approximation to the full next-to-next-to-leading order calculation.

These analyses use the flexible Monte Carlo program `VBFNLO` interfaced to LoopSim. As part of this thesis, a parallel version of `VBFNLO` is implemented, which provides a step forward in the usability and speed of `VBFNLO` especially for complex processes by making better use of modern computing infrastructure.

Zusammenfassung

Die Produktion von Vektorbosonpaaren ermöglicht die Untersuchung der Wechselwirkung zwischen drei elektroschwachen Eichbosonen. Eine Abweichung dieser Kopplung von der Vorhersage des Standardmodells kann durch anomale Kopplungen im Formalismus von Effektiver Feldtheorie beschrieben werden.

In dieser Arbeit wird die zusätzliche Abstrahlung von Jets in WZ und WH Produktion untersucht. Hierfür wird die Observable x_{jet} eingeführt, um Events, die von Jet Abstrahlung dominiert werden, von solchen zu trennen, die zwei hochenergetische Vektorbosonen beinhalten. Mit dieser Observablen können Phasenraumbereiche identifiziert werden, die sensitiv sind auf anomale Kopplungen zwischen Eichbosonen. Zudem wird ein dynamisches Jet Veto vorgeschlagen, um die Sensitivität von Suchen nach anomalen Kopplungen zu erhöhen. Ein traditionelles Veto mit einer festen Skala führt zu logarithmisch wachsenden Termen, die durch ein dynamisches Veto vermieden werden können. Das dynamische Veto erlaubt weiterhin die Einbeziehung eines größeren Phasenraumbereichs. Dies verbessert die Statistik und damit die Empfindlichkeit von Suchen nach anomalen Kopplungen.

Für eine genaue Beschreibung der Events mit Vektorbosonpaaren mit hohen Transversalimpulsen sind Korrekturen höherer Ordnung notwendig. Im Rahmen dieser Arbeit wird die LoopSim Methode verwendet, um Korrekturen in \bar{n} NLO in der starken Kopplung zu berechnen. Dies ist eine Näherung der Korrekturen in nächst-zu-nächst-zu-führender Ordnung und besonders geeignet für hohe Transversalimpulse.

Diese Analysen nutzen das flexible Monte Carlo Programm `VBFNLO` in Verbindung mit LoopSim. In dieser Arbeit wird eine parallelisierte Implementierung von `VBFNLO` entwickelt, die insbesondere für komplexe Prozesse die numerische Integration und Laufzeit verbessert und moderne Rechencluster effizienter nutzt.

Contents

1. Introduction	1
2. Theoretical Foundations	5
2.1. The Standard Model of Particle Physics	5
2.2. Colliders and Cross Sections	8
2.2.1. Hadronic Cross Sections	8
2.3. Fixed Order Calculations	9
2.4. LoopSim	11
2.4.1. Matching and Merging	12
2.4.2. Contributions to Higher Order Corrections	12
2.4.3. LoopSim Algorithm	14
3. Anomalous Couplings	19
3.1. Effective Field Theory	19
3.1.1. Fermi Theory	20
3.1.2. Modern Applications of Top-Down Effective Field Theories	21
3.2. The Standard Model as an Effective Field Theory	22
3.3. Anomalous Couplings in the Gauge Boson Sector	23
3.3.1. The HISZ Basis	24
3.3.2. Mass Basis	25
3.4. Validity of Effective Field Theories	26
3.5. Interference and Squared Terms	26
3.6. Choice of Basis	28
3.7. Unitarity	29
4. Diboson Production	31
4.1. Experimental Status	31
4.1.1. LHC Experiments	31
4.1.2. Anomalous Couplings	33
4.2. Theoretical Status	33
4.2.1. Diboson Production	33
4.2.2. Previous LoopSim Analyses	34
5. Implementation in VBFNLO	37
5.1. Structure of VBFNLO	37
5.1.1. Monte Carlo Integration	38
5.1.2. Phase Space Generation	40
5.1.3. Amplitudes	41
5.2. Improving Numerical Stability	42
5.2.1. Enhancing Tails	42
5.2.2. Bin Smearing in VBFNLO and LoopSim	43

5.3. Random Number Generator	44
5.3.1. Choice of Random Number Generator	45
5.3.2. Quasi Random Numbers	45
5.4. Parallelization	46
5.4.1. Message Passing Interface	46
5.4.2. Parallelizing VEGAS	46
5.4.3. Design of the Implementation	47
5.4.4. Runtime Improvements to VEGAS and RNGs	49
5.4.5. Potential Improvements	52
5.5. Testing and Validation	52
5.6. Interface to Loopsim	55
6. Phenomenological Analysis	57
6.1. Computational Setup	57
6.2. Jets in Diboson Production	58
6.3. Distinguishing Dibosons from V+jet Production	62
6.3.1. Kinematical Variables	62
6.3.2. Lepton Separation Cut R_{ll}	65
6.3.3. Defining x_{jet}	66
6.3.4. Describing Jet Radiation in Diboson Production using x_{jet}	67
6.3.5. Applying x_{jet} to Anomalous Couplings	72
6.4. Jet Veto	73
6.4.1. Fixed Jet Veto	73
6.4.2. Dynamical Jet Veto	74
6.4.3. Jet Veto based on x_{jet}	75
6.5. Anomalous Couplings and \bar{n} NLO QCD in WZ Production	78
6.5.1. Numerical Setup	78
6.5.2. WZ production at \bar{n} NLO QCD	78
6.5.3. \bar{n} NLO QCD Corrections with Anomalous Couplings	78
6.5.4. Dynamical Jet Veto	81
7. Summary and Conclusion	85
Appendix	87
A. LoopSim events	87
Bibliography	91

Introduction

The nature of matter, its fundamental building blocks and their interactions have fascinated scientists already in ancient times. Modern particle physics is using high energy colliders to study elementary particles and their interactions. Currently, the Large Hadron Collider (LHC) at CERN in Geneva is pushing the energy and intensity frontier. In 2012, ATLAS and CMS, the two general-purpose experiments at LHC, discovered a scalar particle [1, 2], which within the current experimental accuracy has all properties of the Standard Model Higgs boson. The Standard Model (SM) contains Quantum Chromodynamics (QCD) [3–6], which describes the strong interaction between quarks and gluons, as well as the Glashow-Weinberg-Salam (GWS) theory of the electroweak interaction [7–10]. Through the Higgs mechanism [11–13] the electroweak symmetry is spontaneously broken and masses are generated. It also predicts a scalar particle, the Higgs boson, which was the last undiscovered elementary particle contained in the SM.

The SM continues to prove very successful in describing a wide range of particle physics experiments. It is tested to high precision for example in the measurement of the anomalous magnetic moment ($g - 2$) of electron and muon. These are both computed and measured to a few parts in a billion and trillion respectively [14, 15]. There is currently a tension of 3 – 4 standard deviations for ($g - 2$) of the muon [16] which might be a hint of physics beyond the SM.

In the search for new particles, hadron colliders are often considered *discovery machines*, since they have the highest reach in energy of all laboratory experiments. The LHC follows this path and surpasses the previously highest collision energies at the Tevatron by a factor of seven. Even at these high energies, until today, no particle outside of the SM was discovered. A broad range of searches are considered simultaneously. They can be roughly categorized as *direct searches* and *precision measurements/indirect searches*. Direct searches aim to measure the decay particles of a new resonance or a process that does not exist in the SM. Several search channels for particles beyond the SM showed a temporary excess over the expected background, like the 750 GeV resonance in photon pairs [17–20] or diboson pairs with an invariant mass of 2 TeV [21]. Searches for resonances typically look for bumps on top of a smooth background. This kind of analysis was for example used for the Higgs discovery in the decays to two photons [22, 23] or four leptons [24, 25]. In these channels the mass resolution is good enough to observe a peak coming from the Higgs boson resonance.

The other kind of searches for New Physics are precision measurements. Here, a SM process is studied with high precision with the aim to uncover small deviations from the prediction that could arise from New Physics models. Many precision measurements are performed at lepton colliders, where the background contributions are smaller. Despite the tremendous complexity,

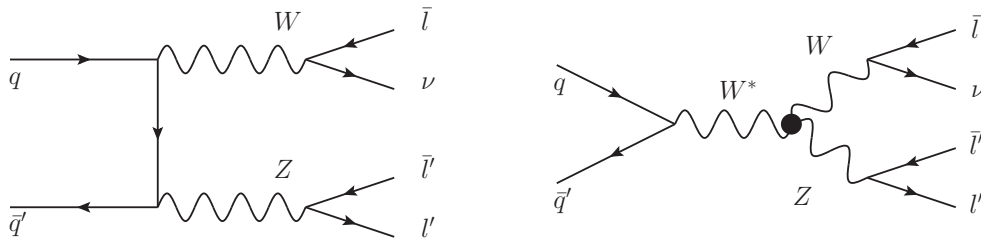


Figure 1.1: Representative diagrams for WZ production. This process allows to measure the WWZ triple gauge coupling by studying the kinematics of the events.

the LHC can provide high precision measurements for many processes down to the percent level, thanks to the significant effort of the experimental and theoretical communities.

One of the processes that experienced a drastic improvement in precision at the LHC is the production of two vector bosons. Example diagrams for WZ production, which will be studied in the following, are shown in Fig. 1.1. Leptonic decays can be used to tag events and discriminate against the background. When considering semi-leptonic decays, where one vector boson decays to hadrons and the other to leptons, a balance can be reached between background reduction via leptonic tags and larger branching ratios of the vector bosons to hadrons which improves the statistics. Diboson production is the process class with the highest cross section that gives access to triple gauge couplings, like in the diagram on the right of Fig. 1.1. These can be studied by measuring kinematical distributions of the final state. Especially sensitive are the region of large transverse momenta or decay angles, which carry information about the boson helicity.

Deviations in triple gauge couplings from the SM prediction can be described by anomalous couplings in the framework of Effective Field Theories (EFT). EFT is a general framework to model the low-energy effect of a theory at a high energy scale using operators with dimensionful couplings. There is a plethora of New Physics models. They often introduce new particles at a high energy scale to satisfy current experimental bounds. This separation of scales allows to apply EFT techniques for the low energy description.

Diboson production can set limits on anomalous coupling operators by studying events with high transverse momentum. These types of events benefit significantly from increases in the center of mass energy and luminosity, such that sizable improvements were achieved in LHC run 2 and more are expected for future LHC upgrades.

The theoretical description of these events needs to match at least the experimental precision to be able to detect deviations. This makes the calculation of higher order corrections in perturbation theory mandatory. The *next-to-leading order (NLO) revolution*, which made corrections available for many processes, reduced uncertainties typically down to the 10% level. Even higher order corrections are needed to match the experimental program and provide an accurate prediction for high-energy events. While results of full NNLO calculations are becoming available for a subset of processes, these calculations are technically extremely challenging and out of reach for some process classes, like the production of three massive vector bosons. LoopSim [26] is a general approach to approximate NNLO corrections by combining NLO calculations of processes for several final state jet multiplicities. This resulting prediction is called \bar{n} NLO. The accuracy of LoopSim can be assessed by comparing the \bar{n} NLO calculation to existing NNLO calculations and then applying LoopSim to processes where the full calculation does not exist.

The LoopSim method in combination with the flexible Monte Carlo program VBFNLO [27–29] allows to calculate observables for diboson production at high precision. Leptonic decays and off-shell effects are included. Furthermore, VBFNLO allows to calculate effects of anomalous couplings and experimental selection cuts and custom observables can be implemented.

Diboson events with high transverse momenta are often accompanied by additional jets. These can reduce the sensitivity to anomalous coupling effects and lead to large corrections. In this thesis additional jets in WZ and WH production are studied and a measure of the jet activity is introduced. Using this analysis, events with additional radiation can be suppressed to improve anomalous coupling searches. Higher order corrections are required for an accurate description of additional radiation. Since these corrections can be of comparable size as the impact of anomalous couplings, their interplay is of interest.

This thesis is organized as follows: In Chapter 2 the theoretical foundations will be introduced, including the Standard Model, fixed order calculations and LoopSim (Section 2.4). Chapter 3 will discuss anomalous couplings using the EFT formalism and their application to triple gauge couplings in diboson production. The current experimental and theoretical state of diboson production is reviewed in Chapter 4. The calculation is implemented in VBFNLO, which is introduced in Chapter 5 including the technical modifications like improved statistics in tails (Section 5.2) and a new random number generator used for the parallelization of the Monte Carlo integration (Sections 5.3 and 5.4). The calculation is used to study the phenomenology of WH and WZ production in Chapter 6. The focus is on improving the sensitivity to anomalous couplings by better understanding additional jet radiation. A dynamical jet veto is introduced and studied including LoopSim corrections.

Theoretical Foundations

Predictions for processes at particle collider experiments can be calculated using quantum field theory. Section 2.1 will introduce the Standard Model (SM) of particle physics and in Section 2.2 the calculation of cross sections at hadron colliders will be discussed. These calculations are performed to a fixed order in perturbation theory, which is described in Section 2.3. The LoopSim method, introduced in Section 2.4, is used to approximate higher order corrections.

2.1. The Standard Model of Particle Physics

The SM describes our current knowledge of elementary particles and their interactions. As all quantum field theories, it is defined by its field content and symmetries.

The interactions are determined by gauge symmetries. The gauge symmetry group of the SM is

$$SU(3)_C \times SU(2)_L \times U(1)_Y. \quad (2.1)$$

The group $SU(3)_C$ corresponds to Quantum Chromodynamics (QCD) [3–6], which describes the strong interaction between quarks and gluons, governed by the coupling constant α_s . QCD shows confinement, which means that all color-charged particles form color singlet bound states. The QCD coupling α_s depends on the renormalization scale μ_R , which should be the typical energy scale of the process [30, 31]:

$$\mu_R^2 \frac{\partial \alpha_s}{\partial \mu_R^2} = \beta(\alpha_s), \quad (2.2)$$

$$\beta(\alpha_s) = -\alpha_s^2 \left(b_0 + b_1 \alpha_s + b_2 \alpha_s^2 + \dots \right), \quad (2.3)$$

$$b_0 = \frac{11C_A - 4T_R n_f}{12\pi} = \frac{33 - 2n_f}{12\pi}. \quad (2.4)$$

The running depends on the constants C_A and T_R given by the gauge group and the number of active quark flavors n_f . At high energies the QCD coupling constant becomes small (*asymptotic freedom*) and allows to calculate amplitudes in perturbation theory, which will be considered in Section 2.3. For small energies α_s grows and in a perturbative description diverges around $\Lambda_{\text{QCD}} \approx 0.2 \text{ GeV}$ [31]. Therefore, for small energies the resulting physics has to be described non-perturbatively.

The group $SU(2)_L \times U(1)_Y$ describes the electroweak interaction as given by the Glashow-Weinberg-Salam (GWS) theory [7–10]. The electromagnetic force is mediated by the photon, the weak force is mediated by the W and Z bosons.

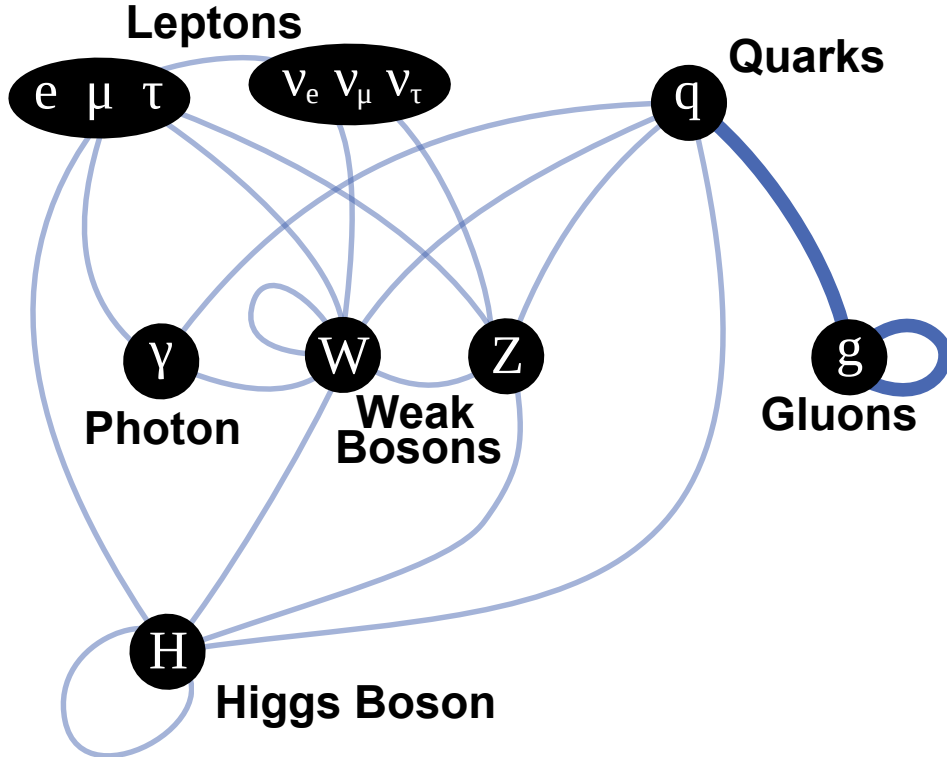


Figure 2.1: The particle content and interactions of the SM are shown in a simplified graph. The focus of this thesis is on the interaction of the W and Z boson. For the production of WZ pairs, higher order corrections in QCD (bold line) will be considered. Inspired by [32]

The fermion fields in the SM are quarks and leptons. Quarks are charged under $SU(3)_C$ and form hadrons, like the proton, while leptons do not interact under the strong interaction. There are right- and left-handed fields. Right-handed fields are singlets under $SU(2)_L$, while the left-handed fields are in a doublet.

The fermion fields are therefore

$$\begin{pmatrix} u \\ d \end{pmatrix}_L, u_R, d_R, \quad \begin{pmatrix} \nu_e \\ e \end{pmatrix}_L, e_R, \nu_R. \quad (2.5)$$

For each field, there are three generations: $u \rightarrow c, t$, $d \rightarrow s, b$, $e \rightarrow \mu, \tau$, $\nu_e \rightarrow \nu_\mu, \nu_\tau$. A simplified visualization of the field content and interactions can be seen in Fig. 2.1.

The coupling of the fermion fields to the electroweak gauge fields is given by the Lagrangian density

$$\mathcal{L}_{\text{fermion}} = \sum_j \bar{\Psi}_j i \not{D} \Psi_j, \quad (2.6)$$

where j sums over all right- and left-handed fermion fields Ψ_j and D_μ is the covariant derivative

$$D_\mu = \partial_\mu - ig' B_\mu \frac{Y}{2} - ig W_\mu^a T^a. \quad (2.7)$$

B_μ and W_μ^a are the gauge fields of $U(1)_Y$ and $SU(2)_L$ with couplings g' and g respectively. The generators of $SU(2)_L$ are $T^a = \frac{\sigma^a}{2}$ with the Pauli matrices σ^a for the doublet fields. The corresponding terms for right-handed fields have $T^a = 0$.

The kinetic terms for the gauge fields are

$$\mathcal{L}_{\text{EW}} = -\frac{1}{4}W_{\mu\nu}^a W^{a\mu\nu} - \frac{1}{4}B_{\mu\nu}B^{\mu\nu}, \quad (2.8)$$

with the field strength tensors

$$W_{\mu\nu}^a = \partial_\mu W_\nu^a - \partial_\nu W_\mu^a + g\epsilon^{abc}W_\mu^b W_\nu^c, \quad (2.9)$$

$$B_{\mu\nu}^a = \partial_\mu B_\nu^a - \partial_\nu B_\mu^a. \quad (2.10)$$

Spontaneous Symmetry Breaking

A direct mass term for the gauge bosons would violate the gauge symmetry. Instead, the Higgs mechanism is used to generate masses for the W and Z bosons.

The Higgs Lagrangian with the Higgs doublet Φ is

$$\mathcal{L}_H = (D_\mu \Phi)^\dagger (D^\mu \Phi) - V(\Phi), \quad (2.11)$$

$$V(\Phi) = \mu^2 \Phi^\dagger \Phi + \lambda (\Phi^\dagger \Phi)^2. \quad (2.12)$$

The Higgs potential leads to spontaneous symmetry breaking if $\lambda > 0$ and $\mu^2 < 0$. In this case the potential has a Mexican hat shape and the minimum of the potential is at a non-vanishing field value, called the vacuum expectation value,

$$v = \sqrt{\frac{-\mu^2}{2\lambda}}. \quad (2.13)$$

While the potential has $SU(2)_L \times U(1)_Y$ symmetry, the selection of the ground state spontaneously breaks the symmetry. The field Φ can be expanded around vacuum expectation value and three of its degrees of freedom can be absorbed by a gauge transformation, such that

$$\Phi = \frac{1}{\sqrt{2}} \begin{pmatrix} 0 \\ v + h \end{pmatrix}. \quad (2.14)$$

The kinetic term for the Higgs boson then generates interactions between gauge bosons and the Higgs as well as masses for the gauge bosons:

$$(D_\mu \Phi)^\dagger (D^\mu \Phi) = (v + h)^2 \left(\frac{g^2}{4} W_\mu^\dagger W^\mu + \frac{g^2}{8 \cos^2 \theta_W} Z_\mu Z^\mu \right) + \dots \quad (2.15)$$

The charge and mass eigenstates of the gauge bosons are

$$\begin{aligned} W_\mu^\pm &= \frac{1}{\sqrt{2}} (W_\mu^1 \mp iW_\mu^2), \\ Z_\mu &= \frac{1}{\sqrt{g^2 + g'^2}} (gW_\mu^3 - g'B_\mu), \\ A_\mu &= \frac{1}{\sqrt{g^2 + g'^2}} (g'W_\mu^3 + gB_\mu). \end{aligned} \quad (2.16)$$

The definition of Z_μ, A_μ is a rotation of W_μ^3, B_μ by the angle

$$\cos \theta_W = \frac{g}{\sqrt{g^2 + g'^2}}. \quad (2.17)$$

Gauge Boson Interactions

Expanding the kinetic terms of the gauge bosons leads to gauge boson self-interactions with triple and quartic couplings. Considering only the WWZ interaction, the terms are

$$\begin{aligned} -\frac{1}{4}B_{\mu\nu}B^{\mu\nu} - \frac{1}{4}W_{\mu\nu}^a W^{a\ \mu\nu} = & -ie \cot \theta_W \left[(\partial^\mu W^\nu - \partial^\nu W^\mu) W_\mu^\dagger Z_\nu \right. \\ & - (\partial^\mu W^{\nu\dagger} - \partial^\nu W^{\mu\dagger}) W_\mu Z_\nu \\ & \left. + W^\mu W^{\nu\dagger} (\partial_\mu Z_\nu - \partial_\nu Z_\mu) \right] + \dots \end{aligned} \quad (2.18)$$

A comprehensive review of the SM and its interactions can be found in e.g. [33, 34].

2.2. Colliders and Cross Sections

Processes involving elementary particles can be studied at colliders. The motivation to use particle colliders is to maximize the center of mass energy of the collision. The high center of mass energy is needed to produce heavy new states and study the high-energy behavior of processes. A high rate is needed to see rare processes.

There are different types of colliders, depending on which particles are brought into collision. The main ones use electrons or protons and their antiparticles. Colliders are typically either linear or circular. Circular colliders allow the reuse of the collided particles, but lead to synchrotron radiation due to the bending of the particle beam. The power loss due to synchrotron radiation is

$$\Delta E \propto \frac{\gamma^4}{R}, \quad (2.19)$$

with γ the Lorentz boost of the accelerated particles and R the ring radius. At a given energy, heavy particles (protons) are less boosted than light ones (electrons) and thus experience less power loss due to synchrotron radiation. This allows to accelerate them to higher energies. The LHC is a proton-proton collider running currently at $\sqrt{s} = 13$ TeV, while in the same ring the Large Electron-Positron Collider (LEP) accelerated electrons and positrons only up to $\sqrt{s} = 209$ GeV.

2.2.1. Hadronic Cross Sections

The experiments at the LHC record final states of collisions. A measurement then refers to the number of events that pass certain selection criteria. The rate \dot{N} , with which a given process occurs, can be split into a process dependent and a machine dependent part:

$$\dot{N} = \sigma \mathcal{L}. \quad (2.20)$$

σ is the cross section and \mathcal{L} the luminosity. The cross section can be calculated from theory. It depends on the selected final state particles. After including the detector acceptance and analysis cuts, it is called *fiducial* cross section. The luminosity does not depend on the

processes, but only on machine parameters. For a collider with N_b bunches in both beams which revolve with frequency f and contain N particles each that are spatially distributed in a Gaussian profile of width σ_x, σ_y the luminosity is

$$\mathcal{L} = \frac{N^2 f N_b}{4\pi\sigma_x\sigma_y}. \quad (2.21)$$

To get a number of events instead of a rate, the integrated luminosity is used,

$$L_{\text{int}} = \int \mathcal{L} dt. \quad (2.22)$$

The LHC has a design luminosity of $\mathcal{L} = 1 \cdot 10^{34} \text{ cm}^{-2}\text{s}^{-1}$. In 2016 it delivered an integrated luminosity of $L_{\text{int}} = 41 \text{ fb}^{-1}$ [35].

Parton Distribution Functions

At the LHC the colliding particles are protons, which are not elementary, but QCD bound states. At the LHC energies, their constituents are resolved, such that the *hard process* is a collision including quarks and gluons. The mapping between protons and their partons is determined by non-perturbative QCD and can not be calculated using perturbation theory. It is parametrized by *Parton Distribution Functions* (PDF). These are probability density functions $f_i(x, Q^2)$ that depend on the type of parton i , the momentum fraction of the proton which the parton carries, x , and the energy scale Q^2 .

The hadronic cross section can then be factorized as

$$\sigma_{pp \rightarrow \text{fin}} = \sum_{i,j} \int dx_1 dx_2 f_i(x_1, Q^2) f_j(x_2, Q^2) \sigma_{ij \rightarrow \text{fin}}. \quad (2.23)$$

The indices i and j refer to the partons: g, u, d, \dots . The PDFs are parametrized and fitted to measurements by different groups [36–38].

The hard cross section can be calculated from the underlying quantum field theory as

$$\sigma = \int d\Phi_n \frac{1}{2\hat{s}} \overline{|\mathcal{M}|^2}. \quad (2.24)$$

Here, $\frac{1}{2\hat{s}}$ is the flux factor, $d\Phi_n$ is the phase space integration and $\overline{|\mathcal{M}|^2}$ the matrix element describing the initial-final transition averaged over the initial state spins and summed over the final state spins.

2.3. Fixed Order Calculations

Since exact solutions to the SM are not known for general processes, the usual approach to calculate amplitudes is the use of perturbation theory. In this approach one splits the Lagrangian into a free theory, for which freely propagating particles are the solution, and interactions between these particles, which are perturbations described by small coupling constants. Quantities like cross sections can be expanded as a series in the couplings and each order of this expansion can be calculated individually. The first non-vanishing term is

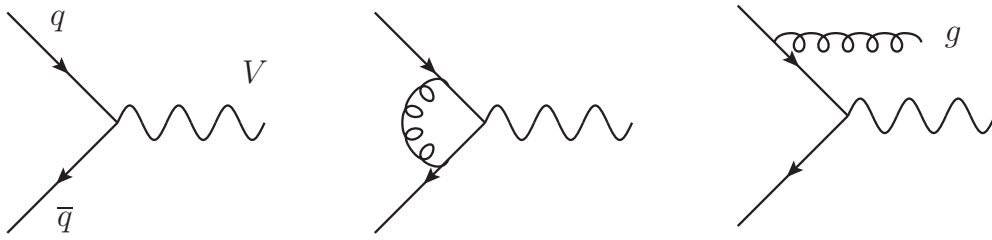


Figure 2.2: LO and NLO amplitudes for single vector boson production in a $q\bar{q}$ collision. At NLO there is either an additional loop (center) or an additional emission (right).

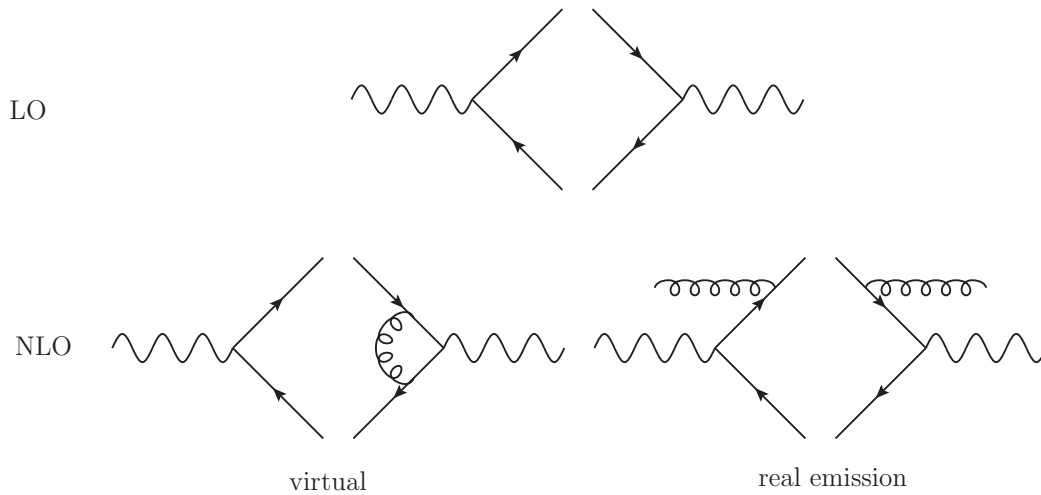


Figure 2.3: Visualization of squared amplitudes at LO (top) and NLO (bottom). Virtual corrections appear as interference with the Born amplitude and real corrections as a square of the amplitude with one additional emission.

called *leading order* (LO). The next term is *next-to-leading order* (NLO) and so forth (NNLO, $N^3\text{LO}$, ...).

The amplitude is calculated using the Feynman diagram approach. Here the series expansion is visible in the number of couplings in the diagram. The LO amplitude is also called *Born* amplitude. Often, like in diboson production, the LO amplitude is described by a tree-level diagram. But there are also processes where the LO amplitude has a loop, for instance Higgs production via gluon-fusion.

At NLO there are two different types of higher order corrections: real emission and virtual corrections. Real emission corrections have one additional external particle compared to the LO process, while virtual corrections add an additional loop.

For the minimal example of single vector boson production the contributing diagrams are shown in Fig. 2.2. At the amplitude level, there is a triangle loop (vertex correction) for the virtual corrections and an additional emission from one of the quark legs for the real emission. The cross section is calculated as an integral over the squared amplitude, which is visualized in Fig. 2.3. For a NLO calculation, terms with up to one additional factor of α_s are considered. At this order, the one-loop amplitude enters as the interference with the Born amplitude, while the real emission amplitude appears squared.

When calculating these corrections, divergences appear in the calculation. Special treatment of these divergences is needed, such that all physical observables have finite results.

The divergences can be categorized in two regions. UV divergences correspond to large momenta in loops and can be regularized using for example dimensional regularization and can then be absorbed in parameters of the theory using renormalization. Furthermore, there are divergences for small momenta in loops and for soft or collinear emissions in real emission amplitudes. These are called IR divergences and can be understood as the on-shell limit of an intermediate massless propagator. If a massless quark emits a gluon, the corresponding amplitude contains a quark propagator, such that the squared amplitude will be

$$|\mathcal{M}| \propto \frac{1}{p_{\text{emitter}}^2} \propto \frac{1}{p_g \cdot p_q} \propto \frac{1}{E_q E_g (1 - \cos \theta)}, \quad (2.25)$$

where p_q, p_g (E_q, E_g) are the momenta (energies) of the final quark and gluon and θ the angle between them. In the last term, the divergent kinematical configurations can be extracted. The term diverges if the emission is soft ($E_g \rightarrow 0$) or collinear ($\theta \rightarrow 0$).

These IR divergences can also be regularized using dimensional regularization. In total cross sections the regularized divergences can be canceled analytically. This cancellation always works for IR safe observables as stated by the Kinoshita-Lee-Nauenberg (KLN) theorem [39, 40].

When calculating differential cross sections, the cancellation can in general not be performed analytically. Instead, a numerical procedure is used. The most common approach is to use a subtraction scheme. To accomplish this, a term is constructed with the same divergence structure as the real emission. In contrast to the real emission, in the subtraction term the divergent phase space of the additional emissions can be integrated analytically. Thus it can be added back to the virtual corrections. For a process with n particles at LO and $n + 1$ in the real emission the contributions to the NLO cross section are:

$$\begin{aligned} \sigma_{\text{NLO}} &= \sigma_B + \int_n d\sigma_V + \int_{n+1} d\sigma_R \\ &= \sigma_B + \int_n \left(d\sigma_V + \int_1 d\sigma_A \right) + \int_{n+1} (d\sigma_R - d\sigma_A). \end{aligned} \quad (2.26)$$

This construction is possible, due to the factorization of the IR divergences, which means that a $(n + 1)$ configuration in the soft or collinear limit can be written as a product of the (n) particle amplitude multiplied with a universal (process independent) divergent factor.

Different realizations of the subtraction algorithm exist. In the Monte Carlo program VBFNLO, which is used for the numerical calculations in this thesis, the *Catani-Seymour* dipole subtraction [41, 42] is applied. The idea is that the divergences are given by the Born process with an additional splitting attached. This splitting is described using dipole terms. When integrating out the emitted particle a third particle has to be involved, such that momentum is conserved while keeping all particles on their mass shell. This additional particle is called *spectator*.

2.4. LoopSim

The LoopSim method was introduced in the paper ‘‘Giant QCD K-factors beyond NLO’’ [26]. The goal is to describe processes, which receive sizeable corrections at higher order due to additional emissions. While LoopSim can be applied at different orders, the most common case is to approximate NNLO corrections of a process X , by combining the NLO calculations

(abbreviated as $X@NLO$) with the NLO corrections to the process with an additional jet ($X+j@NLO$). The resulting description by LoopSim is called $X@nNLO$. For this combination, a method is needed to merge samples of different multiplicities without double counting contributions. The main idea is to use unitarity, such that the fully inclusive NLO cross section is preserved and the sample with additional emissions only modifies distributions and fiducial cross sections, but not the fully inclusive cross section. LoopSim works purely numerically on the level of events.

2.4.1. Matching and Merging

In recent years many algorithms with similar aims as LoopSim were developed. They all use common building blocks. Most of them aim at combining fixed order calculations of different jet multiplicities with parton showers. Fixed order calculations are an expansion in the coupling up to a fixed power in the coupling and, thus, a fixed number of additional emissions. A parton shower gives a description of many emissions, for which the leading logarithmic terms of QCD are considered. When both are combined, double counting has to be avoided by adjusting the phase space filled by the parton shower and the fixed order calculation, while loosing neither the fixed-order accuracy nor the leading-log accuracy. This procedure is called *matching*.

Fixed order calculations for different jet multiplicities can be combined to give a better description of events with multiple emissions. This combination is called *merging*. It was first applied to LO calculations, but can be extended to include higher order corrections. LoopSim is a parton-level merging procedure. It uses fixed order calculations of different multiplicities to produce a combined sample. In contrast to many other recent merging methods, LoopSim is not connected to a parton shower and can work directly with parton-level Monte Carlo programs.

VBFNLO itself is a parton level generator and does not include a parton shower or matching/merging. Nevertheless, it can be interfaced to other Monte Carlo programs, which implement matching and merging. The interface of fixed-order amplitudes to parton shower Monte Carlo programs is standardized in Binot-Houches-Accord (BLHA) [43, 44] as a collaborative effort of many Monte Carlo program authors. Using this interface VBFNLO was used in combination with Herwig to investigate parton shower effects on vector boson fusion processes [45]. Using this interface also NLO merging can be performed in Herwig using a new NLO merging scheme [46] available in Herwig 7.1. An overview of the Monte Carlo programs, merging schemes and their recent developments can be found e.g. in [47].

2.4.2. Contributions to Higher Order Corrections

The cross section definition in Eq. (2.24) can be written more explicitly for a perturbation theory approach:

$$\sigma = \sum_k \int d\Phi_k \frac{1}{2\hat{s}} \left| \sum_l \mathcal{M}_k^{(l)} \right|^2. \quad (2.27)$$

k is the number of final state particles. For each k the phase space $d\Phi_k$ has a different number of dimensions and there is a sum over the number of additional loops l which contribute to the amplitudes $\mathcal{M}_k^{(l)}$.

The different contributions to a fixed order calculation can be visualized by starting with a Born process, to which additional emissions (legs) or loops are added, which is shown

l (loops)	2	$\sigma_0^{(2)}$	$\sigma_1^{(2)}$	\dots		
1	1	$\sigma_0^{(1)}$	$\sigma_1^{(1)}$	$\sigma_2^{(1)}$	\dots	
0	0	$\sigma_0^{(0)}$	$\sigma_1^{(0)}$	$\sigma_2^{(0)}$	$\sigma_3^{(0)}$	\dots
		0	1	2	3	\dots
		k (legs)				

Figure 2.4: Contributions to fixed order calculations visualized as a dependence on additional legs or loops.

in Fig. 2.4. The leading order cross section for a process X is $\sigma_0^{(0)}$. The lower index counts the additional legs (k) and the upper index the additional loops (l). The $\sigma_k^{(l)}$ correspond to a power series in α_s of the squared amplitude and contain loop diagrams and interferences between different numbers of loops. $\sigma_k^{(l)}$ then has an additional factor α_s^{k+l} compared to the process $\sigma_0^{(0)}$.

Following this notation, higher order cross sections can be written as

$$\sigma_{\text{NLO}} = \sigma_0^{(0)} + \sigma_1^{(0)} + \sigma_0^{(1)}, \quad (2.28)$$

$$\sigma_{\text{NNLO}} = \sigma_0^{(0)} + \sigma_1^{(0)} + \sigma_0^{(1)} + \sigma_2^{(0)} + \sigma_1^{(1)} + \sigma_0^{(2)}. \quad (2.29)$$

One can also consider the processes $X + j$, i.e. the process with an additional jet. Its cross sections are given by

$$\sigma_{j,\text{LO}} = \sigma_1^{(0)}, \quad (2.30)$$

$$\sigma_{j,\text{NLO}} = \sigma_1^{(0)} + \sigma_2^{(0)} + \sigma_1^{(1)}. \quad (2.31)$$

LoopSim, for a description at \bar{n} NLO, includes additional emissions beyond NLO. The inputs are σ_{NLO} and $\sigma_{j,\text{NLO}}$, which are both part of σ_{NNLO} . They can be calculated using a NLO Monte Carlo implementation for the processes X and $X + j$, e.g. WZ and WZj . To combine them, one has to remove the double-counted $\sigma_1^{(0)}$ contribution, which is done by explicitly dropping the Born contributions from the $X + j$ sample. Compared to the full NNLO calculation the $\sigma_0^{(2)}$ term is missing. The IR divergent terms are known, since they have to cancel against $\sigma_1^{(1)}$ and $\sigma_2^{(0)}$. By *looping* the last two terms, an approximation of $\sigma_0^{(2)}$ can be obtained that is correct up to IR-finite corrections. These corrections are expected to scale as $\alpha_s^2 \sigma_0^{(0)}$ and are the only difference between the LoopSim description at \bar{n} NLO and a full NNLO calculation. Additional emission in diboson production and similar processes is enhanced for high transverse momenta in the form

$$\mathcal{O}\left(\alpha_s \ln^2 p_{\text{Tjet}}/m_V\right). \quad (2.32)$$

The terms are known as *Sudakov logarithms* [48, 49] and correspond to soft vector boson emission from hard jets. These contributions grow for large jet momenta and are dominant in the tails of distributions. For scales below the vector boson masses, the logarithms of Eq. (2.32) are small and the LoopSim description should not be used.

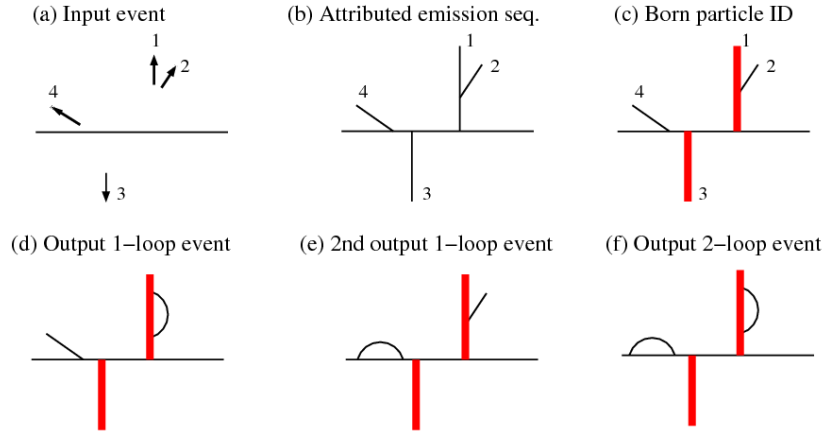


Figure 2.5: The LoopSim algorithm is schematically shown. An input event is assigned an emission sequence and then non-Born particles are *looped*. In this depiction a $2 \rightarrow 2$ Born processes is assumed and an event with two additional emissions processed. This graphic is taken from [26].

2.4.3. LoopSim Algorithm

A detailed discussion of the LoopSim algorithm can be found in [26, 50]. This section is a summary of the work presented there and uses the notation and visualizations of [26].

The LoopSim algorithm is applied to event samples on an event-by-event basis. Given a sample with additional emissions, it generates *looped* events with fewer emissions down to the Born configuration. The total weight of all generated events before cuts is chosen to sum to zero, such that looped events do not contribute to the fully inclusive cross section. Due to this conservation of the cross section, the method is also referred to as “unitarizing” events with additional emissions. Once a certain final state is required or cuts are applied, the application of the LoopSim algorithm will lead to modified fiducial cross sections. In distributions, events can be moved to other values or outside of the accepted region. This leads to non-vanishing corrections which, for observables sensitive to additional radiation, correspond to approximate NNLO corrections.

The input event is passed from a Monte Carlo program, in our case VBFNLO. The event format only records the list of final state particles and momenta as well as the weight. Details of the interface to VBFNLO are discussed in Section 5.6.

The steps of the LoopSim algorithm as depicted in Fig. 2.5 are:

- Get an input event from the fixed order Monte Carlo program (a),
- Assign an emission sequence (b),
- Identify the Born particles (c),
- Loop non-Born particles and generate 1- and 2-loop events (d-f).

Looping is the prescription to find for each real emission event a proxy event for the virtual corrections. This generated event is assigned the same weight with a relative negative sign to cancel the divergences in the real emission. The concrete algorithm will be introduced in the following.

Recombining particles

The parton level input event is received from the parton level Monte Carlo program by LoopSim. The goal of the first step is to find soft or collinear emissions, for which canceling terms are needed. To this end, the particles are clustered.

This leads to an emission sequence, where particles with small separation are connected. With this construction collinear and soft emissions will be clustered to their emitters, such that the arising IR divergences can be extracted. On the clustered state the Born configuration is selected. These particles will not be *looped*, since they are part of the selection of the underlying analysis and not part of the additional radiation.

The idea is to reverse parton-shower like splittings and the method is inspired by the CKKW procedure [51]. The C/A algorithm [52, 53] is used to cluster particles. It is usually used as a jet clustering algorithm and clusters particles, by considering pairwise distances in the plane of rapidity and azimuthal angle $\Delta R_{ij}^2 = (y_i - y_j)^2 + (\phi_i - \phi_j)^2$. Starting with the smallest distance pairs of particles are recombined into one until the minimal separation reaches a fixed limit R_{LS} . In this recombination the particle with higher p_T is considered to be the emitter and the emission history is recorded.

The Born particles are selected from the emission history using the k_T -algorithm hardness measure

$$h_{ij} = \min(p_{T_i}^2, p_{T_j}^2) \Delta R_{ij}^2 / R_{LS}^2. \quad (2.33)$$

To do so, the clustering history is traversed, following the harder parton until a final state particle is reached and marked as belonging to the Born process. This is repeated until b Born particles are identified. This emission sequence contains the leading emissions which contribute to logarithmic enhancements in the real emission. For non-enhanced (wide-angle, hard) emissions, the assigned emission sequence has less physical meaning. For these events the final effect is smaller and, as shown by the original LoopSim authors, does not significantly contribute to relevant observables.

Generating Looped events

Looped events are generated by making final state particles virtual. To accomplish this, these particles are recombined with their respective emitters according to the reconstructed emission sequence. The recombination procedure has to be infrared and collinear safe (IR-safe) to ensure the correct cancellation of the divergences. There are many potential recombination methods. LoopSim uses a method similar to the \tilde{p} -kinematics of Catani-Seymour. The momentum of the combined particle is redistributed such that the resulting particles are on-shell and have the same transverse momentum and rapidity. For the splitting from a final state particle this corresponds to adding the momenta and rescaling the sum to restore the mass of the emitter.

Formally the generation of looped events is given by the operator U_l^b . From the input event, simulated *looped* events with one or more loops will be generated. The operator U_l^b acts on an event E_n with n particles and returns events with with l loops generated by LoopSim for a Born processes with b particles. The example shown in Fig. 2.5 starts with E_4 and applies $U_{l=1}^{b=2}$. *Looping* means to apply all U_l^b with $0 \leq l \leq n - b$, such that the looped events have a final state multiplicity between b and n .

The LoopSim procedure is defined by the construction of the U_l^b operator. The maximum number of loops that can be generated on an event is given by

$$v = n - (b + n_s), \quad (2.34)$$

where n is the number of particles in the event, b the number of born particles and n_s the number of non-born emitters (intermediate particles).

The operator is defined in the extreme cases as

$$U_0^b = 1, \quad U_l^b(E_n) = 0 \quad \text{for } l > v. \quad (2.35)$$

To generate all looped diagrams, all possible numbers of loops are generated:

$$U_{\forall}^b = \sum_{l=0}^v U_l^b. \quad (2.36)$$

With a NLO input, there are events corresponding to the virtual corrections, the real emission and subtraction terms. The real emission and subtraction terms are passed as a block, to be able to sum their contribution to distributions before calculating the variance. For the generation of looped events, all input events including the real emission and subtraction events are treated individually, but the block structure is conserved for later analysis.

Each input event has an associated weight w_n from the fixed order calculation. The weight of the generated events with l additional loops is equal to the original weight w_n up to the sign:

$$w_{n-l} = (-1)^l w_n. \quad (2.37)$$

This sign is necessary to cancel the appearing divergences. The cancellation also requires to keep the absolute value of the original weight. The total weight of all events generated by U_{\forall}^b is

$$\sum_{l=0}^v \binom{v}{l} (-1)^l w_n = 0. \quad (2.38)$$

This ensures that the total cross section is not modified when the looped events are added. For inclusive observables, which are not sensitive to additional radiation, the looped events sum to 0. For observables that depend on the additional radiation the events with alternating signs will move contributions from one phase space point to another and thus induce shape changes in histograms.

The effect of the U_l^b operator on some topologies is visualized by the following diagrams that are taken from [26]:

$$U_{l=1}^{b=2} \left(\begin{array}{c} 2 \\ | \\ \hline | \\ 1 \end{array} \right) = - \begin{array}{c} 2 \\ | \\ \hline | \quad \text{loop} \\ 1 \end{array} - \begin{array}{c} 2 \\ | \\ \hline | \quad \text{loop} \\ 1 \end{array}, \quad (2.39)$$

$$U_{l=2}^{b=2} \left(\begin{array}{c} 2 \\ | \\ \hline | \\ 1 \end{array} \right) = \begin{array}{c} 2 \\ | \\ \hline | \quad \text{loop} \quad \text{loop} \\ 1 \end{array}, \quad (2.40)$$

$$U_{l=2}^{b=2} \left(\begin{array}{c} \text{2} \\ | \\ \text{---} \\ | \\ \text{1} \end{array} \right) = \begin{array}{c} \text{2} \\ | \\ \text{---} \\ | \\ \text{1} \end{array} \begin{array}{c} | \\ \text{---} \\ | \end{array} + \begin{array}{c} \text{2} \\ | \\ \text{---} \\ | \\ \text{1} \end{array} \begin{array}{c} \text{---} \\ \text{---} \\ \text{---} \\ | \end{array} + \begin{array}{c} \text{2} \\ | \\ \text{---} \\ | \\ \text{1} \end{array} \begin{array}{c} \text{---} \\ \text{---} \\ \text{---} \\ | \end{array}, \quad (2.41)$$

$$U_{l=2}^{b=2} \left(\begin{array}{c} \text{2} \\ | \\ \text{---} \\ | \\ \text{1} \end{array} \right) = \begin{array}{c} \text{2} \\ | \\ \text{---} \\ | \\ \text{1} \end{array} \begin{array}{c} \text{---} \\ \text{---} \\ \text{---} \\ | \end{array}. \quad (2.42)$$

Generating one loop on an event with 4 particles and 2 Born particles is shown in Eq. (2.39). For a \bar{n} NLO calculation of a process with 2 Born particles, all potential loops of the 4 particle event would have to be considered, such that the relevant operator is

$$U_{\forall}^2 = U_0^2 + U_1^2 + U_2^2. \quad (2.43)$$

Therefore, in addition to Eq. (2.39) also Eq. (2.40) and the original event are needed to get all possible looped combinations:

$$U_{\forall}^2 \left(\begin{array}{c} \text{2} \\ | \\ \text{---} \\ | \\ \text{1} \end{array} \right) = \begin{array}{c} \text{2} \\ | \\ \text{---} \\ | \\ \text{1} \end{array} \begin{array}{c} | \\ \text{---} \\ | \end{array} - \begin{array}{c} \text{2} \\ | \\ \text{---} \\ | \\ \text{1} \end{array} \begin{array}{c} \text{---} \\ \text{---} \\ \text{---} \\ | \end{array} - \begin{array}{c} \text{2} \\ | \\ \text{---} \\ | \\ \text{1} \end{array} \begin{array}{c} \text{---} \\ \text{---} \\ \text{---} \\ | \end{array} + \begin{array}{c} \text{2} \\ | \\ \text{---} \\ | \\ \text{1} \end{array} \begin{array}{c} \text{---} \\ \text{---} \\ \text{---} \\ | \end{array}. \quad (2.44)$$

Depending on the number of available and requested loops, all potential combination have to be generated as shown in Eq. (2.41) for two loops and three emissions. The recombination follows the emission sequence, such that emissions which stem from a certain particle are looped back to it as shown in Eq. (2.42).

The looping procedure is agnostic to the flavor of the considered particle. This is mostly based on the fact that VBFNLO, like many parton level Monte Carlo programs, assumes summation over the available flavors and by default does not generate specific flavor combinations. The LoopSim method can also be applied to non-QCD final state particles. For massive particles the redistribution and hardness measure of the clustering step has to be adjusted. For this thesis, all events that would lead to looped W or Z bosons are dropped by explicitly requiring all electroweak particles to be in the final event. These types of diagrams could be used to simulate electroweak loops. The total cross section gets a non-vanishing contribution by always including the real emission but dropping events, where the looping algorithm would remove electroweak bosons.

Calculating \bar{n} NLO corrections

Using the U_l^b operator, samples with simulated loops can be defined. Starting with LO descriptions of a process X with b final state particles and the LO calculation of $X + j$, the NLO corrections to X are approximated as

$$X@{\bar{n}}LO = X@LO + U_{\nabla}^b(X + j@LO). \quad (2.45)$$

A similar description can be used to combine NLO events into a \bar{n} NLO sample:

$$X@{\bar{n}}NLO = X@NLO + U_{\nabla,1}^1(X + j@NLO_{\text{only}}). \quad (2.46)$$

Starting with NLO samples, the exact one-loop amplitudes are used, such that the LoopSim operator has to be adjusted. From the $X + j@NLO$ sample the Born contributions are neglected, since they appear as the real emission of $X@NLO$. The combination of virtual corrections and real emission is called $X + j@NLO_{\text{only}}$. Denoting events by the number of final state particles n and the number of exact loops calculated l as $E_{n,l}$, this sample has contributions from the virtual corrections to $E_{n-1,1}$ and from the real emission to $E_{n,0}$. Applying U_{∇}^b to $E_{n,0}$ will generate an approximation of $E_{n-1,1}$ that should be replaced by the exact calculation. For E_{n-2} type events, generated loops from both E_n and E_{n-1} states are needed to cover all potentially appearing divergences. To summarize, this leads to

$$U_{\nabla,1}^b(E_{n,0}) = U_{\nabla}^b(E_{n,0}) - U_{\nabla}^b(U_1^b(E_{n,0})), \quad (2.47)$$

$$U_{\nabla,1}^b(E_{n-1,1}) = U_{\nabla}^b(E_{n-1,1}). \quad (2.48)$$

This construction can be extended in two ways. Combining two NNLO samples would give a prediction at $\bar{n}NNLO$. On the other hand more than two NLO samples can be combined. With NLO calculations of process X , $X + j$ and $X + 2j$ a precision of $\bar{n}\bar{n}NLO$ is possible.

Uncertainties

The radius R_{LS} , used in the recombination step, can be varied to generate an uncertainty estimate due to the clustering procedure. This will highlight which observables are sensitive to LoopSim corrections and additional emissions. In general for electroweak observables (transverse momenta of leptons or electroweak bosons) the sensitivity is small and significantly below the renormalization scale dependence while for jet observables (transverse momenta, invariant masses or distances between jets) the R_{LS} dependence can exceed the scale dependence.

The scale dependence of the \bar{n} NLO result overestimates the NNLO scale dependence since the cancellations that lead to a reduction of the scale dependence needs the full virtual corrections. The size of the scale dependence is thus close to the original NLO scale band for most observables.

For this thesis, the LoopSim implementation as published in [54] is used with modifications to include bin smearing as discussed in Section 5.2.2. The analysis uses the LoopSim internal analysis tools that are based on FastJet [55].

Anomalous Couplings

Anomalous couplings (AC) parametrize deviations from couplings between particles predicted by the SM. In Section 3.1 the concept of *Effective Field Theory* (EFT) will be introduced. One application of this framework is to extend the SM to include anomalous couplings, which is presented in Section 3.2. The couplings of electroweak bosons are then investigated in Section 3.3. EFTs are only valid in a specific combination of phase space and parameters. The limits of their validity are discussed in Section 3.4. The range of validity can also be studied by comparing interference terms and squared terms as in Section 3.5. Finally, the dependence on the choice of basis (Section 3.6) and the restoration of unitarity (Section 3.7) will be discussed.

3.1. Effective Field Theory

A field theory is defined by symmetry groups and a set of fields, which are the available degrees of freedom and are related to its matter content.

When looking for physics beyond the SM, new elementary particles are included by introducing new fields within a theory. The masses of these particles are often constructed to be heavier than the masses of SM particles to avoid exclusion by current experimental searches.

Therefore, one can distinguish two different energy scales:

$\Lambda_{\text{observable}}$ energy scale, at which the observable is measured, for the LHC this is typically around the electroweak scale, $O(100 \text{ GeV})$,

$\Lambda_{\text{New Physics}}$ scale of a New Physics model, which is of the order of the mass scale of New Physics particles, $O(\text{TeV})$.

If these scales are sufficiently different, observables at the low scale are well approximated by neglecting contributions from New Physics. This is called *decoupling* and its applicability is stated in the decoupling theorem [56–59]. Depending on the New Physics model, there can be non-decoupling effects. An example, where non-decoupling affects an EFT description in Higgs physics is given in [60].

A more general concept is the *separation of scales* and appears in a wide variety of areas of physics. Dimensionful quantities, like new energy scales, can appear in predictions for dimensionless quantities, like corrections to observables, only in the form of ratios. The ratio of a New Physics model prediction O_{NP} to the corresponding SM prediction O_{SM} can be written as a function of the ratio of scales:

$$\frac{O_{\text{NP}}}{O_{\text{SM}}} = f\left(\frac{\Lambda_{\text{observable}}}{\Lambda_{\text{New Physics}}}\right). \quad (3.1)$$

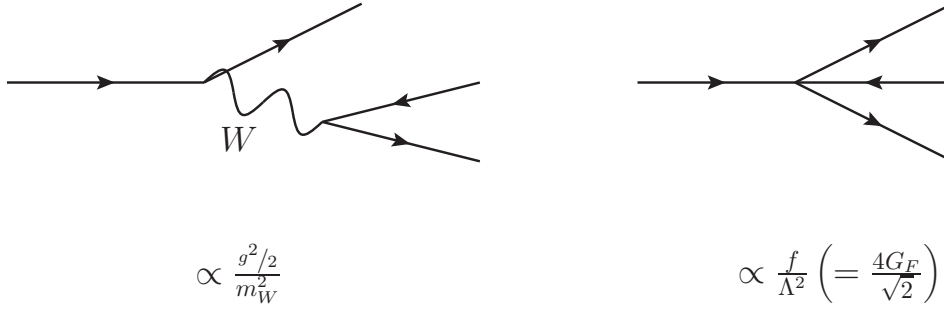


Figure 3.1: The interaction of four fermions in β decay or the decay of a muon, is described by the exchange of a weak boson. In the low energy limit, this exchange can be expressed in terms of a dimension-6 operator. This formulation is called Fermi Theory.

If the scales are well separated, the ratio is small and allows to expand f in a series. Corrections due to new New Physics can therefore be expressed as a power series of the ratio of the observable scale and the new mass scale.

The EFT approach can be used in two ways:

top-down Start with a theory at a high scale and derive the effects at a low scale by *integrating out* the heavy degrees of freedom.

bottom-up Start with a low scale theory and add all higher-dimension terms that can appear in a top-down approach.

The bottom-up approach is used, when deviations from the SM should be described in a model-independent way, since the full theory is not yet known. At the low energy scale, the high energy effects are described by operators that only consist of low energy fields and obey the symmetries of the low energy theory. They have an energy dimension larger than four, which is compensated by dimensionful couplings. The Lagrangian can be written as

$$\mathcal{L}_{\text{EFT}} = \sum_d^D \sum_i \frac{f_i}{\Lambda^d} \mathcal{O}_i^{(d)}. \quad (3.2)$$

The prefactors f_i are called *Wilson coefficients*. The EFT is an expansion in powers of Λ that is cut at a dimension D . In this power series, a priori there is no distinction between the scale Λ and Wilson coefficient f_i . The scaling of an operator is given by the dimensionful combination

$$F_i = \frac{f_i}{\Lambda^d}. \quad (3.3)$$

In the following the shorthand F_i will refer to the dimensionful coupling and, as an abbreviation, in figures the units will be assumed to be TeV^{-2} and not explicitly stated.

3.1.1. Fermi Theory

The concept of EFT can be illustrated using the example of Fermi Theory. Fermi Theory was developed in 1934 [61, 62] to model β decay. It uses the previously introduced neutrino and a four-fermion vertex, as shown on the left in Fig. 3.1. This description applies to β decays of nuclei as well as muon decay.

The coupling of this vertex has dimensions of E^{-2} . This vertex is non-renormalizable, which means that for each order in perturbation theory one has to introduce a growing number of counterterms. In general in a (3+1)-dimensional theory all operators in the Lagrangian with dimension larger than 4 and, therefore, couplings with negative energy dimension will show this behavior.

Following the discovery of neutral currents [63], in 1983, the W and Z bosons were discovered at LEP [64, 65]. Using the electroweak theory, β decay can be modeled with a weak boson as force carrier between two fermion lines, as shown on the right in Fig. 3.1, in contrast to an elementary interaction between four fermions.

The four-fermion interaction corresponds to the operator

$$\frac{G_F}{\sqrt{2}} \left(\bar{\psi}_i (1 - \gamma_5) \gamma^\mu \psi_j \right) \left(\bar{\psi}_k (1 - \gamma_5) \gamma_\mu \psi_l \right), \quad (3.4)$$

while using the SM the amplitude is

$$\left(\bar{\psi}_i \frac{ig}{\sqrt{2}} \frac{(1 - \gamma_5)}{2} \gamma^\mu \psi_j \right) \frac{-g_{\mu\nu}}{p^2 - m_W^2} \left(\bar{\psi}_k \frac{ig}{\sqrt{2}} \frac{(1 - \gamma_5)}{2} \gamma^\nu \psi_l \right). \quad (3.5)$$

If the invariant mass carried by this W boson is smaller than its on-shell mass, $p^2 \ll m^2$, one can expand the W boson propagator in $\frac{p^2}{m_W^2}$

$$\frac{1}{p^2 - m_W^2} = -\frac{1}{m_W^2} + O\left(\frac{p^2}{m_W^2}\right). \quad (3.6)$$

By matching the Fermi theory to the expanded electroweak theory, one finds

$$G_F = \sqrt{2} \frac{g^2}{8m_W^2}. \quad (3.7)$$

Also the next-to-leading term can be studied, which grows as $\frac{p^2}{m_W^2}$. This term allows to estimate the area of validity for the Fermi theory. As soon as the W boson is close to on-shell the expansion breaks down and the full electroweak theory is needed. At the muon mass, corrections are only of order $m_\mu^2/m_W^2 \approx 10^{-6}$.

The four-fermion vertex is a dimension-6 term and as such also of interest to bottom-up approaches. Analogously as the GWS theory, which contains W and Z bosons as high-energy extension for the Fermi theory, a new theory containing a W' or Z' boson can be constructed, which generates a new four-fermion interaction at current experimentally reachable scales.

3.1.2. Modern Applications of Top-Down Effective Field Theories

A recently active area using the top-down approach is the calculation of higher order corrections. When diagrams contain loops with heavy particles, these can be “integrated out” and reduced to tree-level diagrams.

A typical example is the production of a Higgs boson at the LHC. The leading production channel is gluon fusion, which is shown on the left in Fig. 3.2. This process contains one loop



Figure 3.2: Diagrams for gluon fusion production of a Higgs boson. On the left the one-loop diagram with a top-quark loop is shown. Using EFT this amplitude can be expanded in the ratio m_h/m_t , which results in an effective ggh vertex.

already at leading order, which increases the difficulty to calculate higher order corrections. The partonic cross section reads [66–68]

$$\sigma = \frac{G_F \alpha_s^2}{288 \sqrt{2} \pi} |A(\tau)|^2 m_h^2 \delta(\hat{s} - m_h^2), \quad (3.8)$$

$$A(\tau) = \frac{3}{2} \tau [1 + (1 - \tau) f(\tau)], \quad (3.9)$$

$$f(\tau) = \begin{cases} \arcsin^2 1/\sqrt{\tau}, & \text{for } \tau \geq 1 \\ \frac{1}{2} \left[\ln \frac{1 + \sqrt{1 - \tau}}{1 - \sqrt{1 - \tau}} - i\pi \right]^2, & \text{for } \tau < 1 \end{cases}, \quad (3.10)$$

$$\tau = \frac{4m_t^2}{m_h^2}. \quad (3.11)$$

To simplify calculations based on this amplitude, one can use an EFT. The scale of the process is given by the Higgs boson mass m_h , which in the amplitude appears as a ratio with the top quark mass m_t . Since $m_t > m_h$, the cross section can be expanded for large values of τ :

$$A(\tau) = 1 + \mathcal{O}\left(\frac{1}{\tau}\right). \quad (3.12)$$

The leading term in this expansion gives a constant amplitude, which is independent of the heavy quark mass. This term corresponds to an effective ggH vertex, which is given by a dimension 5 operator connecting two gluons with the Higgs boson

$$\mathcal{O}_{\text{ggh}} = \frac{\alpha_s}{12\pi} \sqrt{\sqrt{2} G_F} G_{\mu\nu}^a G_{\mu\nu}^a h. \quad (3.13)$$

The corresponding diagram is shown on the right in Fig. 3.2. Since the leading order corresponds to a tree-level diagram, one can calculate NLO corrections easier and extend higher order corrections to N³LO with dedicated calculations [69]. Calculating the coefficients of EFT operators in the low-energy theory in terms of parameters of the high-energy theory is called *matching*. Besides reducing the loop order, the EFT also removes the massive propagators and leaves only massless propagators for the QCD corrections, which simplifies the calculation of the amplitudes even further.

3.2. The Standard Model as an Effective Field Theory

Many New Physics models predict particles at scales above the electroweak scale. Therefore, one can consider the SM to be a low energy limit of a yet unknown, UV-complete, theory at a higher scale. In this scheme, the existing SM Lagrangian, with operators of dimension 4, is only the leading term in an EFT expansion.

We expect that a new theory at high energy scales also respects the SM symmetry $SU(2)_L \times U(1)_Y$. Most models for physics beyond the SM start with a certain set of symmetries at a high scale, of which the SM symmetry group is a subgroup. When moving to a lower scale, the symmetry of the new model is broken to the SM group. Therefore, it should be possible to describe such a new physics model using an EFT in terms of the SM fields and symmetries.

If the SM is extended in a bottom-up approach, there are terms for $d = 5$ and above. Only SM fields are used and all terms need to be invariant under the SM gauge symmetries. The building blocks to construct gauge invariant operators are

- Higgs field Φ ,
- fermion fields Ψ ,
- (covariant) derivative ∂^μ, D^μ and
- field strength tensors $G^{\mu\nu}, W^{\mu\nu}, B^{\mu\nu}$.

The only $d = 5$ term, called the Weinberg operator [70], corresponds to a Majorana mass for the neutrino:

$$\left(\bar{E}_L^c \tilde{\Phi}^*\right) \left(\tilde{\Phi}^\dagger E_L\right), \quad (3.14)$$

where $E_L = (\nu_e, e_L)^T$ is the left-handed lepton doublet and $\tilde{\Phi} = i\sigma_2\Phi$.

Once lepton number conservation is required, the lowest allowed energy dimension is $d = 6$. Higher orders would be $d = 7$, which only exists if $B - L$ violation is allowed and $d = 8$, which adds a significant number of new operators. The total number of independent operators at $d = 8$ and above was only recently systematically studied in [71].

In general the dimension-6 operators can be grouped into several categories:

- fermionic operators, connecting four fermion fields,
- mixed operators, connecting bosonic and fermionic fields and
- bosonic operators, connecting only bosonic fields.

As will be discussed in Section 3.6, it is possible to relate different operators by equations of motion. Writing down all possible operators leads to groups that have redundancies. An initial complete basis with 80 operators of dimension 6 was introduced by Buchmüller and Wyler in [72] and updated to a minimal basis of 59 flavor-universal operators in [73], which is now called the *Warsaw* basis. This approach is also referred to as Standard Model Effective Field Theory (SMEFT). Many of the operators containing fermions can be constraint from electroweak precision data or flavor physics. Recently ideas were published to also consider fermionic operators at the LHC [74, 75]. We study anomalous couplings in the gauge boson sector and will focus on purely bosonic operators.

There are alternative approaches to expand the SM using an EFT. The non-linear EFT approach [76–78] uses a Higgs boson that is not in a doublet representation and has a different EFT expansion parameter. This is useful if the underlying UV-complete theory is assumed to have a different mechanism of electroweak symmetry breaking or a composite Higgs boson.

3.3. Anomalous Couplings in the Gauge Boson Sector

In the SM, the WWH interaction is described in the Lagrangian as introduced in Section 2.1. The Feynman rule for this WWH vertex is $igm_W g^{\mu\nu}$.

An example dimension 6 operator which leads to a modification of the WWH vertex is

$$\mathcal{O}_W = (D_\mu \Phi)^\dagger \hat{W}^{\mu\nu} (D_\nu \Phi) . \quad (3.15)$$

It can be added to the SM Lagrangian as

$$\mathcal{L} = \mathcal{L}_{\text{SM}} + \frac{f_W}{\Lambda^2} \mathcal{O}_W . \quad (3.16)$$

This operator introduces an additional WWH interaction term with the corresponding Feynman rule

$$-\frac{1}{2}i \frac{f_W}{\Lambda^2} g m_W (-g^{\mu\nu} (p_h \cdot p_- + p_h \cdot p_+) + p_h^\nu p_-^\mu + p_h^\mu p_+^\nu) , \quad (3.17)$$

where p_h is the momentum of the Higgs boson and p_\pm the momenta of the W^\pm attached to the WWH vertex.

Comparing the Feynman rule induced by \mathcal{O}_W to the SM expression, there is an additional momentum dependence, that scales as p^2/Λ^2 , where p^2 is a quadratic dependence on combinations of momenta. This scaling is a consequence of the dimension-6 operator, which introduces a dimensionful coupling. The phenomenological consequences of this scaling will be discussed in Section 3.5.

Dimension 6 operators can, in addition to terms which increase with the energy, also introduce terms which scale as v^2/Λ^2 . These will lead to a constant (and small) rescaling of SM terms and can be partially absorbed in the renormalization of SM parameters, see Section 3.6 for more details. Another effect of the p^2 dependence is the violation of unitarity at large scales, which will be discussed in Section 3.7.

We will use the \mathcal{O}_W operator as a typical representative for anomalous couplings. It affects VVH vertices as well as WWZ which allows to use it both in the study of WH associated production as well as in WZ production. Using diboson production, this operator was already restricted by LEP data. The global fit in [79] gives for the coupling f_W/Λ^2 a 90% CL interval of $[-5.6, 9.6] \text{ TeV}^{-2}$. Very recently a 95% CL limit of $[-2.0, 5.7] \text{ TeV}^{-2}$ was presented by the CMS experiment [80] using only semileptonic decays in WZ production.

3.3.1. The HISZ Basis

The basis used in VBFNLO and for this thesis was introduced in [81] and updated in [82]. For the field strength tensors this notation includes the coupling constants:

$$\begin{aligned} \hat{W}_{\mu\nu} &= ig W_{\mu\nu}^a T^a , \\ \hat{B}_{\mu\nu} &= ig' B_{\mu\nu} . \end{aligned} \quad (3.18)$$

In this basis the C and P conserving operators leading to gauge field interactions are

$$\begin{aligned}
\mathcal{O}_W &= (D_\mu \Phi)^\dagger \hat{W}^{\mu\nu} (D_\nu \Phi), \\
\mathcal{O}_B &= (D_\mu \Phi)^\dagger \hat{B}^{\mu\nu} (D_\nu \Phi), \\
\mathcal{O}_{WWW} &= \text{Tr} \left[\hat{W}_{\mu\nu} \hat{W}^{\nu\rho} \hat{W}_\rho^\mu \right], \\
\mathcal{O}_{WW} &= \Phi^\dagger \hat{W}_{\mu\nu} \hat{W}^{\mu\nu} \Phi, \\
\mathcal{O}_{BB} &= \Phi^\dagger \hat{B}_{\mu\nu} \hat{B}^{\mu\nu} \Phi, \\
\mathcal{O}_{\Phi,1} &= (D_\mu \Phi)^\dagger \Phi \Phi^\dagger (D^\mu \Phi), \\
\mathcal{O}_{DW} &= \text{Tr} \left(\left[D_\mu, \hat{W}_{\nu\rho} \right] \left[D^\mu, \hat{W}^{\nu\rho} \right] \right), \\
\mathcal{O}_{BW} &= \Phi^\dagger \hat{B}_{\mu\nu} \hat{W}^{\mu\nu} \Phi.
\end{aligned} \tag{3.19}$$

The operators $\mathcal{O}_{\Phi,1}$, \mathcal{O}_{DW} and \mathcal{O}_{BW} contribute to gauge boson two-point functions at tree-level and are therefore constrained by electroweak precision data. Since these limits are strict these operators will not be considered for triple gauge coupling modifications. To study the WWZ vertex only \mathcal{O}_W , \mathcal{O}_B and \mathcal{O}_{WWW} have to be considered.

3.3.2. Mass Basis

Earlier parametrizations of AC effects are formulated in the mass basis after electroweak symmetry breaking. This formalism was first introduced in [83] and used for the study of interactions between weak bosons at LEP and the Tevatron in e.g. [84, 85]. A more recent review is available in [86].

A subset of the terms in the mass basis that contribute to triple gauge couplings are

$$\mathcal{L} = ig_1^V \left(W_{\mu\nu}^\dagger W^\mu V^\nu - W_\mu^\dagger V_\nu W^{\mu\nu} \right) + i\kappa_V W_\mu^\dagger W_\nu V^{\mu\nu}, \tag{3.20}$$

where V is γ or Z . The HISZ basis induces terms in the mass basis with the relations [87]

$$g_1^Z = 1 + f_W \frac{m_Z^2}{2\Lambda^2} \tag{3.21}$$

$$\kappa_Z = 1 + \left(f_W - s_\theta^2 (f_B + f_W - 2f_{WB}) \right) \frac{m_Z^2}{2\Lambda^2} \tag{3.22}$$

$$\kappa_\gamma = 1 + (f_B + f_W - 2f_{WB}) \frac{m_Z^2}{2\Lambda^2} \tag{3.23}$$

The downside of this formulation is that it is based on the mass basis after electroweak symmetry breaking and gauge symmetry is not preserved for a general choice of coupling values. On the other hand, in the SMEFT approach gauge connections between terms and correlations between different contributions to observables are enforced by the construction of the theory.

The translations given in Eq. (3.21) highlight these correlations, since the combination $f_B + f_W - 2f_{WB}$ appears in both κ_Z and κ_γ . For a current overview of these translations and limits in both formulations see also the review [88]. For the most general couplings in the gauge boson sector dimension 8 operators have to be included. Using only dimension 6 operators, there are no neutral triple gauge couplings and a very limited number of quartic gauge couplings. Both of these contributions appear in operators of dimension 8. Dimension 8 operators are predominantly studied in vector boson scattering [89] and triple vector boson production [90].

3.4. Validity of Effective Field Theories

EFTs are based on an expansion in the ratio of scales $\Lambda_{\text{observable}}/\Lambda_{\text{New Physics}}$. The EFT is only applicable if this expansion parameter is small, which means that the full theory is well described by a truncated series. In terms of the scales, this assumes, that the observed scales are smaller than the New Physics scales and that there are no resonances at or below the observed scale. In a top-down approach, one can calculate additional terms of the expansion and check the convergence of the series and, thereby determine, whether only including the leading elements of the series leads to a valid descriptions.

In a bottom-up approach it is more difficult to estimate the validity-limit, since there are two elements to the expansion, which are both not fixed a priori:

- New Physics scale $\Lambda_{\text{New Physics}}$ and
- couplings f_i .

The actually relevant ratio in the expansion is $f_i \Lambda_{\text{observable}}/\Lambda_{\text{New Physics}}$ and should be significantly below 1. The couplings f_i depend on the New Physics model. Unitarity of scattering amplitudes gives upper limits on these couplings. On the other hand couplings can be small. In the SM there is a significant range of coupling sizes (strong and weak interaction). Thus, different coupling values are also expected in models of physics beyond the SM. A detailed discussion of EFT power counting in weakly and strongly coupled theories is given in [91].

For a fixed scale $\Lambda_{\text{observable}}$, the convergence of the EFT expansion can be improved by either smaller couplings or larger scales $\Lambda_{\text{New Physics}}$. Improving the expansion therefore directly corresponds to smaller New Physics effects. Typical experimental analyses are most sensitive to large deviations which appear for high invariant masses, where the EFT effect is enhanced. This phase space region is also close to where the EFT expansion breaks down. Thus, a consistent description close to the validity limit is needed. Potential solutions will be described in Section 3.7.

3.5. Interference and Squared Terms

For amplitudes like diboson production, the SM is the leading term in the EFT expansion at Λ^0 . The next relevant terms appearing are at Λ^{-2} (dimension 6) and Λ^{-4} (dimension 8). Measurements use cross sections, which are proportional to $|\mathcal{M}|^2$. Considering the terms in the squared amplitude one finds [92]

$$\mathcal{M} = \mathcal{M}_{\text{SM}} + \underbrace{\mathcal{M}_{\text{AC}}^{d=6}}_{1/\Lambda^2} + \underbrace{\mathcal{M}_{\text{AC}}^{d=8}}_{1/\Lambda^4} + O(\Lambda^{-6}), \quad (3.24)$$

$$|\mathcal{M}|^2 = \underbrace{|\mathcal{M}_{\text{SM}}|^2}_{1/\Lambda^0} + \underbrace{2 \text{Re} \mathcal{M}_{\text{SM}}^* \mathcal{M}_{\text{AC}}^{d=6}}_{1/\Lambda^2} + \underbrace{|\mathcal{M}_{\text{AC}}^{d=6}|^2}_{1/\Lambda^4} + \underbrace{2 \text{Re} \mathcal{M}_{\text{SM}}^* \mathcal{M}_{\text{AC}}^{d=8}}_{1/\Lambda^4} + \underbrace{|\mathcal{M}_{\text{AC}}^{d=8}|^2}_{1/\Lambda^8} + O(\Lambda^{-6}). \quad (3.25)$$

Ordering the contributions to the squared amplitude in Eq. (3.25) in powers of Λ gives:

$$\Lambda^0 : |\mathcal{M}_{\text{SM}}|^2 , \quad (3.26)$$

$$\Lambda^{-2} : 2 \text{Re} \mathcal{M}_{\text{SM}}^* \mathcal{M}_{\text{AC}}^{d=6} , \quad (3.27)$$

$$\Lambda^{-4} : \left| \mathcal{M}_{\text{AC}}^{d=6} \right|^2 + 2 \text{Re} \mathcal{M}_{\text{SM}}^* \mathcal{M}_{\text{AC}}^{d=8} . \quad (3.28)$$

The leading AC contribution is the interference of dimension 6 operators with the SM amplitude, while the squared dimension 6 amplitude appears at the same order as the dimension 8 interference term with the SM. In a conservative approach, the Λ^{-4} contributions should not be used to extract limits without also studying dimension 8 operators simultaneously. The Λ^{-4} terms also introduce a dependence on the basis, as will be discussed in Section 3.6.

For the study of dimension 6 operators, we will include both terms, the interference and the squared term, in the following. When calculating predictions to observables, one could consider both the interference and the squared term separately. If the calculation is based on amplitudes and not on squared amplitudes (as in **VBFNLO**), the separation might require more complex modifications. Also including only the interference term might lead to momentum configurations where a negative interference term is larger than the SM contributions. This can generate negative differential cross sections, which break traditional unweighting techniques.

In that case one can instead study the dependence of the resulting prediction on the coupling. For any observable, the interference term shows a linear dependence on the AC value, while the squared term has a quadratic dependence. This way both the interference and the quadratic contributions can be extracted by fitting a quadratic polynomial to a series of three different AC values. This fit can then be used to extrapolate to arbitrary coupling values.

There might be new physics models, where the EFT expansion is dominated by the $\left| \mathcal{M}_{\text{AC}}^{d=6} \right|^2$ term. This can happen if the SM amplitude is accidentally small. The SM is known to have cancellations of different contributions to an amplitude in many processes. One of the drastic cancellations is the *radiation zero* in $W\gamma$ production. In this process, the LO amplitude vanishes exactly for a certain momentum configuration. At higher orders, this cancellation is smeared out, but a clear reduction is still experimentally visible in this phase space region.

The suppression of the interference term could also appear only for certain helicity combinations. If the anomalous coupling favors helicity combinations that are small in the SM, the overall amplitude might be dominated by the helicity combinations favored by the New Physics model. This scenario is often considered in vector boson scattering, where the SM cross section mostly contains transverse polarization, while anomalous coupling operators can favor longitudinal polarizations. One more example where the interference of dimension 6 operators with the SM is suppressed is discussed in [93]. It is shown that for certain operators containing fermion fields, amplitudes for helicity combinations arise, which do not contribute in the SM.

Another reason for a suppressed interference term could be, that the New Physics interaction is strongly coupled, such that the weak coupling that describes gauge boson interactions in the SM is small compared to the strong coupling appearing in the New Physics model. Depending on the value of the coupling, a perturbative approach might not be applicable and different formulations are needed.

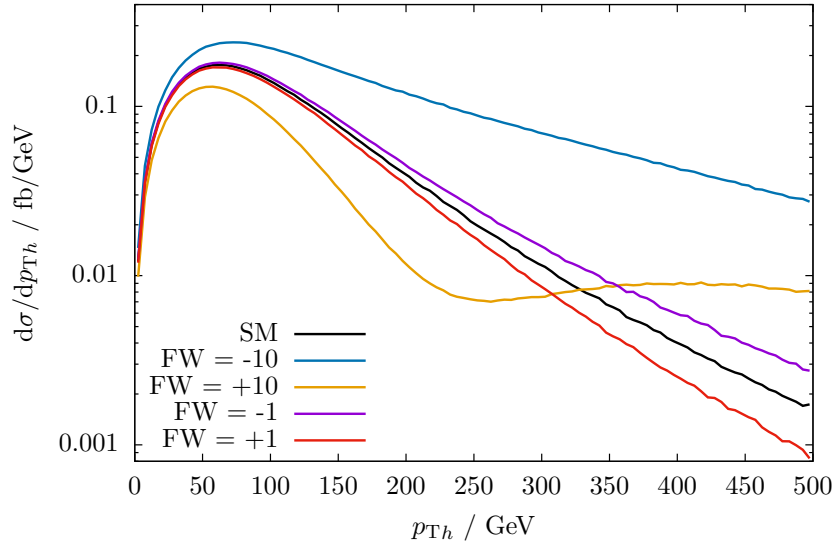


Figure 3.3: Higgs p_T for WH associated production at NLO QCD is shown for the SM (black) and the \mathcal{O}_W operator with different coupling values. Here and in the following plots the units are implicit: $F_W = 10$ stands for $f_W/\Lambda^2 = 10 \text{ TeV}^{-2}$.

Example of anomalous coupling effect on distributions

The typical effect of AC on observables can be seen in Fig. 3.3. The size of the effect depends on the scale of the observable, here the transverse momentum of the Higgs boson. At small scales, the effect is minuscule and typically on the order of a percent. It grows with the p_T and the sign of the effect depends on the sign of the anomalous couplings. In this region, the relevant term is the interference $\mathcal{M}_{\text{SM}}\mathcal{M}_{\text{AC}}^*$, which is proportional to $f_W p^2/\Lambda^2$. For larger momentum values the $|\mathcal{M}_{\text{AC}}|^2$ term becomes dominant. It is proportional to $f_W^2 p^4/\Lambda^4$. These terms being competitive means that $p^2 = \Lambda^2/f_W$, which, depending on the coupling, is the phase space region where the EFT becomes invalid.

3.6. Choice of Basis

The choice of dimension 6 operators is not unique. One can transform one operator into a set of different operators using several methods. The first is *equations of motion*, which are differential equations for the fields in the Lagrangian. The field definition can also be modified to absorb terms into renormalization constants. Another method is to use *integration by parts*. This uses the property that a total derivative in the Lagrangian does not change the described physics. Therefore, integration by parts can be used to move a derivative from one term to another. Combining these two methods allows to transform operators into linear combinations of each other. In both methods, additional higher order contributions that would correspond to dimension 8 terms are neglected.

For the most common bases there are prescriptions on how to translate operator coefficients, for example in [94]. Only the leading term $O(f/\Lambda^2)$ is unique in these translations, but corrections appear at $O(f^2/\Lambda^4)$. Also the translation to the mass basis $(\kappa_\gamma, \kappa_Z, g_1^Z)$ is formally only valid to order $1/\Lambda^2$.

Furthermore, when transforming experimental bounds on EFT operators, the transformations mostly assume that only the linear term is considered. Thus, including the $|\mathcal{M}_{\text{AC}}^{d=6}|^2$ term in calculations or when extracting limits makes them depend on the choice of basis for the EFT.

There is a multitude of bases used in the literature. Not all utilized bases are complete and minimal. Besides the HISZ basis, popular bases are the Warsaw basis [73], the SILH basis [95] and the mass basis [86]. A review of several bases and their use can be found in [96]. The choice of basis is also relevant for higher order corrections to the couplings induced by dimension 6 operators. Work towards these corrections in the form of RGE running is presented in [97].

3.7. Unitarity

EFTs in general lead to a violation of unitarity, when applied to regimes, where the expansion of the EFT is not valid. For the production of gauge boson pairs, this happens for example in the phase space region with a high invariant mass of the gauge boson pair. One of the motivations when building the LHC was that without the Higgs boson, W boson scattering would violate unitarity around the TeV scale, such that the LHC would have to either find a Higgs boson, or some other kind of non-SM gauge boson interaction.

To set limits on anomalous couplings in an experiment, one should not compare to an obviously unphysical prediction. Instead one should modify the theory prediction, such that it does not violate unitarity, i.e. *unitarize* the cross section. There is no unique procedure to do this.

There are several unitarization methods used in the literature that fit in one these groups:

- Form Factor,
- Cut-off at a fixed scale,
- K-matrix, T-matrix.

Form Factor

In the Form Factor approach, each anomalous coupling vertex is multiplied by a phase space dependent factor. In this thesis, a form factor is used of the form

$$\mathcal{F}(\mu) = \left(1 + \frac{\mu^2}{\Lambda_{\text{FF}}^2}\right)^{-n}. \quad (3.29)$$

The form factor introduces two new parameters: The form factor scale Λ_{FF} and the exponent n . μ is the scale of the process. For diboson production, m_{VV} is used. Another common choice for the scale is $\sqrt{\hat{s}}$, the total invariant mass of the collision.

The form factor is constructed to have little to no effect for momenta below the unitarity limit, especially at the production threshold, which is dominant for inclusive production. At large invariant masses, the form factor should suppress the unphysical growth of the amplitude with a factor m_{VV}^{-2n} . In between these two phase space regions, the expression in Eq. (3.29) provides a smooth transition. The analytical expression is inspired by the nucleon form factor [98]

$$G_E(Q^2) = \frac{1}{\left(1 + \frac{Q^2}{0.71 \text{ GeV}^2}\right)^2}. \quad (3.30)$$

The form factor exponent n can be chosen depending on the operator used, such that the leading \hat{s} dependence of the operator is canceled by the form factor. For dimension-6 operators

this leads to $n = 1$ and for dimension-8 operators $n = 2$. The scale Λ_{FF} determines at which scale the form factor leads to a sizable suppression. It should therefore be sufficiently large. An upper bound can be set by the unitarity requirement.

The form factor tool [99] is published along with `VBFNLO`. It calculates, for a given set of operator couplings, the maximum allowed form factor scale, such that unitarity is preserved. To accomplish this, the 0th partial wave of the $2 \rightarrow 2$ scattering of vector bosons is analyzed and for each amplitude the limit $|\text{Re}(a_i)| < \frac{1}{2}$ considered.

Using this procedure, once a general expression for the form factor is chosen, the form factor approach can be used without additional free parameters. For the analysis presented later, a form factor with $\Lambda_{\text{FF}} = 2 \text{ TeV}$ and $n = 1$ is used. The form factor scale is kept constant to simplify comparisons. Since the scale is well above most of the scales shown in plots, the effect of the form factor on observables is negligible.

Alternative formulations of the form factor are possible. For example in [100] the form factor

$$\mathcal{F} = \begin{cases} 1 & m_{VV} < \Lambda_F \\ \left(\frac{\Lambda_F}{m_{VV}}\right)^4 & m_{VV} > \Lambda_F \end{cases} \quad (3.31)$$

is used.

Cut-off

The cut-off method, also called ‘‘event clipping’’, removes all anomalous coupling contributions above a certain fixed energy [91]. It can be understood as the extreme limit of a form factor, which has no suppression at all below the form factor scale, but maximum suppression (restoring the SM prediction) above the form factor scale. It can be written as:

$$\mathcal{F}_{\text{cut}} = \theta(\Lambda_C^2 - s) \quad (3.32)$$

K-Matrix and T-Matrix

The idea of the K-matrix approach [101] is to project a unitarity-violating amplitude back on the Argand-circle. The projection uses angular-momentum eigenamplitudes, that are transformed as

$$A'_i = \frac{A_i}{1 - iA_i}. \quad (3.33)$$

The leading behavior in s of this construction can also be reproduced using a complex form factor [102, 103]

$$\mathcal{F}(s) = \left(1 - i\frac{s^2}{\Lambda_{\text{FF}}^4}\right)^{-1}. \quad (3.34)$$

A recent extension of the K-matrix approach is the T-matrix formalism [104].

Diboson Production

Diboson production is actively investigated both in experimental analyses and theoretical calculations. An overview of the existing measurements and recent developments is given in Section 4.1. The theoretical description and previous works leading up to and during this thesis are discussed in Section 4.2.

4.1. Experimental Status

Diboson production is measured at several collider experiments. The first observation of pair production of massive bosons was at LEP in $e^+e^- \rightarrow W^+W^-$. In this process the existence of triple gauge couplings was confirmed [105]. The production of W^+W^- and Z boson pairs was used to set limits on anomalous triple gauge couplings. An overview of the diboson measurements at LEP and resulting limits can be found in [106]. The Tevatron measured diboson production in multiple channels, including WZ production in fully leptonic [107–110] and semileptonic decays [111–113].

4.1.1. LHC Experiments

The LHC led to measurements of many processes in proton collisions. An overview is shown in Fig. 4.1, where the large range of cross sections from elastic and inelastic pp interactions down to vector bosons scattering is visualized. The total cross section of the diboson processes (center) is of the same order of magnitude as top pair production or Higgs boson production. When decays are considered and analysis cuts are applied, these cross sections reduce significantly such that many of them are statistically limited.

There is an ongoing program to measure the production of boson pairs by both the ATLAS and CMS collaborations. A selection of diboson measurements by ATLAS is shown in Fig. 4.2. For WZ production, there are measurements in several decay channels of the electroweak bosons. Each of the final state bosons can decay either to leptons or hadrons. The decay channel is labeled depending on how many of the two final state vector bosons decay hadronically. For zero, one or two bosons decaying hadronically, it is called fully leptonic, semileptonic and fully hadronic, respectively. The fully leptonic decays are studied in [115–120]. They have only minor background from other processes, but at the same time have a smaller branching ratio than the (semi-) hadronic channel and are therefore limited by statistics in the high- p_T region. Semi-leptonic decays are studied in [80, 121–125]. In these channels uncertainties arise due to the large background from single vector boson production in association with jets and top production, where the jets can be miss-identified to originate from a vector boson decay. The larger branching ratio of the weak bosons to hadron leads to a larger rate and,

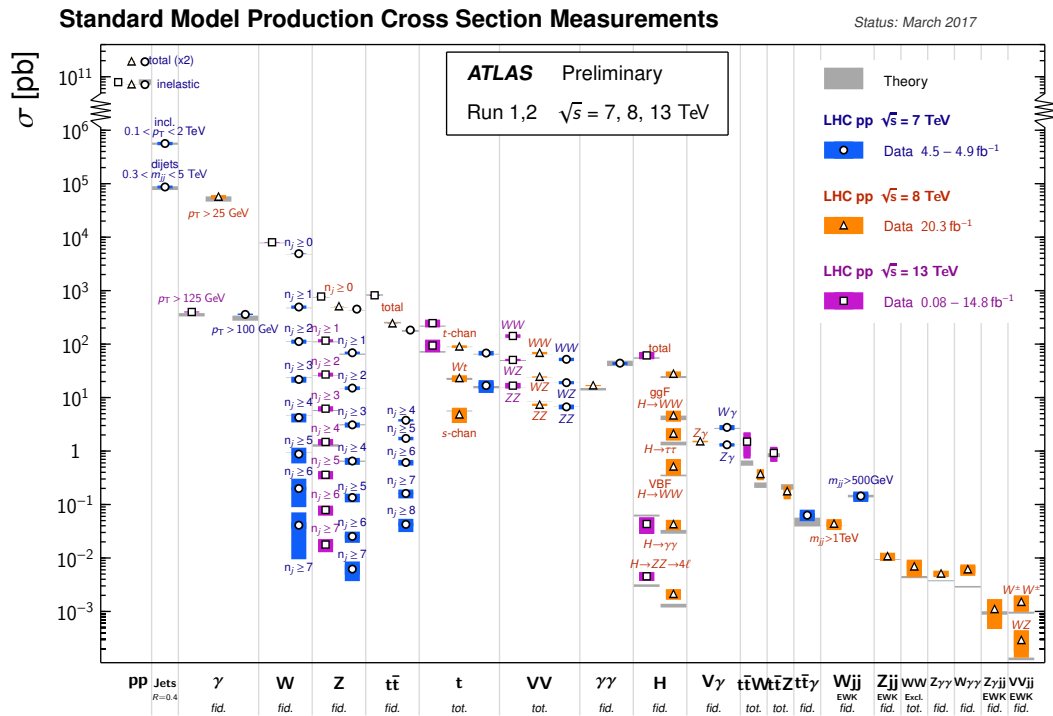


Figure 4.1: Overview of measured SM processes at ATLAS, from [114].

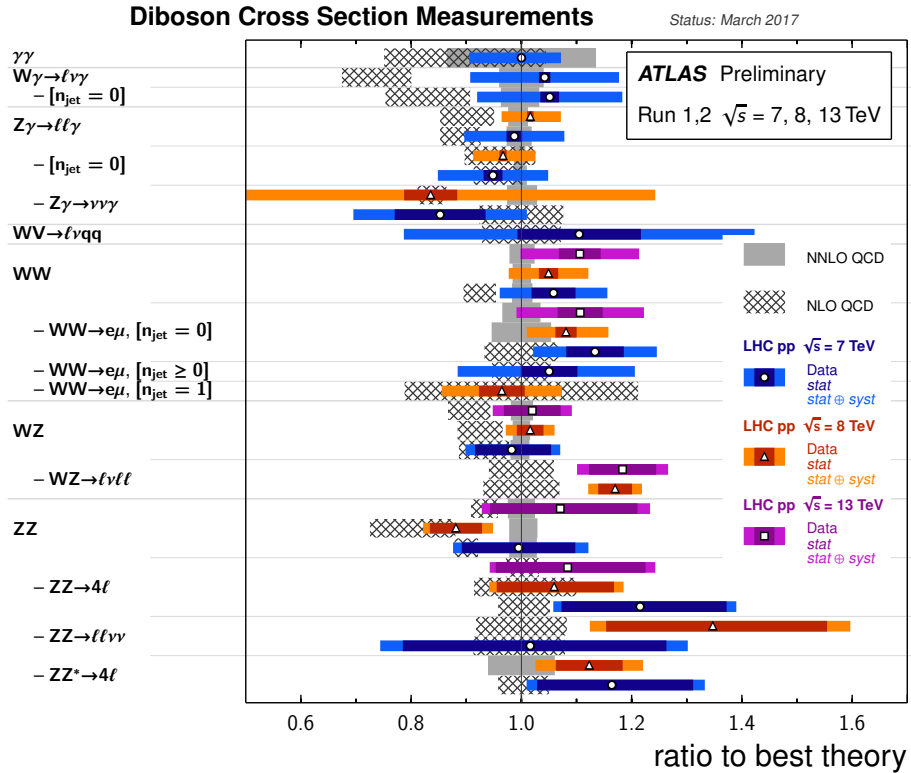


Figure 4.2: Measurements of diboson production by ATLAS, from [114].

in combination with modern subjet analysis techniques, the semileptonic channels are very competitive compared to the fully leptonic decay channels.

Diboson production is also of interest for searches of new heavy resonances, since e.g. a W' boson can be detected through its decay to vector boson pairs [126–131]. Limits on masses of these resonances are currently around 2 TeV [131].

4.1.2. Anomalous Couplings

Many of the previously cited measurements of diboson production also give limits on anomalous couplings. Since individual processes are only sensitive to a subset of operators, one has to combine many analyses to set a limit on a complete operator basis.

Several groups [79, 132–134] publish global fits using the published measurements. The differences between those fits in general are the used datasets and the choice of basis for the fit. The fit results for the allowed range of operator couplings are compatible within a factor of two, such that the qualitative behavior and results found here do not depend on the detailed limits considered. The analyses presented in this thesis mostly use numerical values inspired by the limits presented in [79].

One of the most recent and strictest limits on anomalous couplings in WZ production can be found in [80], where the $l\nu q\bar{q}$ final state is studied. A boosted vector boson ($p_T > 200$ GeV) decaying to a “fat jet” is considered and additional jet radiation above 80 GeV is vetoed. Additional angular and separation cuts are used to ensure a “back-to-back” configuration of the two vector bosons.

The LHC continues to run and upgrades to the detectors are planned. Thus, both systematic and statistical uncertainties will improve further and even more precise measurements and more stringent limits are to be expected in the future.

4.2. Theoretical Status

The recent history of phenomenology in theoretical particle physics is dominated by the NLO revolution. NLO calculations were automated and are now readily available for many processes [135]. Besides the automated calculations of a lot of basic processes, also challenging processes were calculated at NLO and used for phenomenological analyses, for example diboson production in QCD with two additional jets [136–140]. In the past few years these efforts were extended and NNLO calculations of many relevant LHC processes were published.

Beyond fixed order calculations there are many improvements to parton showers and soft QCD, which improve the quality of predictions for processes at hadron colliders. Most recent results include NNLO QCD corrections matched to a parton shower, e.g. in Drell-Yan lepton pair production [141, 142]. An overview of general purpose Monte Carlo programs can be found in [143].

4.2.1. Diboson Production

A review of calculations of diboson processes can be found in [144]. WZ production was first calculated in [145] and used to study anomalous couplings in [146]. WHj production at NLO QCD was also studied in [147, 148].

Recently, differential NNLO QCD calculations of all diboson production processes were presented, including most recently WZ production [149, 150]. This is based on the calculation

of the two-loop amplitudes for two massive bosons [151, 152] which led to the calculation of all diboson processes at NNLO in the MATRIX framework [153–158]. Sizeable corrections come from the gg initial state, which is enhanced by up to 100% at two loops and was investigated e.g. in [159–164].

Also NLO electroweak corrections are known [165–170]. An important effect are *Sudakov logarithms* [48, 49]. They appear, since the real radiation of massive bosons can be identified and is treated as a different process and therefore does not cancel logarithmic term as in the massless case. Their shape at NLO is [165]

$$\frac{\alpha}{2\pi} \log^2 \left(\frac{p_{\text{TV}}^2}{M_V^2} \right). \quad (4.1)$$

These logarithms can reach more than 20% in the tails of distributions. Another aspect of electroweak corrections is the photon induced production of vector boson pairs, which dominates the electroweak corrections for WZ production in the study in [165].

4.2.2. Previous LoopSim Analyses

LoopSim was published in [26, 50], where Z production with an additional jet (Zj) was studied. It was found that dijet type events with the radiation of a soft Z boson lead to sizeable enhancements. In Zj production the NLO K-factor of $H_{\text{T,jets}}$, the sum of the transverse momenta of all jets, grows up to a factor of 100 at $H_{\text{T,jets}} = 1.5$ TeV. The LoopSim approximation of the NLO corrections is able to reproduce this. Combining $Z + \{1, 2\}$ jets at NLO gives \bar{n} NLO corrections to Zj production, which shows K-factors around 2 for most observables. For this study LoopSim was interfaced to MCFM [171, 172].

LoopSim was interfaced to VBFNLO to study different diboson production processes: WZ [173], WW [174] and ZZ production [175]. In this thesis, the interface introduced in these publications is used. A representative result for LoopSim corrections can be seen in Fig. 4.3. It shows the p_{T} of the hardest lepton in W^+W^- production at LO, NLO and \bar{n} NLO. The corrections at \bar{n} NLO reach around 25% for high- p_{T} events. The \bar{n} NLO result is outside of the NLO scale band. A jet veto (right) reduces the higher order corrections and renders them negative. It also reduces the scale dependence. Similar observables and jet vetoes will be studied in Chapter 6.

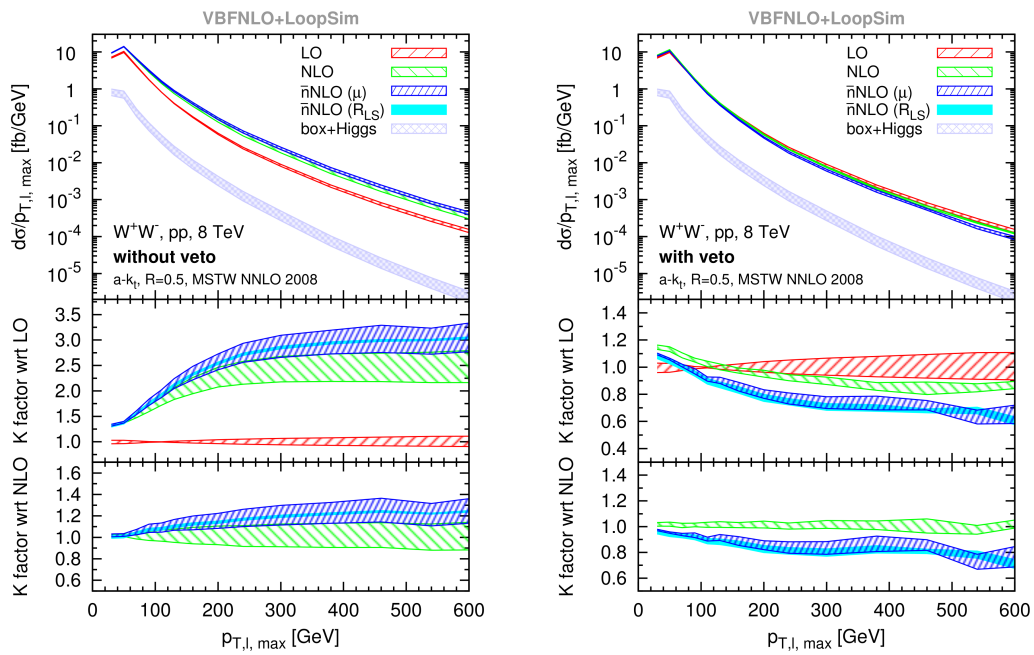


Figure 4.3: VBFNLO interfaced with LoopSim shows sizable corrections on top of NLO for WW production. A jet veto leads to negative corrections. From [174].

Implementation in VBFNLO

VBFNLO is a fully flexible parton-level Monte Carlo program with a focus on hadron collider processes involving electroweak bosons, including diboson and triboson production as well as vector boson fusion and scattering. Many of these processes are also available in combination with additional jets. Leptonic decays and full off-shell effects are included. Cross sections including NLO QCD corrections are calculated efficiently and anomalous triple and quartic gauge couplings are implemented for many processes. VBFNLO is currently released in Version 3.0.0beta4 [176], which corresponds to the code version used for this thesis. It is a collaborative effort with many authors and several published versions [27–29].

This chapter will introduce the structure of VBFNLO in Section 5.1. Methods to improve convergence and numerical stability of the Monte Carlo integration will be discussed in Section 5.2. Changes to the core VBFNLO code as part of this thesis include the introduction of a new random number generator that is described in Section 5.3 and the implementation of parallelization using MPI, which is covered in Section 5.4. Section 5.5 covers the testing and validation procedure for these changes. Finally, Section 5.6 will introduce the interface between VBFNLO and LoopSim.

5.1. Structure of VBFNLO

The goal of the VBFNLO program is to provide predictions for differential distributions of observables at the LHC including NLO QCD corrections. To this end, Monte Carlo integration (Section 5.1.1) is used to integrate the phase space numerically.

The main routine of VBFNLO has the following parts:

1. initialize the program,
2. read input files for masses, couplings, integration settings, cuts,
3. calculate dependent physical quantities like branching ratios,
4. initialize phase space mapping and amplitude for the given process,
5. calculate cross section,
6. output cross section and histograms.

The program calculates the different contributions to the cross section separately:

- born amplitude,
- virtual corrections,
- real emission.

Depending on the process, each of these contributions can be again split using different phase space mappings or different types of amplitudes. For the virtual corrections a typical differentiation is using the maximum number of external legs on the loop to integrate amplitudes of different numerical complexity individually.

For each of these contributions a Monte Carlo integration is started that integrates the cross section by calculating the amplitude at many phase space points. For a certain phase space point the procedure is

1. get random numbers from a VEGAS-driven random number generator,
2. calculate momenta from the random numbers using optimized phase space mapping,
3. apply cuts to momenta, skip to next point if not within cuts,
4. calculate amplitude,
5. add this phase space point to histograms,
6. output event (if needed).

The most complex part is the calculation of the amplitude. All other aspects around it are designed to efficiently calculate the cross section. For this purpose the phase space generator is optimized to give a good approximation of the amplitude and phase space points which do not pass the cuts are discarded early.

5.1.1. Monte Carlo Integration

The main part of VBFNLO is the numerical integration of the cross section. The integration of each contribution is performed using Monte Carlo integration. Monte Carlo integration is a technique to numerically solve an integral by calculating the integrand at random points within the integration space. A review of Monte Carlo methods is given in [177].

Starting with a cross section as defined in Eq. (2.24), the numerical integration can be written as

$$\sigma = \int d\Phi_n \frac{1}{\hat{s}} |\mathcal{M}(p_i)|^2 = \int d\mathbf{r} \frac{1}{\hat{s}} \left| \frac{d\Phi_n}{d\mathbf{r}} \right| |\mathcal{M}(p_i(\mathbf{r}))|^2 \quad (5.1)$$

$$\xrightarrow{\text{Monte Carlo}} \sigma = \frac{1}{N} \sum_{k=1}^N |\mathcal{M}(p_i(\mathbf{r}_k))|^2 \omega_{\text{PS}}. \quad (5.2)$$

The integration measure $d\Phi_n$ stands for the n -dimensional Lorentz-invariant phase space. The amplitude \mathcal{M} is a function of the four-momenta p_i in this phase space. The integration is rewritten in terms of an integration over the n -vector \mathbf{r} , which parametrizes the momenta. This parametrization is called the phase space generator and is constructed to approximate the integrand and reduce the variance of the integrand. Monte Carlo integration then rewrites the integral as a sum over N random phase space points. Each phase space point corresponds to n random numbers \mathbf{r} , which are translated to momenta $p_i(\mathbf{r})$. The weight ω_{PS} contains the Jacobian of the phase space mapping $\left| \frac{d\Phi_n}{d\mathbf{r}} \right|$ as well as the appropriate normalization factors.

The technical problem of the integration can therefore be stated as

$$I = \frac{1}{N} \sum_{i=1}^N f(r_i), \quad (5.3)$$

where f is a function that incorporates the matrix element as well as phase space factors and reweighting factors.

After rescaling, the integration space is assumed to be a d -dimensional unit cube. The mapping between this cube and values of physical momenta in the amplitude is discussed in Section 5.1.2.

Monte Carlo integration is the most appropriate solution for high-dimensional integrals, which can not be solved analytically. It performs better than methods based on regular grids. Iteratively applying 1D integration techniques using grids leads to an integration error which scales as $N^{-2/d}$. For an overview of methods for numerical integration see e.g. [178, 179]. Monte Carlo integration scales as $\frac{1}{\sqrt{N}}$ or to be precise

$$\delta_{\text{MC}} = \frac{1}{\sqrt{N(N-1)}} \sqrt{\sum_{i=1}^N f(r_i)^2 - \frac{1}{N} \left(\sum_{i=1}^N f(r_i) \right)^2} \quad (5.4)$$

This formally outperforms grid-based integration methods for $d \geq 5$ and clearly for the use case in VBFNLO with $d = 12$ and $N = 2^{26}$. A more detailed discussion of the derivation and how to combine Monte Carlo error estimates from multiple runs can be found in [180].

5.1.1.1. Importance Sampling with VEGAS

There are two approaches to improve the convergence of Monte Carlo integration further, which both aim at reducing the variance of the integrand. One option is to favor the regions with the largest contribution to the integral, *importance sampling*, the other one to prefer the region with the largest variance, *stratified sampling*. The generation of integration points is then no longer uniform in the unit cube, but the density is adjusted to minimize the Monte Carlo error, Eq. (5.4).

For importance sampling, the nonuniform distribution of random points is generated by constructing an estimator function $g(x)$ which is designed to estimate the integrand $f(x)$, while at the same time being invertible and thus usable for sampling. There are different techniques to construct this estimator. VBFNLO uses *Monaco*, which was implemented in [181] and is based on VEGAS [182, 183]. The idea of VEGAS is to use importance sampling with an estimator that is a product of 1D estimators:

$$g(x) = g_1(x_1) \cdot g_2(x_2) \cdots g_d(x_d) \quad (5.5)$$

This factorization assumes that the integrand also approximately factorizes. Non-factorizable contributions will reduce the agreement between integrand and estimator and thus the efficiency of the integration. The functions g_i , also called grids, are constructed as step-functions with a fixed number of steps (48 by default) in the unit interval. The values of the steps are determined by collecting the values of the integrand in histograms for each of the random numbers used.

The integration is performed in iterations. During each iteration the integrand value is recorded in histograms. At the end of the iteration the recorded histograms are used as the new baseline for the g_i . To improve numerical stability the adjustment is damped, such that instabilities of individual iterations have less effect.

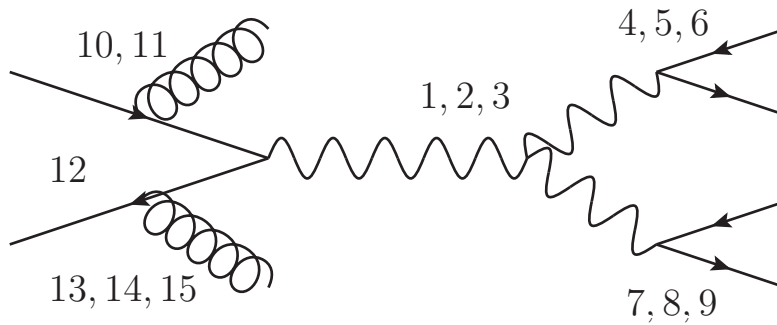


Figure 5.1: Order of generation and mapping of random numbers to kinematical variables for $WZjj$ production.

If the factorization in Eq. (5.5) is correct for the integrand, this leads to a very efficient integration. For real-world integrands this factorization in general only works approximately and there can also be features that are not picked up by the histograms. Typical examples where the VEGAS factorization assumption fails are correlations between variables, like in the integrand $((r_1 - r_2)^2 + m^2)^{-1}$. A collection of alternative algorithms for multi-dimensional integration can be found in the popular package CUBA [184].

5.1.2. Phase Space Generation

Each of the contributions to the cross section (born, virtual corrections and real emission) can be split up into different “phase space mappings” to optimize the integration efficiency and runtime. For example in $W\gamma$ production, the photon can either be emitted from the initial state quark line, the W or a decay lepton of the W . The last case leads to a significantly different phase space, where photon, lepton and neutrino correspond to an on-shell W boson. Using different phase space mappings, multiple momentum combinations, including potential resonances, can be described and efficiently integrated.

For WZ +jets production only one phase space mapping is used. The order in which the kinematical variables are generated is visualized in Fig. 5.1. The mapping is annotated on an example Feynman diagram, while the mapping tries to be general and not diagram specific. First, the invariant mass \hat{s} of the intermediate W^* boson is generated, then the angles for its decay to two bosons. For those again the invariant mass and angles for the decay to leptons are assigned. In the end, the jet radiation is described using rapidities relative to a center-of-mass rapidity as well as transverse momenta. The list of kinematical variables and their mapping to random numbers is given in Table 5.1. The angular distributions are assumed to be flat, while for the boson masses Breit-Wigner distributions are used. For the invariant mass of the diboson system (\hat{s}) a combination of a Breit-Wigner distribution with very large width and a flat background is used. For the jet transverse momenta the assumed distribution is

$$\begin{aligned} r \leq 0.2 &: (0, p_{T\min}), & p_T &\sim r, \\ r > 0.2 &: (p_{T\min}, \sqrt{\hat{s}}), & p_T &\sim 1/r. \end{aligned} \quad (5.6)$$

Here $p_{T\min} = \max\{10 \text{ GeV}, p_{Tj,\text{cut}}\}$ is used, where $p_{Tj,\text{cut}}$ is the minimal jet p_T required by the analysis. Below this transverse momentum value, jets are assumed to not be resolved and therefore need fewer events to be well-modeled.

The choice of mapping distributions is important to have an efficient integration. The difference between the distributions assumed here and the actual scaling of the matrix elements will

Random Number ID	kinematic variable
1	\hat{s}
2	$\theta(V^* \rightarrow VV)$
3	$\varphi(V^* \rightarrow VV)$
4	m_W^*
5	$\theta(V_1 \rightarrow ll)$
6	$\varphi(V_1 \rightarrow ll)$
7	m_Z^*
8	$\theta(V_2 \rightarrow ll)$
9	$\varphi(V_2 \rightarrow ll)$
10	η_{j_1}
11	p_{Tj_1}
12	y_{CM}
13	η_{j_2}
14	p_{Tj_2}
15	$\phi_{j_2} - \phi_{j_1}$
non-vegas	ϕ_{j_1}

Table 5.1: Mapping of random numbers to kinematic variables for the example of WZjj production.

be compensated by VEGAS. This compensation has a limited range. In many cases the distributions to use can not be easily derived from first principles. For example in the high-energy tails of jets, the expected p_T dependence is p_T^{-4} due to the scaling of the propagator. Interferences between amplitudes can lead to terms with a different power and for high invariant masses there is an additional suppression from the PDFs.

5.1.3. Amplitudes

The amplitudes are calculated using the effective current approach and the spinor-helicity amplitude method [185] as implemented in the HELAS subroutines [186] and also implemented in MadGraph [187]. The calculation of the QCD part of the amplitude, including higher order corrections, can be factorized from the EW part of the calculation to a certain extent.

In the code, this factorization is implemented by computing leptonic tensors, which contain the possible combinations of electroweak particles that can be attached to the QCD part of the diagram. For WH production there is only one such combination, which corresponds to the virtual W boson that decays into the W and H boson, which both decay further. In WZ production, besides the virtual W , also the two bosons can be attached directly to the initial quark line. Also for these cases leptonic tensors are precomputed. The electroweak part of the calculation also contains other contributions like non-resonant $V \rightarrow 4l$ decays with bosonic radiation off one of the lepton lines. This factorization is shown with some example contributions in Fig. 5.2.

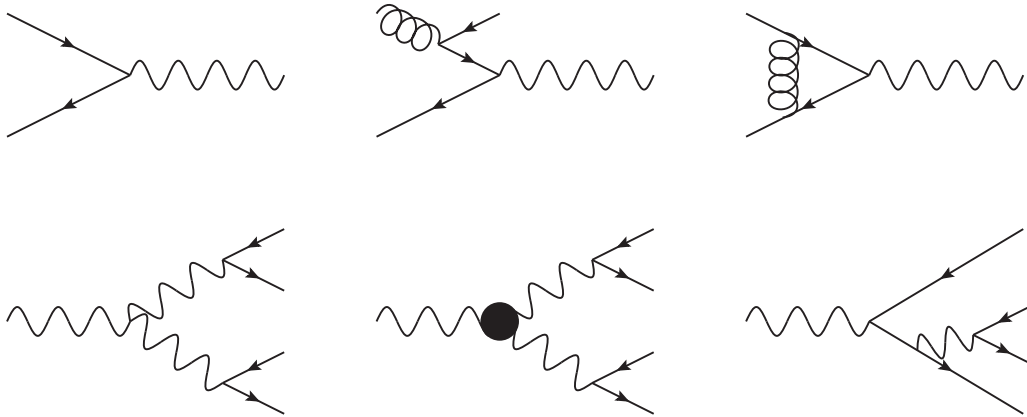


Figure 5.2: The effective current approach allows to factorize the QCD and EW contributions. Using the example of WZ production, the top row lists exemplary born, real emission and virtual corrections QCD amplitudes that can appear in the production of an off-shell vector current. The bottom row shows potential contributions to this current, which include the SM triple gauge coupling, anomalous triple gauge couplings and also other, non-resonant contributions with the same four-lepton final state.

Within this framework, anomalous couplings can be integrated into the leptonic tensors without any modification to the QCD calculation. This allows, for example, verification of the QCD and AC calculation separately. Precomputing and storing the electroweak tensors for repeated use is a significant advantage. It speeds up the calculation and avoids redundancies in the code. The QCD corrections are calculated using the building blocks for one-loop diagrams presented in [188].

5.2. Improving Numerical Stability

To get numerically stable results for the high- p_T tails of distributions, we use two methods. First the number of phase space points in the tails is increased compared to what VEGAS would do based on their contribution to the total cross section. The other technique uses bin smearing for the histograms.

5.2.1. Enhancing Tails

The idea is to favor high- p_T events in the phase space integration more than their contribution to the total cross section would suggest. To achieve this, the statistics in tails of distributions are increased by integrating $d\sigma \cdot w(p_i)$ instead of $d\sigma$, where $w(p_i)$ is a reweighting function. For the LoopSim based plots in this thesis $w(p_i) = H_T^4$ was used to bias the Monte Carlo towards the high- H_T region. Here H_T is the scalar sum of the transverse momenta:

$$H_T = p_{TZ} + p_{TW} + \sum_{\text{jets}} p_{Ti}. \quad (5.7)$$

In this general approach, the reweighting function $w(p_i)$ can be chosen arbitrarily. The error on the integrated cross section will grow, since the importance sampling is now biased away from the region with the largest contribution to the cross section. The reweighting function has to be infrared safe to ensure that the cancellations between real emission and subtraction terms remain intact.

More generally this procedure can be used to get a flat relative error in a certain distribution. To achieve this, the reweighting function has to be chosen as the inverse of the corresponding distribution.

5.2.2. Bin Smearing in VBFNLO and LoopSim

For the NLO calculation, a subtraction scheme is used to cancel the real emission singularities. Since the subtraction terms and the real emission appear in phase spaces with a different dimension, observables can have slightly different numerical value for both event types, even when they are IR-safe. If the observable value is close to a bin boundary in a histogram, it can occur that the real emission and subtraction terms end up in different bins. The cancellation then no longer works and the histogram bin values get significant shifts which also increase their Monte Carlo integration error. The resulting histograms then can show neighboring bins with large positive/negative spikes.

This issue arises not only for NLO subtraction, but also for “looped” events with LoopSim, where the original event and its looped counterpart can contribute to different observable values.

Bin Smearing Approaches

The general idea of bin smearing is to record events in more than one bin, especially when they are close to a bin boundary. This smoothes out the bin boundary and restores the cancellation between contributions that are close.

Smearing also appears in experiments, where the uncertainty of a measurement leads to entries appearing in a certain distribution around the true value.

The prescription on how to smear bins is not unique. To record the weight of an event in a histogram using smearing, instead of only using the histogram bin at the calculated observable value x_0 , a function $f(x - x_0)$ is used that defines the contribution of an event to the surrounding observable values x . The weight entering a certain bin is then the integral over this function in the range of the bin.

Potential smearing functions are:

$$f_{\text{nosmearing}}(x) = \delta(x - x_0), \quad (5.8)$$

$$f_{\text{linear}}(x) = \begin{cases} \frac{1}{D}, & \text{if } |x - x_0| < \frac{D}{2}, \\ 0, & \text{otherwise,} \end{cases} \quad (5.9)$$

$$f_{\text{quadratic}}(x) = \begin{cases} -\frac{4}{D^2} |x - x_0| + \frac{2}{D}, & \text{if } |x - x_0| < \frac{D}{2}, \\ 0, & \text{otherwise,} \end{cases} \quad (5.10)$$

$$f_{\text{gaussian}}(x) = \frac{1}{\sqrt{2\pi D^2}} e^{-\frac{(x-x_0)^2}{2D^2}}. \quad (5.11)$$

The naming of the linear and quadratic smearing functions refers to their integrated form, which is responsible for how the weight in a bin scales with the distance to its border. All non-trivial smearing functions have some parametrization for the width D of the smearing. This distance should typically be on the order of the bin size. The choice of the smearing function should reflect the distribution of values. For many measurements, a Gaussian distribution is assumed. For a Monte Carlo implementation one of the more basic functions is preferable.

They are faster to run than the exponential and also ensure that only a maximum of two bins get contributions from an event, assuming the smearing width D is less than the bin width.

Bin Smearing in VBFNLO

VBFNLO provides linear smearing in its internal histogram routine. Events at an observable value of x_0 that have a distance of less than $D/2$ from the next bin boundary x_{bin} are recorded with a reduced weight of $w' = w \cdot \left(\frac{1}{2} + \frac{|x_{\text{bin}} - x_0|}{D}\right)$ and with the remaining weight of $w'' = w - w'$ in the neighboring bin.

Starting with version 3.0 linear bin smearing is enabled by default (via the `SMEARING` variable) and uses a smearing width D (`SMEAR_VALUE`) of 10% of the bin width. For the plots in this thesis a smearing value of 40% was used to generate smoother distributions of jet observables.

Bin Smearing in LoopSim

The published LoopSim library does not have bin smearing implemented. For this thesis linear smearing was implemented in LoopSim and used for all plots with a smearing width of 20% of the bin width.

The use of bin smearing is very valuable to produce smooth distributions in fixed order calculations, but it has potential downsides. If the smearing width is larger than the bin width, narrow features of the distribution can get smeared out and vanish. Also the smearing can introduce a shift in steep distribution. For the comparison between different theoretical predictions and to data, it is important to ensure that the same smearing procedure is used.

5.3. Random Number Generator

As discussed in Section 5.1.1 the main part of VBFNLO is Monte Carlo Integration, which is based on the idea that the matrix element is evaluated at random phase space points. True randomness, for example from a measurement, can only be generated slowly and while useable, it is not needed for numerical integration. Pseudo random numbers, that are generated by an algorithm, are faster to generate and can have “sufficient randomness” for Monte Carlo integration.

Criteria for a pseudo random number generator (RNG) include:

- quality of random numbers
 - no (relevant) correlations, also for high-dimensional phase spaces
 - long period N , such that at most \sqrt{N} numbers are used
 - uniformity
- ease of implementation/seeding
- speed

Different methods exist to give quantitative measures of the “quality” of random numbers. A popular choice is TestU01 [189], which is a collection of statistical tests for random number generators. This includes *BigCrush* as the state-of-the-art test used by many authors to assess the quality and behavior of their RNGs.

5.3.1. Choice of Random Number Generator

VBFNLO versions before 3.0 provide a choice of two random number generators:

- *RANMAR*, by Marsaglia and Zaman [190], internally also called MZ and
- Sobol Sequences [191] based on the Implementation in [192], a Quasi random number generator, discussed in Section 5.3.2.

To parallelize the implementation, a random number generator is needed, which can be used for a fast generation of parallel random number streams. This requirement leads to the inclusion of two new RNG choices:

- *xoroshiro128+* [193, 194],
- the `random_number` function as provided by the compiler.

The latter is implemented in GNU Fortran 7 and newer using *xorshift1024* [195], while versions 4.8 to 6 are based on the KISS-RNG [196].

The default RNG in VBFNLO is RANMAR. A runtime comparison of the different RNGs can be found in Section 5.4.4.

The *xoroshiro128+* random number generator

For parallel environments, *xoroshiro128+* is now recommended in VBFNLO. *xoroshiro128+* is based on the family of xorshift generators [195]. A seed given by the user is used to compute an internal *state*. For *xoroshiro128+* the state consists of 2 integers of 64 bit. On these an iteration step is run, which evolves the state and generates a stream of output values. The state of 128 bits is minimal compared to the achieved period length of the output of $2^{128} - 1$. In comparison, *RANMAR* stores its state in 97 floats of 64 bits and has a more involved initialization and iteration step, while providing less randomness “quality” based on the modern tests mentioned before. The iteration step of *xoroshiro128+* consists only of three bitshifts, four XOR operations and one addition and is therefore very efficient. For the implementation, the original C-code [194] was used and extended to integrate it with the existing code, especially for seeding and randomness output in blocks.

Besides being significantly faster, *xoroshiro128+* also allows to produce multiple independent streams of random numbers starting from a common seed. After seeding the state, it is possible to jump ahead in the random number sequence in steps of 2^{64} , such that 2^{64} independent streams can be generated. This feature will be used for parallel integration to have multiple random number streams from a common seed.

5.3.2. Quasi Random Numbers

An alternative choice for Monte Carlo integration is to use quasi random numbers. In contrast to pseudo random numbers they do not try to mimic randomness, but show a strict structure and aim at providing a homogeneous coverage of the integration region. It can be shown that the error of the numerical integration using quasi random numbers scales as $\frac{1}{N}$, compared to $\frac{1}{\sqrt{N}}$ for pseudo random numbers.

In VBFNLO it is possible to use Sobol sequences, which are quasi random numbers that are commonly used for high-dimensional integration since they provide multi-dimensional equi-distribution. In practice, the convergence of the integration is not significantly improved

when using Sobol sequences compared to pseudo random numbers. The convergence of quasi random Monte Carlo integration is widely studied. As shown in [197] the convergence depends on the integrand. For smooth (low-variance) functions quasi-random numbers are favored, while for non-smooth functions their advantages are less clear.

Furthermore, for small integration errors in a realistic calculation, it is best to use some parallelization, either via MPI or by starting multiple runs with different seeds for a pseudo random generator and combining their results. VBFNLO currently does not support seeding of quasi random numbers.

5.4. Parallelization

Modern computers have processors with many cores – from typical desktop machines with 4 cores to highly energy-efficient cluster machines with more than 100 cores. On computing clusters often more than 1000 cores can be used simultaneously. The implementation should thus try to make use of these available resources and run on multiple cores. A single run can be sped up by distributing its workload on multiple CPU cores.

Most of the VBFNLO runtime is spent in the Monte Carlo integration and in particular in the evaluation of the integrand. Monte Carlo integration is essentially the calculation of a sum. Since the elements of the sum are independent, this is trivially parallelizable, by calculating all summands individually and then combining them in a final sum. As part of this thesis, the numerical integration within VBFNLO was reimplemented to make use of multiple cores.

5.4.1. Message Passing Interface

There are many different frameworks that make parallelizing numerical code easier. The most common ones are OpenMP [198, 199] and Message Passing Interface (MPI). OpenMP by design is limited to one physical machine and only makes use of the cores of that machine. The MPI specifications were first published in 1994 [200] and since then extended several times leading to the current standard [201]. MPI can, in most implementations, run on several machines and combine their cores, which allows scaling to complete computing clusters. The implementations differ, since OpenMP handles the communication implicitly and uses decorators on loops that then spawn threads to work on subparts of the algorithm. In MPI the communication has to be implemented explicitly. This makes the code more verbose and at the same time highlights at which stages of the computation there is communication between the individual processes. For a codebase that was not designed with parallelization in mind this explicit implementation can make shared state and performance bottlenecks more obvious.

Due to the greatest potential when running on more than one machine, MPI was chosen for the parallelization in VBFNLO. For a discussion of alternatives see Section 5.4.3. Usually cluster operators provide an MPI installation that is configured to make the best use of the existing infrastructure of that cluster, like choosing the fastest communication backend (Shared Memory, Ethernet, Infiniband, ...) or adjusting communication strategies to the performance characteristics and topology of the cluster.

5.4.2. Parallelizing VEGAS

VBFNLO uses the VEGAS algorithm as presented in Section 5.1.1. VEGAS uses importance sampling and adds some complexity over a naive Monte Carlo integration. The summation of

the Monte Carlo integration no longer consists of uncorrelated summands. The introduction of the grid for importance sampling as well as adapting the grid adds dependencies between phase space points and amplitudes at previous points.

Nevertheless VEGAS is easily parallelizable. It is ordered in iterations and information exchange can be reduced to the steps between iterations. The inner-most loop of VEGAS within one iteration is a simple Monte Carlo sum, where a function (the matrix element) is evaluated at a set of (pseudo) random phase space points and cumulated. During this summation, the weights are recorded in a binned histogram that is used to generate optimized grids to improve the importance sampling. This overhead data needs to be shared between parallel running jobs. It is possible to limit the data exchange to the steps between VEGAS iterations, such that for the majority of the calculation time no data transfer is needed. Furthermore, the total data exchange is only a few kilobytes and the transfer time was measured to be negligible even for very fast runs. A more involved parallelized version of VEGAS is presented in [202], where also different approaches to the parallelization are discussed.

5.4.3. Design of the Implementation

The goal of the implementation was to have parallelization as an option in the main `VBFNLO` code. Support for MPI should be optional, such that users can compile and use `VBFNLO` with or without a MPI library. To improve maintainability the changes should be minimal and as backward compatible as possible. There should be no changes to input and output as far as possible. For validation runs with and without MPI should lead to identical results.

Using these conditions a parallel implementation of `VBFNLO` was designed and implemented as part of this thesis. For the configure step, a flag `--enable-MPI` was added. This triggers `#ifdef` statements in the code, which switch between the newly added MPI and non-MPI versions of some code sections. The initialization and interfacing of the random number generators was adjusted to support both cases and for the histogram and cross sections the data structures were adapted to be more easily passable between different parallel workers. As a side effect the memory usage of the histograms was optimized and some duplications removed.

The overall idea is that each MPI worker process runs independently. This means that each MPI worker runs the full initialisation phase, reads the input files and calculates the physical parameters as needed. There is one master process. The difference to the other workers is, that this master outputs the results to the screen and other output files, while the other workers are mostly silent. For the parallel code sections, each worker determines which subrange of the phase space points they are supposed to cover. For this the worker ID and the total number of workers is used to split the total number of points equally between all workers.

After the computation, the results (cross section, histograms, grids) are exchanged, such that each worker has the same result that corresponds to the full statistics computed by all workers. Since only summarized data, like histograms and binned random number information of VEGAS is exchanged, the amount of data is fairly small (kilobytes) and has negligible overhead compared to the runtime of a typical calculation. For histograms and the cross section, the Monte Carlo error estimate of Eq. (5.4) is used. Each process calculates $\sum_i f(r_i)$ and $\sum_i f(r_i)^2$ for their subset of points and the resulting sums are combined at the end of each iteration to cover the full statistics.

For the communication, mostly the command `MPI_ALLREDUCE` is used. With this command, both the combination (summing) of subresults as well as the distribution of the final result are covered by one call to the MPI library and the summation can be distributed over multiple machines for highly-parallel runs.

Most MPI commands are split up in a separate Fortran90 module `vbfno_mpi`, that can be found with the published source code in [176]. Besides this new module only the main integration loop contains MPI specific code. The benefits of parallelization are thereby independent of the process or custom extensions to VBFNLO like new processes, phase space changes or additional histograms.

Identical results for non-MPI and MPI with different number of workers

To validate the parallel version, the implementation is designed to lead to numerically identical results for runs without MPI and with MPI for different numbers of workers. To achieve this with the RANMAR generator, the random numbers used are chosen to be the same in each configuration. If multiple workers run, they all generate the full set of random numbers necessary and only use their assigned subset. This guarantees that the state of the pseudo random number generator (PRNG) is identical to a non-MPI run. There are potential numerical differences appearing due to the different order of the summation. Effects of the numerical differences between different runs are only at the order of the machine accuracy. When runs with more than one iteration are used those differences grow significantly, since the importance sampling gets a different numerical input, which leads to significantly different phase space points and thereby results for the amplitude.

This dependence on the order of summation is well-studied. Starting with Kahan summation [203] several techniques were developed, as can be seen in the review [204]. Those require access to all summands and would thus increase the memory/network usage and reduce performance, compared to the naive summation implemented here.

With the *xoroshiro128+* RNG the performance is optimized and only the minimal necessary number of random numbers is generated. Therefore, multiple runs will use different random numbers than a single long run. The agreement of different RNGs was verified independently of the parallelization.

Limitations

There are multiple implementations of the MPI specifications. For this thesis, OpenMPI [205] in combination with GFortran was used, although the code adheres to the MPI standard and is expected to work with other MPI libraries and compilers. Additional validation of the numerical results is needed for new library/compiler combinations.

The phase space points are split evenly over the available worker processes. This assumes that the speed of the workers is approximately equal. For heterogeneous clusters the work should be split up according to the worker speed. A more advanced task distribution algorithm could also deal with workers failing or dynamically changing the number of cores during the integration.

Parallelization is disabled for runs requesting event output, since for that case multiple processes writing to the same file would need to be handled. This would require some kind of file locking, making the process IO-limited and thus reducing the performance to that of a single core. Alternatively, separate outputs for each job could be created and combined in a

post-integration step. The recommended procedure to get event output is to first run with disabled event output but high statistics to generate an optimized grid. Then this grid can be used for multiple runs with different seeds to efficiently generate events.

Alternatives

Even without the MPI implementation, VBFNLO can be run on multiple cores. For this, usually first a long run with many VEGAS iterations is used to generate an optimized integration grid file. Then several jobs with different random seeds are started using this optimized grid and only one iteration. This is the preferred process for cases in which MPI can not be used. The advantage of MPI is that also the grid generation can be parallelized and a separate step to combine the output of several runs is not needed.

For a given process there is a certain lower limit to the number of phase space points. Below this limit the phase space is not appropriately filled and thus the integration result is not trustworthy and often does not converge towards to correct result. For complex processes with a large number of final state particles this limit can be so high that for a run on a single core the total runtime becomes unpractical. In these cases, the MPI implementation allows to use the total statistics of all workers to fill the phase space and combines the results at each iteration to improve the integration grid and produce a reliable result.

For the edge case, where the integration statistics are just sufficient to fill the complete phase space, there are ideas on how to combine runs, when only a small number of them have unstable results. For this, outliers are detected and removed. Nevertheless, these methods are less stable than the correctly parallelized VEGAS integration.

Other Monte Carlo Generators also consider to or already provide parallelized implementations. MCFM [171, 172] was parallelized [206] using OpenMP and is shown to scale up to O(100) cores using an Intel Phi processor. For Whizard [207, 208] an implementation using MPI is planned as part of VAMP [209]. An implementation of HELAS routines on GPUs was demonstrated [210].

5.4.4. Runtime Improvements to VEGAS and RNGs

Timings are taken to measure the contribution of VEGAS and the random number generator to the total runtime of VBFNLO and to assess the scaling with the number of cores. For an example, the total run for process 100 (VBF-H) with 2^{22} points at LO takes 73 s. Those are split between amplitude (49 s), phase space (20 s) and VEGAS/RNG (4 s). For more complicated processes in general the amplitude will become even more dominant. In the parallelized version, the VEGAS/RNG phase grows substantially and could be a bottleneck.

In the VEGAS implementation a significant performance improvement was achieved. VEGAS calculates the bin in its optimized grid to map uniform random numbers to the desired distributions. This mapping was computed twice: *uniform* \rightarrow *weighted* and after the amplitude *weighted* \rightarrow *uniform*. The back transformation was implemented as a linear search in an array and thus very inefficient. By replacing the back transformation with a lookup of the cached information of the first transformation the runtime of VEGAS was improved by a factor 4.

A first naive MPI implementation was designed to split up the phase space points such, that the random numbers used for a parallel run were identical to the run on a single core. This makes validation easier, since the numerical output is then independent of the number of cores used. On the other hand, the RANMAR random number generator does not allow to “skip”

RNG	Runtime / s
RANMAR	31
Sobol	16
builtin/KISS	30
xoroshiro128+	22

Table 5.2: Comparison of the random number generator runtime for 2^{26} points. For this comparison the calculation of matrix elements and phase space weight are disabled. For a discussion of these RNGs, see Section 5.3.

Number of cores	Runtime / min	
	naive MPI	improved MPI
1	230	217
15	25	17

Table 5.3: Comparison of the total runtime of 2^{28} points in process 100 (VBF-H) at LO with the naive MPI implementation and a version including the improvements discussed in this section. Ideal scaling of the 1-core result would lead to 15 min runtime. The improved version is able to close the gap to ideal scaling from 40% to 20% and speeds up the single-core execution by about 5%.

blocks of random numbers, such that each process had to calculate the full random number space, while it only uses a fraction.

For many cores the runtime can be improved by only generating as many random numbers as are actually used and using a faster random number generator. Table 5.2 shows a comparison of the runtime of the RNGs available in VBFNLO as introduced in Section 5.3.1. *xoroshiro128+* is implemented as a fast RNG to speed up the MPI runs. The fastest generator is the quasi random Sobol sequence. The total runtime of VEGAS and the RNG is 40% slower when using RANMAR compared to *xoroshiro128+*.

Combining the improvements to VEGAS and the RNG discussed here, the total runtime of both a single core and especially a highly-parallel run are significantly improved as shown in Table 5.3.

Scaling results

Ideally, the runtime should decrease as the inverse of the number of cores used. This corresponds to a linear increase with the number of cores n of the speedup

$$S_n = \frac{T_1}{T_n}, \quad (5.12)$$

where T_1 is the runtime on one core and T_n the runtime of the same setup with the same number of phase space points using n processes in parallel.

In a real implementation, there is a finite amount of overhead that can not be parallelized. This includes initialization and input/output as well as communication/synchronization between

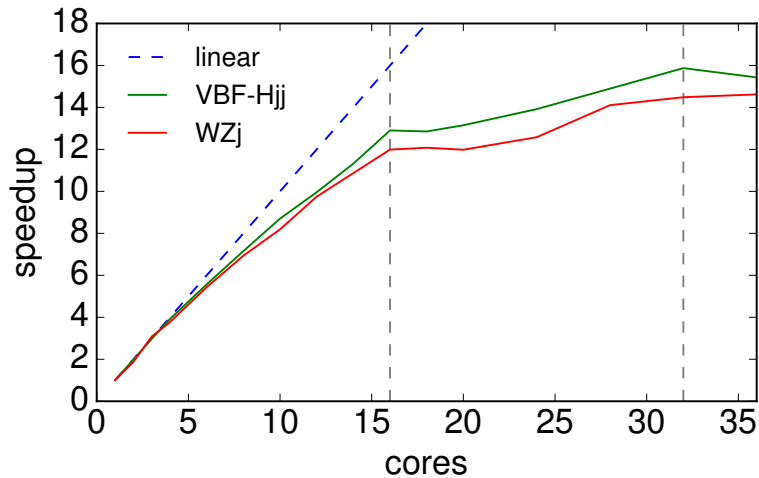


Figure 5.3: Speedup as defined in Eq. (5.12) over the number of cores. As a comparison a dashed line shows the ideal scaling. This ideal case is reached for a small number of parallel processes. Up to 16 cores still reasonable runtime improvements are observed, while the performance decreases once hyper-threading is used above 16 cores.

the processes. The resulting scaling then is described by Amdahl’s Law [211]:

$$S_{\text{overall}} = \frac{1}{(1-p) + \frac{p}{s}}, \text{ where} \quad (5.13)$$

- S_{overall} : resulting speedup of the complete program
- s : speedup of parallel part of the code
- p : fraction of execution time spent in the parallel code section

In the implementation in VBFNLO the overhead for additional cores should be minimal, since communication and synchronization happens only once for each iteration and the amount of exchanged data is small.

Before the numerical integration, there is an initialization phase, that each process runs independently. It consists of reading input files, setting up the run environment for the integration and also calculating some physical variables, like branching ratios. This typically takes about 2 – 3 seconds due to numerical integration of decay phase spaces for the branching ratios. The output of the final results, which takes less than a second, is also not parallelized. The overhead can be extracted by reducing the number of points for the main integration step and was measured to be on the order of 3 seconds, depending on the IO latency.

To test the scaling, the runtime is recorded for different numbers of parallel processes used by MPI. This test is performed on an Intel Xeon E5-2630v3 processor, which has 16 physical cores and using hyper-threading offers 32 logical cores to the operating system. Using one core of this processor gives a runtime of 69 hours for 2^{32} phase space points in VBF Higgs boson production and 32 hours for 2^{27} points in WZj production. The speedup for these processes is shown in Fig. 5.3. Different physical processes are used to investigate, whether the scaling depends on the complexity of the amplitude. The runtime is reduced with nearly optimal linear scaling up to around 6 cores. Beyond this value, a suppression compared to optimal

scaling arises that is, depending on the process and setup, about 30% for 16 parallel processes. Hyper-threading is known to give little improvement for CPU-bound tasks and has a strong dependence on the specific workload. This can be seen with a flat or even decreasing speedup above 16 processes due to multiple processes competing for the available cores and caches.

The different physical processes show overall similar scaling behavior. The speedup is best for the processes with the most time intensive amplitudes (WZj). This is expected, since the relative contribution of the parallelization overhead is smaller.

5.4.5. Potential Improvements

There are several aspects in which the performance of the code could potentially be improved. Currently, one phase space point is generated and then passed through the whole program, from phase space and cuts to amplitudes and histograms. Instead, one could generate a longer list of random numbers and have the different code blocks work on them in bunches. This would allow to make use of the growing hardware support for Single-Instruction-Multiple-Data (SIMD). The AVX2 instruction set of the current processor generation in the best case can perform 8 simultaneous floating point operations. Working on bunches would also improve cache locality. For loop amplitudes the code in general is larger than the CPU cache and therefore is most likely limited by memory access speed. A smaller amount of context switches of the CPU between random number generation, phase space and amplitude can reduce the number of memory accesses and associated runtime.

Investigation of the non-optimal scaling in Fig. 5.3 showed that this is mostly due to the different runtime of the individual processes. While all subprocesses work on the same number of phase space points, they show runtime differences of up to 50% already below the hyper-threading bound. This is potentially due to the configuration of CPU scheduler and processor performance settings like Intel's Turbo Boost. The MPI implementation could be improved by choosing the number of phase space points handled by a given worker more dynamically and adapt it to their runtime. For running on heterogeneous clusters this is even more relevant. The naive equi-distribution of phase space points limits the runtime to the runtime of the slowest machine.

Loop scheduling in parallel computing is an active topic in the computer science community and there are many suggested algorithms available that behave significantly better than the now implemented naive Chunk Self-Scheduling. Popular choices are discussed and evaluated in e.g. [212, 213].

5.5. Testing and Validation

To make sure that new changes to the code do not have unexpected side-effects, there is a list of regress tests. A regress test is a set of input files that represent a scenario to run. VBFNLO 3.0 has 168 regress tests, which correspond to the different processes implemented in VBFNLO as well as some variations on the input files, like using anomalous couplings or resonances of New Physics models.

The regress tests are run automatically on each commit during the development of the code. The output is compared to the manually validated output of a previous run. During the initial development of a new process the code is compared to an independent second calculation or (if available) existing calculations in the literature. Once a section of the code is validated all new changes can be validated against older runs, thus leading to a chain of validations. To

```

Significance, relDiff,   Diff,      Differr
2.89 sigma = +0.866 % (5.42e-04 +- 1.87e-04 fb) 422_ZZhadWM
2.80 sigma = -0.095 % (-8.92e+02 +- 3.19e+02 fb) 1640_WMJ
2.71 sigma = +0.341 % (4.77e-04 +- 1.76e-04 fb) 230_WmZjj
2.40 sigma = +0.908 % (3.81e+03 +- 1.59e+03 fb) 3130_QCDWPjj
2.27 sigma = -2.593 % (-1.68e-01 +- 7.41e-02 fb) 3230_QCDWMZjj
[...]
0.02 sigma = -0.004 % (-7.45e-06 +- 4.12e-04 fb) 430_WpWW_RS
0.02 sigma = +0.005 % (9.25e-05 +- 5.54e-03 fb) 4330_GFZZ
0.01 sigma = -0.002 % (-6.54e-08 +- 6.09e-06 fb) 2102_HAjj_mu
0.01 sigma = -0.007 % (-1.63e-05 +- 1.74e-03 fb) 111_Hjjj_AA
0.01 sigma = -0.003 % (-8.45e-05 +- 1.37e-02 fb) 222_WPZhadjj

```

Listing 5.1: For validation all existing example input files are run and compared to previous output. This shows the difference ordered by the significance (relative difference/statistical uncertainty) together with the relative difference, the absolute difference and the Monte Carlo error propagated to the difference. The most and least significant deviations are shown as an example for the comparison of the previous VBFNLO version to the modified random numbers/VEGAS in VBFNLO 3.0.

save time, the tests are usually run only with a small number of points (2^{10}) for the Monte Carlo integration. In this low statistics case, the output is checked to be numerically identical to the saved result. The Monte Carlo error for this low number of points is typically of the same magnitude as the result and therefore not trustworthy.

For the majority of changes, like adding new processes, modifications to result output or additional settings, the numerical results of other processes should not change at all, such that checking a few phase space points is sufficient. On the other hand, sometimes the numerical result changes, due to a different generation or usage of random numbers or a modification of some part of the calculation. In that case, a high statistics run is needed, such that the agreement of the new output with the saved result can be tested within the statistical integration errors.

As part of the MPI implementation (Section 5.4.1) the quantity of generated random numbers was reduced to the minimum needed to improve performance. This changed the generated phase space points and thus the output of the numerical integration. Based on this change the validation process is demonstrated.

To check the correctness of the changed random number generator and VEGAS setup, all regress tests are run with the full integration statistics and compared against the last validated version. For each comparison the significance of the difference is calculated as

$$\sigma = \frac{|I_{\text{new}} - I_{\text{ref}}|}{\sqrt{\delta_{\text{new}}^2 + \delta_{\text{ref}}^2}}, \quad (5.14)$$

where I_{new} (I_{ref}) and δ_{new} (δ_{ref}) are the cross section and Monte Carlo error of the new (reference) run.

Listing 5.1 shows an excerpt of the numerical output for this comparison sorted by the significance. The most significant difference in this example is 2.9σ and is found for process 422, which is triple vector boson production of ZZW with one Z boson decaying hadronically. The significance of this deviation can be assessed by considering all deviations statistically.

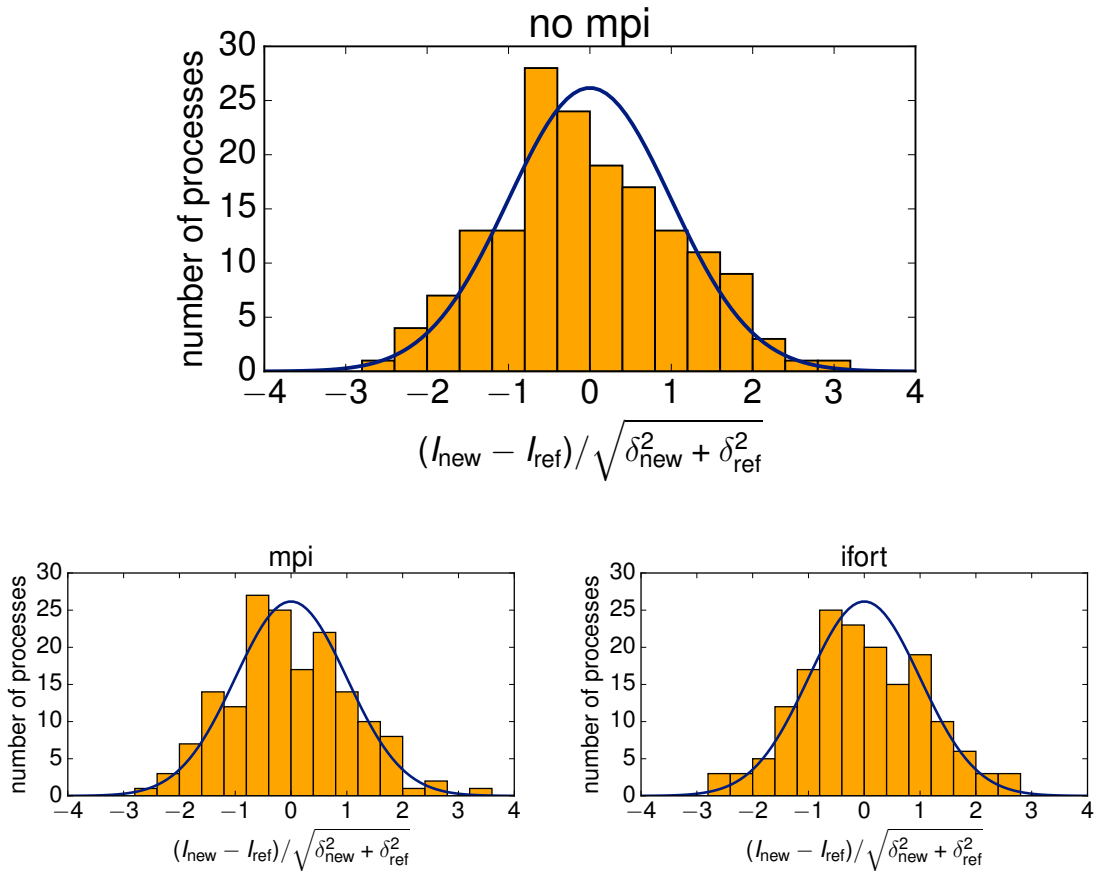


Figure 5.4: Significance of the change in total cross section when compared to reference runs. The number of runs is shown binned by the significance of the difference as stated in Eq. (5.14). The reference runs are identical for all plots and based on the VBFNLO 2.7.1 release, while the new runs use VBFNLO 3.0 beta 3 with different options. The top plot uses standard compilation and runtime. The one on the bottom left is compiled with MPI support and uses parallel runs and the one on the bottom right is compiled with ifort, leading to different numerical optimizations and output. For comparison the expected distribution (Gaussian of width 1) is overlaid.

Figure 5.4 shows a histogram of all comparisons binned by the significance of the difference between new and reference runs. Three different setups for the compilation are shown:

- without MPI and runs on a single core,
- with MPI and parallel runs,
- using Intel Fortran Compiler, which uses different numerical optimizations.

For all three configurations, the differences follow a Gaussian distribution. Investigating the distribution allows to check for several potential problems. If a single process was broken, this would be visible as an outlier. The maximal observed deviation for all configurations is close to 3σ . With a sample size of 164 processes, approximately one process with a difference of 3σ is expected in each comparison.

There is no overall bias to smaller or larger cross section values. This could happen if the phase space is not appropriately filled. Problems due to numerical instabilities or integration step would increase the reported error and increase the difference to the reference runs.

5.6. Interface to Loopsim

Section 2.4 introduced the LoopSim method. This section will discuss the technical steps to interface VBFNLO to the LoopSim program. This discussion is based on previous work that interfaced and studied VBFNLO in combination with Loopsim in WZ [173], WW [174] and ZZ production [175]. While most of the discussion is generic, for process specific sections the example process will be $WZ@n\bar{n}$ NLO. This is constructed by combining the VBFNLO implementation for $WZ@NLO$ [214] and $WZj@NLO$ [215, 216]. The LoopSim code is used in version 1.0.0 as published at [54].

VBFNLO provides event output for LO calculations in the HepMC [217] and LHE [218] formats. These formats are standardized to improve compatibility between Monte Carlo programs of different authors, detector simulation and analysis tools.

To interface with LoopSim the LHE output is extended to NLO calculations. At NLO there are multiple connected events in the real emission. For a given real emission phase space point multiple subtraction terms are generated. To get meaningful results on the variance and thus integration error of observables, one has to ensure that the real emission and subtraction events are always processed together and numerical cancellations can occur before the weight is used to calculate the variance. LoopSim uses an additional header, that enumerates the subtraction terms. Excerpts of example events can be found in Appendix A. The LHE event format also asks for color structures of events. VBFNLO does not calculate the color structures separately and since LoopSim does not use this information, the corresponding fields can be neglected. The same holds of the particle id of partons. For final states, VBFNLO sums over the possible flavors and LoopSim does not use the flavor information, such that a dummy flavor can be used.

To generate the input events for LoopSim a very inclusive selection in the generation cuts is needed to fill the IR divergent phase space. This reduces the relative statistics of the high- p_T tail, such that a balance between very inclusive and computationally feasible needs to be found. This issue can be improved by reweighting as discussed in Section 5.2.1 The overall increase in statistics as well as the more complex analysis increase the runtime of VBFNLO interfaced to LoopSim compared to stand-alone VBFNLO by about a factor of 8.

Overall the majority of the cross section typically comes from the $X@NLO$ sample, while in tails the $X + j@NLO$ becomes relevant. This becomes visible in Fig. 5.5, where the contributions of the individual samples to the p_{TZ} distribution of $WZ@n\bar{n}$ NLO using inclusive cuts are shown. The real emission of the $WZj@NLO$ sample dominates the integration error in the tail. This is visible as statistical fluctuations in Fig. 5.5. The virtual corrections of WZj are negative in the tail and overall have little contribution to the cross section. For observables sensitive to additional radiation, the WZj events can become dominant.

Already at generation level, the renormalization scale has to be chosen in a way that both, the unmodified $X@NLO$ and the *looped* $X + j@NLO$ sample, use the same scale. This can be done by either using a fixed scale or the identical IR-safe dynamical scale in both samples. This ensures that observables that get contributions from both samples are calculated consistently.

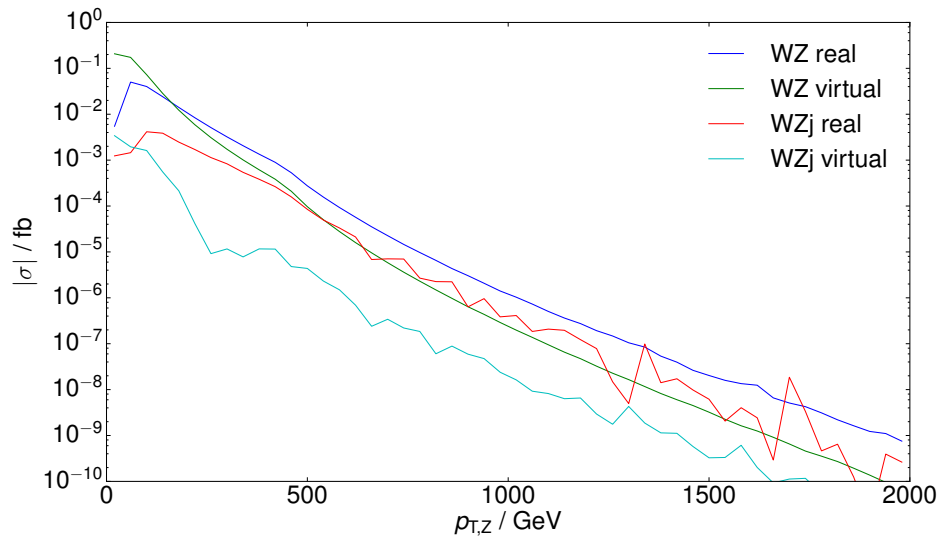


Figure 5.5: Contribution of the four individually integrated contributions to the $WZ@NLO$ cross section. Virtual corrections and real emission of $WZ@NLO$ are used directly, while for $WZj@NLO$ the LoopSim algorithm is applied first. The $WZ@NLO$ contributions are dominant close to the production threshold. In the high- p_T region, the $WZj@NLO$ sample gains influence. The fluctuations are due to the limited statistics in the tails.

Phenomenological Analysis

In this chapter the implementation discussed in Chapter 5 will be used to analyse jets in diboson production and improve the study of triple gauge couplings. The setup of the numerical calculation is introduced in Section 6.1 and the role of jets in WZ and WH production is discussed in Section 6.2 with a focus on the anomalous couplings search region. This discussion is published in [219]. Based on this, in Section 6.3 observables are discussed that allow to describe diboson events with additional jets and find topologies that are sensitive to anomalous couplings. These observables are used to construct a dynamical jet veto in Section 6.4 that improves anomalous coupling searches. Finally, corrections at \bar{n} NLO QCD for WZ production using the LoopSim method are calculated in Section 6.5. The effect of these corrections on anomalous couplings, the observables introduced in Section 6.3 and the application of the dynamical jet veto on the merged sample are investigated. This analysis is published in [92].

6.1. Calculational Setup

For the following analysis VBFNLO [27–29] is used in the published version 3.0.0beta4 [176]. The WH/WHj implementation and associated tests are documented in [220]. WZ production was implemented in VBFNLO at NLO QCD in [214] and WZj production in [215]. AC in $WZ(j)$ production were implemented and studied in [221].

We neglect effects from non-diagonal CKM entries. In [220] they were shown to be less than 1% in WH production and thus negligible compared to the scale dependence which in the same configuration is 7-14%, depending on the process. The 5-flavour scheme is used, which means that b quarks are included and considered massless in all parts of the calculation. The strong coupling α_s is treated using \overline{MS} renormalization. Its value and running are taken from the corresponding PDF set.

The following values for physical constants are used if not explicitly stated otherwise. Where applicable, they follow the defaults in VBFNLO and are based on recent global fits.

$$\begin{aligned}
 G_F &= 1.16637 \cdot 10^{-5} \text{ GeV}^{-2}, & m_{\text{top}} &= 172.4 \text{ GeV}, & \sin \theta_W &= 0.222646, \\
 m_W &= 80.3980 \text{ GeV}, & \Gamma_W &= 2.098 \text{ GeV}, & \text{BR}(W \rightarrow l\nu) &= 10.84\%, \\
 m_Z &= 91.1876 \text{ GeV}, & \Gamma_Z &= 2.508 \text{ GeV}. & \text{BR}(Z \rightarrow \bar{l}l) &= 3.35\%, \\
 m_h &= 126 \text{ GeV}, & \Gamma_h &= 4.277 \text{ MeV}.
 \end{aligned} \tag{6.1}$$

For the electroweak parameters, G_F, m_W, m_Z are used as inputs and $\sin \theta_W, e$ and α determined using the LO relations of the SM. This ensures a consistent treatment throughout the calculation, which is LO in the electroweak coupling. The decay width of the weak bosons

are based on LO relations and thereby match the included LO decay amplitudes, while for the Higgs decay width known higher order results are included. For a detailed discussion on possible combinations of electroweak input parameters and their treatment see the VBFNLO manual [28].

If not stated otherwise, for all LO calculations the PDF set CTEQ6L1 and for NLO calculations CT10 is used [37, 38]. Jets are clustered using the anti- k_t algorithm [222] with a radius of $R = 0.4$. The analysis in Section 6.3 uses a center of mass energy of 14 TeV, while Section 6.5 uses 13 TeV as used in run 2 of the LHC.

For WZ and WH production in the following sections inclusive cuts refer to the following list of selections. They are chosen to represent a simplified version of the experimental analyses of diboson production.

$$\begin{aligned} p_{Tl} > 20 \text{ GeV}, \quad p_{Tj} > 30 \text{ GeV}, \quad \cancel{p}_T > 30 \text{ GeV}, \\ |\eta_j| < 4.5, \quad |\eta_l| < 2.5, \quad R_{l(l,j)} > 0.4, \\ m_{ll} > 15 \text{ GeV}, \quad R_{ll} > 0.4. \end{aligned} \quad (6.2)$$

The m_{ll} cut refers to same-flavor-opposite-sign leptons that come from the Z boson decay. For both the W and Z boson, leptonic decays are assumed to different flavors: $W \rightarrow e\nu_e, Z \rightarrow \mu\mu$. Other flavor combinations add a combinatorial factor 4 to the cross section. Same-flavor decays increase the complexity of the reconstruction to find the correct lepton pair for the Z boson.

For *boosted* cuts the additional condition is

$$p_{TZ/H} > 200 \text{ GeV}. \quad (6.3)$$

For anomalous couplings a form factor as introduced in Eq. (3.29) is used with $n = 1$ and $\Lambda_{\text{FF}} = 2 \text{ TeV}$. The suppression due to the form factor is small in the kinematical ranges studied here, i.e. less than 10% for $m_{VV} \leq 500 \text{ TeV}$. The plots shown are in general comparable to such without form factor.

6.2. Jets in Diboson Production

We study diboson production to learn more about the interactions between electroweak bosons. Additional jet radiation can reduce the sensitivity to AC, as was shown in e.g. [221, 223]. Therefore, it is important to understand the properties of additional radiation and how to correctly treat it to restore maximal AC sensitivity. To do this WHj production and WZj production are considered at NLO QCD.

WH and WZ production share several diagram topologies. A selection of contributing diagrams is shown in Fig. 6.1. At LO in WH production the Higgs has to be attached to the W boson. These diagrams also exist in WZ production, with a WWZ triple gauge coupling. WZ production can, in addition, have both bosons attached to the quark line. These diagrams not only complicate the calculation (one additional propagator for loop diagrams) but also significantly contribute to the cross section. WH production has additional contributions at NLO, where the Higgs couples to a gluon via a quark loop. This type was shown in [220] to contribute to WH production with less than 3%. For WZ production the same topology exists, but has an even smaller relative contribution.

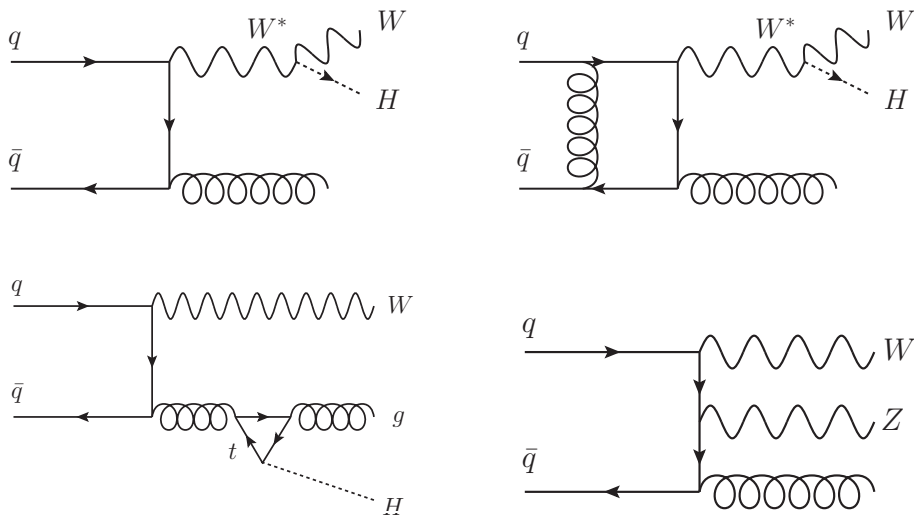


Figure 6.1: Example Feynman diagrams for WHj and WZj production. The top two diagrams exist identically for WZj production and contain a triple gauge coupling vertex. On the bottom left a coupling of the Higgs to a gluon via an effective top loop is shown. On the right the Z boson is coupled to the quark line.

To increase the sensitivity to anomalous couplings and reduce backgrounds, typical analyses focus on the *boosted* phase space region, where one of the vector bosons has large transverse momentum. Without loss of generality we will consider only a boosted Higgs in WH production and a boosted Z boson in WZ production. We will focus on the W^+ channel. Similar results follow if the other boson is boosted or a W^- is studied.

Events with a high- p_T vector boson have a large probability of additional jet radiation. Cross sections for WZ and WZj production at LO and NLO are shown in Table 6.1 with the cuts given in Eq. (6.2). For the boosted region and additional cut $p_{T,Z/H} > 200$ GeV is applied. As renormalization and factorization scale $H_{T,\text{parton}}$ as defined in Eq. (6.21) is used. For each configuration and order, the jet multiplicity is investigated, where a jet is required to have a p_T larger than 30 GeV and is clustered with a radius of $R = 0.4$.

WZ production has no jets at leading order and can have up to one resolved jet at NLO. At NLO, WZj production has either one or two resolved jets. The NLO cross sections in Table 6.1 are split by the number of resolved jets. The contribution to $WZ@NLO$ with one resolved jet is equivalent to WZj production at LO. The corresponding number is given twice, depending on whether VBFNLO was run in NLO mode for WZ or LO mode for WZj . Different implementations of the amplitude and different phase space setups are used, such that numerical differences appear. These differences are larger than the reported Monte Carlo integration error. This could be due to the combination of several runs which leads to an underestimation of the final error.

For inclusive cuts the cross section decreases when additional jets are required since the power of α_s increases. For example at $\sqrt{s} = 8$ TeV for WZ production with $\{0, 1, 2\}$ jets the cross sections are $\{8.4, 4.8, 2.1\}$ fb. This is no longer the case for boosted cuts, where the corresponding cross sections are $\{0.21, 0.37, 0.27\}$ fb. Here additional jets are favored to balance the boosted vector boson.

$\sqrt{s} = 8 \text{ TeV}$	inclusive				boosted			
	W^+Z		W^+Zj		W^+Z		W^+Zj	
	LO	NLO	LO	NLO	LO	NLO	LO	NLO
N_{jets}								
0	8.48	10.40			0.214	0.188		
1		4.84	4.87	4.20		0.369	0.373	0.226
2				2.12				0.271

$\sqrt{s} = 14 \text{ TeV}$	inclusive				boosted			
	W^+Z		W^+Zj		W^+Z		W^+Zj	
	LO	NLO	LO	NLO	LO	NLO	LO	NLO
N_{jets}								
0	14.00	16.74			0.492	0.397		
1		11.28	11.31	8.39		1.242	1.248	0.554
2				6.22				1.094

Table 6.1: Cross sections split up by jet multiplicity for WZ and WZj production at a center of mass energy of 8 TeV and 14 TeV. The cross sections are given in fb and have integration errors smaller than $3 \cdot 10^{-3}$ fb for the total cross section. Already for inclusive, but especially for boosted cuts a large fraction of events has additional jets in the final state and higher order corrections favor additional jets. This table is also published in [219].

$\sqrt{s} = 8 \text{ TeV}$	inclusive				boosted			
	W^+H		W^+Hj		W^+H		W^+Hj	
	LO	NLO	LO	NLO	LO	NLO	LO	NLO
N_{jets}								
0	24.85	24.81			1.716	1.467		
1		8.180	8.365	7.461		0.854	0.889	0.724
2				2.351				0.318

$\sqrt{s} = 14 \text{ TeV}$	inclusive				boosted			
	W^+H		W^+Hj		W^+H		W^+Hj	
	LO	NLO	LO	NLO	LO	NLO	LO	NLO
N_{jets}								
0	47.08	44.12			4.103	3.188		
1		19.72	20.16	16.12		2.648	2.690	1.889
2				7.16				1.243

Table 6.2: Cross section for W^+H and W^+Hj production are given as in Table 6.1. As in WZ production, going to higher invariant mass or boosted cuts increases jet activity. Overall there is less jet radiation than in WZ production. This table is also published in [219].

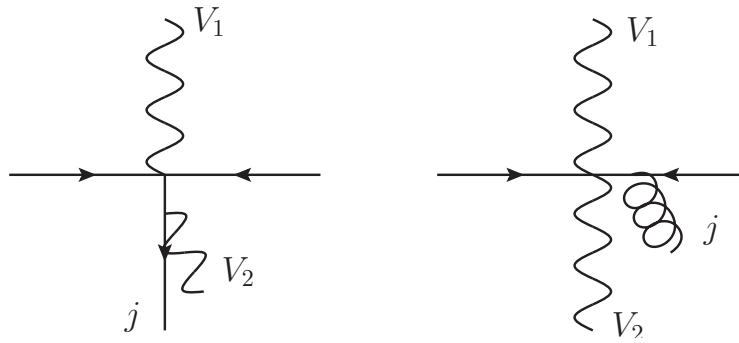


Figure 6.2: The dominant momentum configurations for diboson + jet production are shown when one boson is required to have large transverse momentum. The *boosted* boson recoils either against the other weak boson (right) or against a jet (left).

For the inclusive cuts at NLO, both for WZ and WZj production about 40% of the events have an additional resolved emission. With boosted cuts, this grows to about 70%. These numbers depend significantly on the chosen cuts. The number of resolved jets in general grows when smaller jets and smaller transverse momenta of the jets are considered. Nevertheless, for typical analysis cuts, many or even most events will come with additional resolved radiation. Therefore, higher order corrections with additional emissions have to be included to give a good description of these processes.

Table 6.2 shows cross section values for the same cuts applied to WH production. The qualitative behavior is the same as in WZ production, but the amount of additional jet activity is smaller than in the WZ case. Events with additional resolved emission at $\sqrt{s} = 14$ TeV increase for WH and WHj production from 30% for inclusive only to around 40% for boosted cuts. The difference between WH and WZ production can be understood by considering the involved kinematical configurations. Requiring one vector boson with high transverse momentum in diboson production can lead to two classes of momentum distribution shown in Fig. 6.2. The *boosted* vector boson recoils either against the other vector boson or against a jet.

For very large momenta, the recoil against the jet is enhanced, since the second boson can be *soft* in comparison to the scale of the event. The emission of a soft vector boson is logarithmically enhanced. For massless vector bosons (like the photon) this enhancement is an infrared singularity. The vector boson mass regularizes the divergence, but still leaves a term $\propto \log(m_V^2/p_{T,jet}^2)$. These types of emissions can be considered electroweak corrections to the Vj production processes. This enhancement appears only for diagrams where the soft vector boson is attached to a quark. Since these diagrams do not exist for WH production, the enhancement does not occur.

For anomalous coupling searches, a large invariant mass at the triple gauge vertex is needed. The enhancement of AC compared to the SM is typically proportional to \hat{s} as discussed in Section 3.3. The diboson pair has a large invariant mass when one boson has a high- p_T and recoils against the other boson. On the other hand, a soft boson leads to a small invariant mass and negligible AC effects. Therefore, the kinematical regime, where the recoil happens against a jet should be suppressed in analyses.

6.3. Distinguishing Dibosons from V+jet Production

To separate diboson production with soft jet radiation from single vector boson + jet events with an additional soft vector boson, we will introduce a parametrization of the final state kinematics. The goal is to construct an observable which can parametrize the amount of jet activity in an event and has separation power for phase space regions sensitive to anomalous couplings. This analysis was published in [219].

6.3.1. Kinematical Variables

A final state is defined by the particles and their momenta. Kinematical properties are described using observables that are a function of these momenta. Different constructions of these functions are possible. There are different conditions on the definition of observables depending on their use.

From experiments:

- Measurable: using only measurable quantities of detectable particles
- Small systematics: use well-understood quantities as input
- Theory-independent: little dependence on details of theoretical/simulation input
- Stable: little or well-known dependence on cuts and analysis input

From theory:

- Well-defined: use only objects present in the theoretical calculation
- IR safe: Independent of IR details, stable under NLO and PS calculation
- Easy to calculate: Reduce complexity to reduce runtime and errors
- Parton level: Allow reasonable description already at parton level

Some constructions show a tension between those requirements. For example a jet definition in an experimental analysis will mostly be based on hadronic energy depositions in a calorimeter, while a parton-level Monte Carlo program will use individual partons to define it. Therefore, for predictions it is important to be aware which calculations are applicable for which analysis. In the case of jets, modern jet algorithms can be based on either calorimeter towers or partons.

A comprehensive review of kinematical variables can be found in [30]. For a single particle, the starting point for any description is the four-momentum p^μ .

The momentum can be written as

$$\vec{p} = \begin{pmatrix} p_x \\ p_y \\ p_z \end{pmatrix} = \begin{pmatrix} p_T \cos \phi \\ p_T \sin \phi \\ p_T \sinh \eta \end{pmatrix}, \quad |\vec{p}| = p_T \cosh \eta. \quad (6.4)$$

Useful objects to describe a particle four-momentum p are

$$\text{transverse momentum, } p_{\text{T}} = \sqrt{p_x^2 + p_y^2}, \quad (6.5)$$

$$\text{azimuthal angle, } \phi = \arccos \frac{p_x}{p_{\text{T}}}, \quad (6.6)$$

$$\text{polar angle, } \theta = \arccos \frac{p_z}{\sqrt{p_x^2 + p_y^2 + p_z^2}}, \quad (6.7)$$

$$\text{rapidity, } y = \frac{1}{2} \ln \left(\frac{E + p_z}{E - p_z} \right) = \operatorname{arctanh} \left(\frac{p_z}{E} \right), \quad (6.8)$$

$$\text{pseudorapidity, } \eta = -\ln \tan \frac{\theta}{2}, \quad (6.9)$$

$$\text{invariant mass, } m^2 = p^2. \quad (6.10)$$

Rapidity and pseudorapidity are identical for massless particles or in the limit of small mass compared to p_{T} . For non-vanishing mass there are differences as

$$y = \eta - \frac{1}{2} \cos \theta \left(\frac{m}{p_{\text{T}}} \right)^2 + \mathcal{O}(m^4). \quad (6.11)$$

Pseudorapidity does not depend on the mass, and directly translates to an angle relative to the beam axis. Rapidity, on the other hand, has the property, that a longitudinal boost with velocity β leads to a constant shift

$$y' = y - \tanh^{-1} \beta. \quad (6.12)$$

Therefore the shape of the rapidity distribution stays invariant. Two objects with rapidity difference $\Delta y = y_1 - y_2$ in the lab frame will have the same Δy in any longitudinal boosted frame, like the center of mass frame of the hard partonic interaction.

At the LHC the center of mass frame of the proton collisions is identical to the laboratory frame of the detector. However, the relevant frame is the center of mass of the colliding partons and since the two partons in general carry different momentum fractions, this frame will be longitudinally boosted. If a neutrino is part of the final state or not all particles are within the detector acceptance, not all momenta can be measured and therefore the center of mass frame of the parton collision can not be reconstructed. Therefore properties depending on the correct longitudinal boost are usually not applicable for analysis and boost-invariant observables like Δy used instead.

Inherently boost invariant are observables which only depend on the transverse momentum. Besides transverse momentum, commonly used observables are

$$\text{transverse mass, } m_{\text{T}} = \sqrt{m^2 + p_{\text{T}}^2} = \sqrt{E^2 - p_z^2} = \sqrt{(E - p_z) \cdot (E + p_z)}, \quad (6.13)$$

$$\text{transverse energy, } E_{\text{T}} = \frac{E}{\sqrt{1 + \frac{p_z^2}{p_{\text{T}}^2}}} = E \cdot \frac{|p_{\text{T}}|}{|\vec{p}|}. \quad (6.14)$$

The transverse energy in this definition is not invariant under longitudinal boosts. The definitions for transverse mass m_{T} and transverse energy E_{T} are identical in the limit of small masses as well as for large transverse momenta. Within this limit they are both identical to

their massless version and equal p_T . For massive particles transverse mass and energy differ. Especially for a fixed rapidity and mass

$$\lim_{p_T \rightarrow 0} m_T = m, \quad (6.15)$$

$$\lim_{p_T \rightarrow 0} E_T = 0. \quad (6.16)$$

In the literature the distinction between transverse mass and transverse energy is sometimes not strict and might not follow the definitions given here. The definitions here are for example implemented in FastJet [55, 224] and programs based on it.

For pairs of particles, interesting values are

$$\text{invariant mass, } m = \sqrt{(p_1 + p_2)^2}, \quad (6.17)$$

$$\text{R separation, } R = \sqrt{\Delta\phi^2 + \Delta y^2}. \quad (6.18)$$

All single-particle definitions can also be computed for multi-particle systems by using the four-momentum sum of the individual momenta. For reconstructed particles, the reconstructed four-momentum is used to define those quantities. For example for the leptonic decay of a Z boson, the four-momentum of the Z boson can be calculated from the momenta of the decay leptons p_l and $p_{\bar{l}}$ as $p_Z = p_l + p_{\bar{l}}$. Other observables are then based on the reconstructed momentum p_Z , like

$$E_{T,Z} = E_T(p_Z) = E_T(p_l + p_{\bar{l}}). \quad (6.19)$$

An exception to this convention is the shorthand

$$E_{T,\text{jets}} = \sum_{\text{jets}} E_{T,i} \quad (6.20)$$

which for events with a variable number of jets refers to the scalar sum of the transverse energies of all resolved jets.

A common problem is to find an energy scale corresponding to a complete event or a subset of particles. Such a scale can be used as a dynamical renormalization scale or to categorize events in types. The basic idea to obtain this scale is to sum up all individual particle scales or the relevant subsets. This involves several choices. For electroweak particles one can either use the final decay particles or the reconstructed bosons. Jets can be either included as reconstructed jets or at the parton level. For each individual particle there are multiple choices for a scale, for example its energy, transverse momentum, transverse mass or transverse energy as introduced in Eqs. (6.13) and (6.14). Potential constructions include:

$$H_{T,\text{parton}} = \frac{1}{2} \left(\sum_{\text{partons}} p_{T,i} + \sum_{W,Z} \sqrt{p_{T,i}^2 + m_i^2} \right), \quad (6.21)$$

$$H_{T,\text{squared}} = \frac{1}{2} \sqrt{\sum_{\text{partons}} p_{T,i}^2 + \sum_{W,Z} (p_{T,i}^2 + m_i^2)}, \quad (6.22)$$

$$E_T = E_{T,\text{jets}} + E_{T,W} + E_{T,Z}. \quad (6.23)$$

6.3.2. Lepton Separation Cut R_{ll}

Sometimes a lepton separation cut is introduced to suppress background. This means that the distance between each lepton pair, as defined in Eq. (6.18), needs to be bigger than R_{ll} , which is typically on the order of 0.4.

This type of cut is unsuitable for analyses that investigate high- p_T bosons. For a boosted particle with invariant mass m_Z that decays to two massless (or relativistic) particles, by using Eq. (6.4) one finds

$$\begin{aligned}
m^2 &= 2p_1 \cdot p_2 = 2(E_1 E_2 - \vec{p}_1 \cdot \vec{p}_2) \\
&= 2(p_{T1} p_{T2} \cosh \eta_1 \cosh \eta_2 - \\
&\quad p_{T1} p_{T2} (\cos \phi_1 \cos \phi_2 + \sin \phi_1 \sin \phi_2 + \sinh \eta_1 \sinh \eta_2)) \\
&= 2p_{T1} p_{T2} (\cosh(\eta_1 - \eta_2) - \cos(\phi_1 - \phi_2)) \\
&\approx 2p_{T1} p_{T2} \left(1 + \frac{1}{2} \Delta\eta^2 - 1 + \frac{1}{2} \Delta\phi^2\right) \\
&= p_{T1} p_{T2} \Delta R^2 \\
&\approx \frac{1}{4} p_{TZ}^2 \Delta R^2,
\end{aligned} \tag{6.24}$$

where p_Z is the momentum of the decaying particle in the lab frame and p_{TZ} its transverse momentum. p_1, p_2 are the momenta of the decay products and $\Delta\eta, \Delta\phi, \Delta R$ the separation of the decay products.

In the first approximation step, the separation of the two particles is assumed to be small, such that \cos and \cosh can be expanded. This approximation is valid if the decaying particle is boosted, such that the decay momenta in the particles rest frame will also be boosted and their separation is reduced in the lab frame. This approximation depends on the decay angle. Decays perpendicular to p_{TZ} will be boosted closely together, while decays aligned with the Z boson momentum that end up in opposite hemisphere will still be widely separated. In this limit the decay particles will each carry approximately half of the transverse momentum of the decaying particle, $p_{T1} \approx p_{T2} \approx \frac{1}{2} p_{TZ}$, which is used in the last step.

Since the vector bosons are mostly produced on-shell, a cut in R_{ll} corresponds to a cut in p_T with a dependence on the decay angle. This angular dependence is also correlated to the helicity of the Z boson. In combination with AC contributions, which depend on the vector boson helicities, the R_{ll} cut might lead to non-trivial effects.

For the Z boson mass and a cut $R_{ll} > 0.4$, Eq. (6.24) corresponds to $p_T < 450$ GeV. For transverse momenta above 450 GeV the cross section is reduced, since only certain angular configurations of the decay will pass the cuts.

For many modern analyses this problem does not appear. There R_{ll} is not used, but isolated muons and electrons are identified not only based on distance, but also on the energy of the particles. This allows to identify leptons with a high invariant mass even when they are boosted and have a small distance in R .

6.3.3. Defining x_{jet}

Using the knowledge about kinematical variables and their features, we can describe additional jet radiation in WZ production. The starting point to define x_{jet} is the three particle final state WZj . The analysis is later extended to decaying particles and multiple jets.

This three particle final state can be described by using the particles' 4-momenta. We assume all particles to be close to their on-shell mass.

Considering only the momenta in the transverse plane, there are 6 degrees of freedom for three particles: $\vec{p}_{TW}, \vec{p}_{TZ}$ and \vec{p}_{Tj} . We can reduce these 6 parameters to only 2 relevant ones to describe the event shape: Momentum conservation requires that the vector sum of these three transverse momenta vanishes, removing 2 parameters. One parameter describes azimuthal rotations of the complete systems, which is a symmetry of the collision and thus does not affect the physical description. Another parameter can be extracted which rescales all involved momenta. This parameter corresponds to the scale \hat{s} of the event and does not affect the shape.

There are several choices for the remaining two parameters. These could be angles or mass ratios. For this thesis a new set of observables was constructed:

$$x_{\text{jet}} = \frac{E_{T,\text{jets}}}{E_{T,\text{jets}} + E_{T,W} + E_{T,Z}} , \quad (6.25)$$

$$x_W = \frac{E_{T,W}}{E_{T,\text{jets}} + E_{T,W} + E_{T,Z}} , \quad (6.26)$$

$$x_Z = \frac{E_{T,Z}}{E_{T,\text{jets}} + E_{T,W} + E_{T,Z}} . \quad (6.27)$$

By construction they obey

$$x_{\text{jet}} + x_W + x_Z = 1, \quad (6.28)$$

$$0 \leq x_i < 0.5. \quad (6.29)$$

The last condition only holds for high p_T and for events with only one jet. Then x_i is maximal if the i particle recoils against both of the other particles, such that $p_{Ti} = p_{Tj} + p_{Tk}$ and for high transverse momenta $E_{Ti} \approx E_{Tj} + E_{Tk}$, which leads to $x_i = 0.5$. In phase space regions where the masses contribute significantly, this limit might not hold. Also for events with more than one jet, like real emission contributions at NLO, x_{jet} can exceed 0.5 as shown in the next section. The sum rule of Eq. (6.28) allows to choose any two of these three observables interchangeably. In this thesis we use the x_{jet}, x_Z combination for 2D analyses. The results can be directly translated to any other pair of the x_i .

Besides the definition using E_T , one can construct similar definitions using other measures for the energy scale of the particles, like p_T or m_T . These choices are discussed in Section 6.3.4. In Section 6.3 x_{jet} is used based on m_T and in Section 6.5 using E_T .

With leptonic decays of the vector bosons, the original boson four-momentum is used for the x_{jet} definition. For application in experiments due to the neutrino in the final state, some reconstruction step is needed using $E_{T,\text{miss}}$. This is directly applicable for the p_T based definition of x_{jet} , but not for E_T or m_T . An alternative would be to use the final state objects (jets and leptons) directly to define a ratio that favors ‘‘leptonic’’ events.

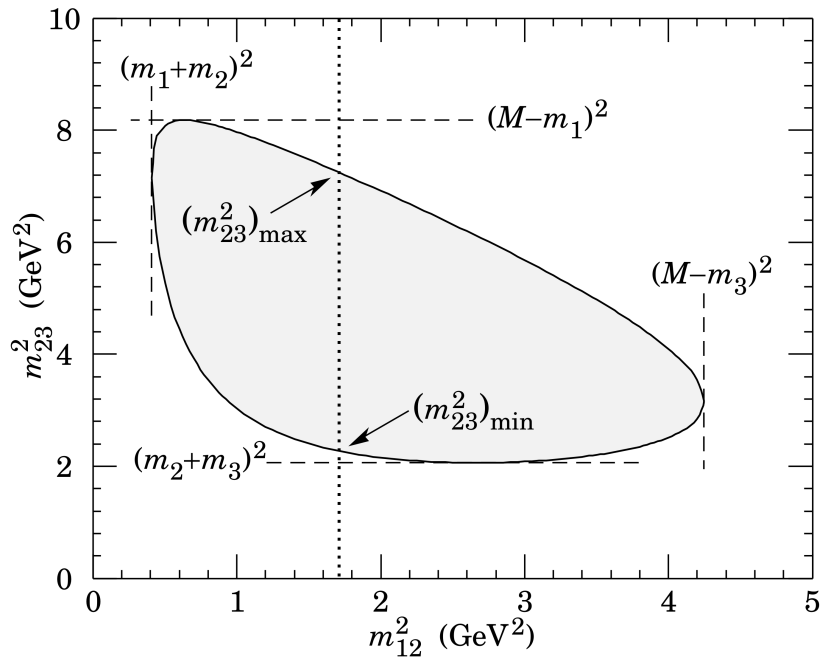


Figure 6.3: The Dalitz plot is used to describe a three-body final state. The events are shown in a 2D plot defined by the invariant mass of two pairs of final state particles. This plot is taken from [30].

6.3.4. Describing Jet Radiation in Diboson Production using x_{jet}

The goal is to describe a three-body final state. There are many physical processes with three final state particles and a famous historic example is the study of K meson decays (then called τ mesons). Dalitz [225] described the three-body decay of K mesons by considering a 2D plot of kinematical variables.

A modern version of a Dalitz plot is shown in Fig. 6.3. It uses the invariant mass of two pairs of final state particles: m_{12} and m_{23} . The sum $m_{12}^2 + m_{23}^2 + m_{13}^2$ is determined by the masses of initial and final state particles and is therefore constant. Like in the x_{jet} definition, one can choose any two of these three variables. The Dalitz plot for massless final state particles would be a triangle, while the finite masses impose kinematical limits that shrink the triangle from the edges to the grayed area shown in Fig. 6.3. This kind of plot visualizes intermediate resonances in the decay chain which enhance the rate in a certain invariant mass region. The Dalitz plot is based on the fixed mass of the decaying particle. In the diboson+jet process the total invariant mass is not fixed, such that ratios are more suitable to describe the kinematical configurations than absolute mass scales. The x_{jet}, x_W, x_Z set of variables together with the sum relation in Eq. (6.28) allows to produce Dalitz-like 2D distribution for diboson production with an additional jet.

The double differential distribution of WZj and WHj production in x_{jet} and x_Z (x_H) is shown in Fig. 6.4 at LO. The m_T based definition for x_{jet} is used together with the cuts given in Eq. (6.33) and a center-of-mass energy of 14 TeV. The overall shape is a triangle based on the sum rules given in Eq. (6.28). In the $x_{\text{jet}}-x_Z$ plane there is an upper limit on both axes of 0.5 and the lower bound stems from $0.5 \geq x_W = 1 - x_{\text{jet}} - x_Z \Rightarrow x_Z \geq 0.5 - x_{\text{jet}}$. These bounds are similar to those of the Dalitz plot, where a three-body phase space is visualized in a 2D plane and kinematical constraints lead to limits to the allowed region in this plane.

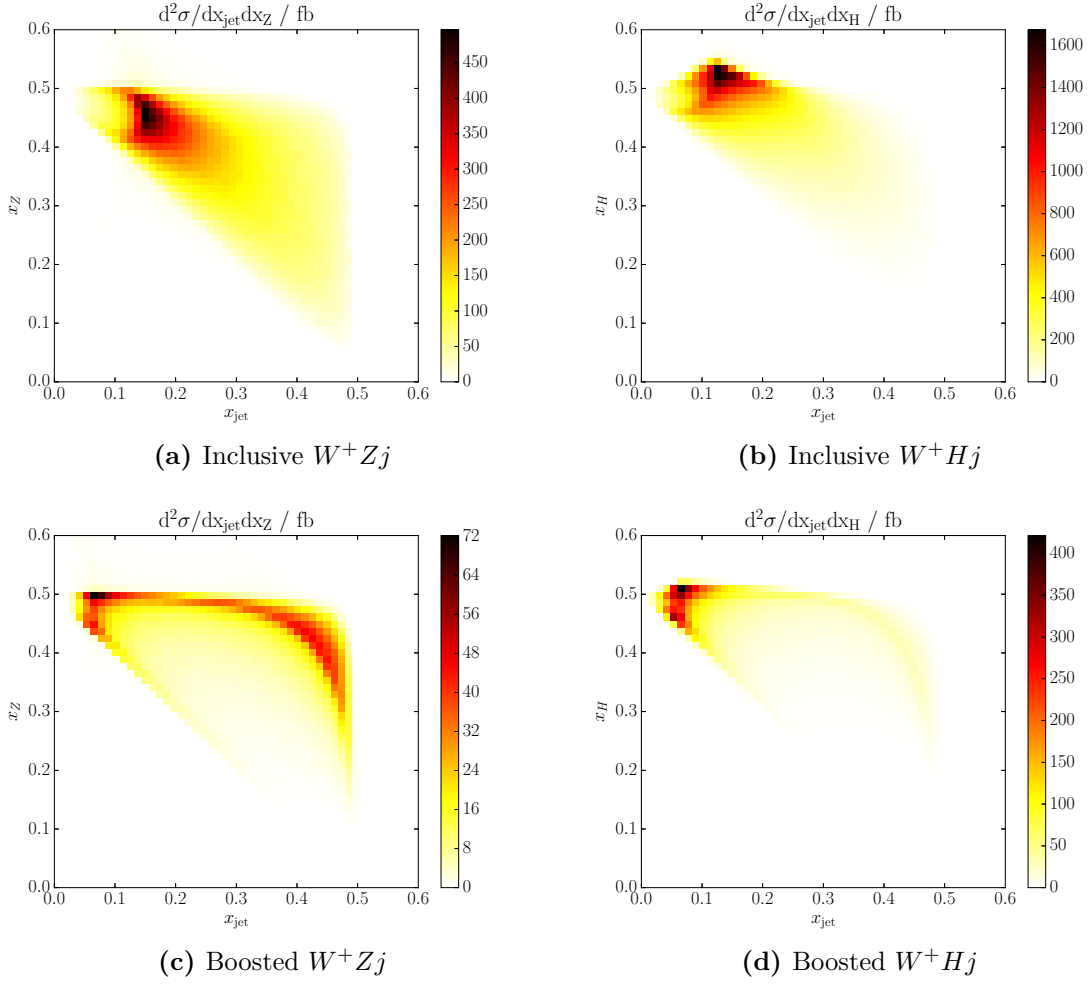


Figure 6.4: W^+Zj (left) and W^+Hj (right) production at LO are shown as double differential in x_{jet} and x_Z or x_H . The upper plots use inclusive cuts, while the lower row additionally requires the Z boson (Higgs boson) to have $p_T > 200$ GeV. These plots are also published in [219].

With inclusive cuts there is only one significant region at low x_{jet} . This is because in the inclusive case the transverse momentum is smaller than the mass. The mass contribution to m_T then leads to heavy objects (W, Z, H) dominating over the light object (jet). Also the upper limit of 0.5 is overshoot for WH production. The limit of x_H is given by $m_h/(m_h+m_W) \approx 0.6$ if the transverse momenta are small. Already with inclusive cuts WZj production has larger contributions for large x_{jet} values than WHj production, due to the preference for additional jet radiation.

For a boosted Z boson (or Higgs boson), the p_T contribution to m_T becomes dominant. This is shown in the bottom row of Fig. 6.4, where the triangle shape is more visible. For WZj production there are two sizable contributions to the cross section. One is again for small x_{jet} values and large x_Z , but another appears at large x_{jet} and large x_Z . Since the boosted cut requires the Z boson to have high transverse momentum, this corresponds to the two regions where the Z boson recoils either against a jet (large x_{jet} , small x_W) or against the W boson (large x_W , small x_{jet}). For WHj production the triangle shape is also visible, but the jet recoil region is nearly completely missing. The reason for this is that in WH production the Higgs boson is always attached to the W boson. The intermediate virtual W boson restricts

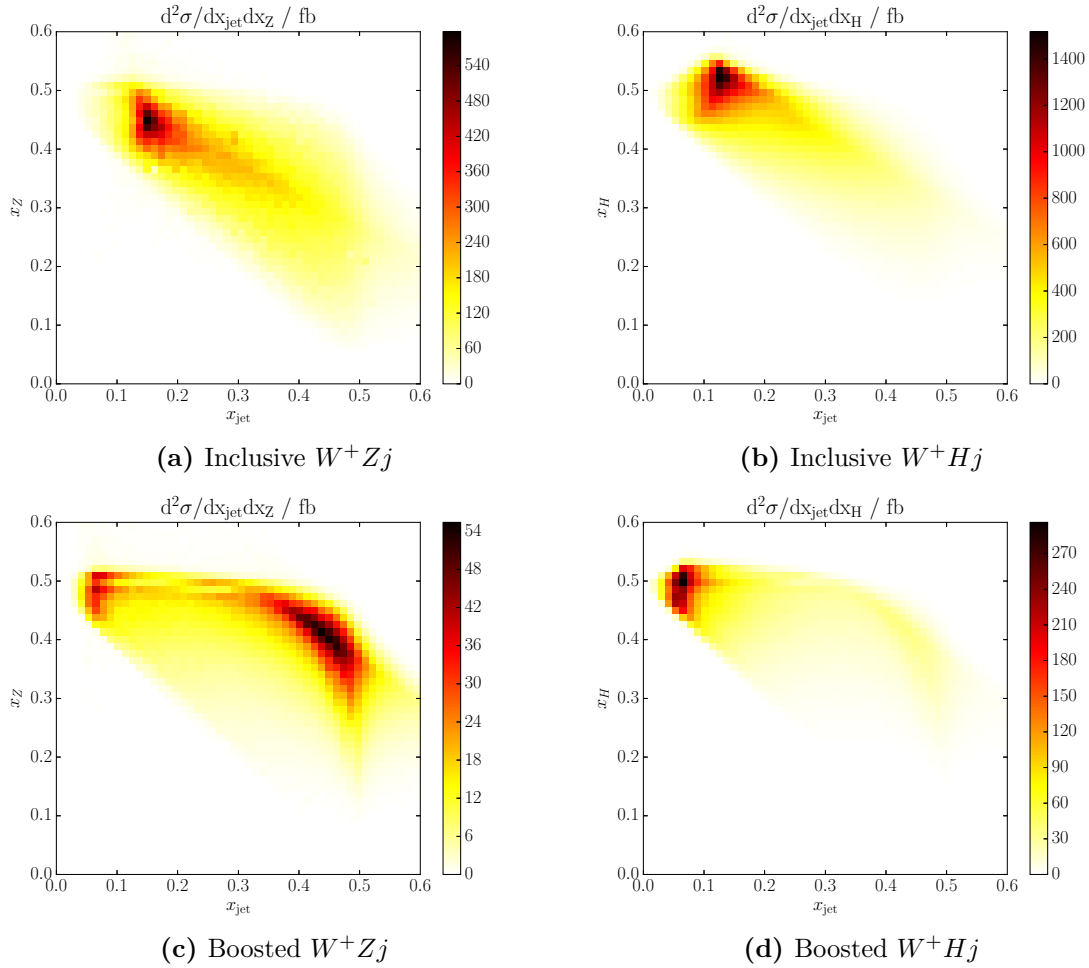


Figure 6.5: The same observables are shown as in Fig. 6.4 but including NLO QCD corrections (instead of LO). The real radiation increases the overall jet activity and leads to larger x_{jet} values. Two jets in the final state can lead to $x_{jet} > 0.5$. These plots are also published in [219].

the WH final state mostly to a $J = 1$ partial wave. Also it does not allow for enhancements due to soft radiation of one of them from a quark, like in WZ production.

The same process and cut combinations that are shown in Fig. 6.4 at LO are presented in Fig. 6.5 including NLO corrections. The overall picture is similar, but shows certain differences, due to additional radiation in the real emission, which increases x_{jet} . Furthermore, there are two jet events for which x_{jet} can be larger than 0.5. In the extreme case $x_{jet} \rightarrow 1.0$, these are dijet topologies where both vector bosons are soft emissions from two hard jets that recoil against each other. In the fixed order NLO calculation real emission and subtraction terms contribute. Using the \tilde{p} kinematics introduced in Section 2.3, subtraction terms and the real emission have slightly different momentum values. Especially at the borders of the allowed $x_{jet} - x_Z$ space, one can have a real emission event above 0.5 and the corresponding subtraction term below 0.5. These steps can be seen in the boosted case for WZj production. Histogram bins directly below $x_Z = 0.5$ have a cross section smaller than the surrounding bins.

Parton Shower Effects

Parton Showers are constructed to correctly describe low- p_T jets and emissions in the soft and collinear region. The effects of a parton shower on the x_{jet} variable family were studied by Jonas Nuber as part of his Bachelor thesis [226].

The x_{jet} , x_H distribution for WHj production at NLO QCD is shown in Fig. 6.6, where the p_T based definition is used. In the top plot the fixed order calculation is shown, for which around $x_i = 0.5$ artifacts appear which correspond to real emission and subtraction terms contributing to different bins. For one parton final states only the region $x_{\text{jet}} < 0.5$ is reachable, while for two partons also $x_{\text{jet}} > 0.5$ is accessible. At NLO the real emission can fill the full $x_{\text{jet}}-x_Z$ space, while all subtraction terms are restricted to $x_{\text{jet}} < 0.5$. Thereby real emission and subtraction terms can end up in different bins, such that the subtraction terms lead to a “dip” just below 0.5 while the corresponding excess is above 0.5.

The result of a parton shower matched to the NLO calculation (using MC@NLO) is shown in the lower plot of Fig. 6.6. The edges of the fixed order calculation are smeared out and a continuous behavior of the x_{jet} and x_H observables is found. The overall behavior of the x_i variable is unchanged, and the two kinematical regions are clearly distinguishable also after a parton shower.

Therefore, the p_T based definition can be used without appearance of artifacts at the boundaries once parton showers are used. More details and examples on the use of parton showers with the x_{jet} variable can be found in [226].

Alternative x_{jet} definitions

The x_{jet} definition in Eq. (6.25) can be modified by using either E_T , m_T or p_T . In the high- p_T region, those choices are identical, but have different behavior for low- p_T objects.

The most direct approach would be to use a p_T based definition, since the motivation for the x_{jet} construction comes from a description of the event shape in the transverse plane. As visible in Fig. 6.6, using the p_T definition leads to discontinuities around $x_Z = 0.5$ and $x_{\text{jet}} = 0.5$ for a fixed-order NLO calculation.

These discontinuities from subtraction terms have less effect when m_T or E_T are used, both of which get contributions from the mass. The drawback of m_T is that for small p_T it is dominated by the mass, such that for inclusive cuts, events end up close to the values determined by the mass and x_{jet} does not have much discriminating power between the diboson and $V + j$ type kinematical configurations.

Therefore for a fixed order analysis, E_T is the preferred definition for x_{jet} . It provides some smearing around the kinematical boundaries for large x_{jet} values and at the same time has differentiating power in the low- p_T region.

Observables that do not depend on the details of soft or collinear emissions are called *IR-safe*. x_{jet} is IR-safe, since it is constructed out of IR-safe objects (E_T , p_T or m_T). It is nevertheless sensitive to additional radiation and artifacts of the fixed order calculation become visible especially in the transition between the one jet and two jet region. Instead of using jets it is also possible to use partons in the x_{jet} definition. This makes the veto less dependent on the specific choice of jet clustering parameters, but is disfavored since it prevents a direct IR-safe extension beyond a parton-level simulation.

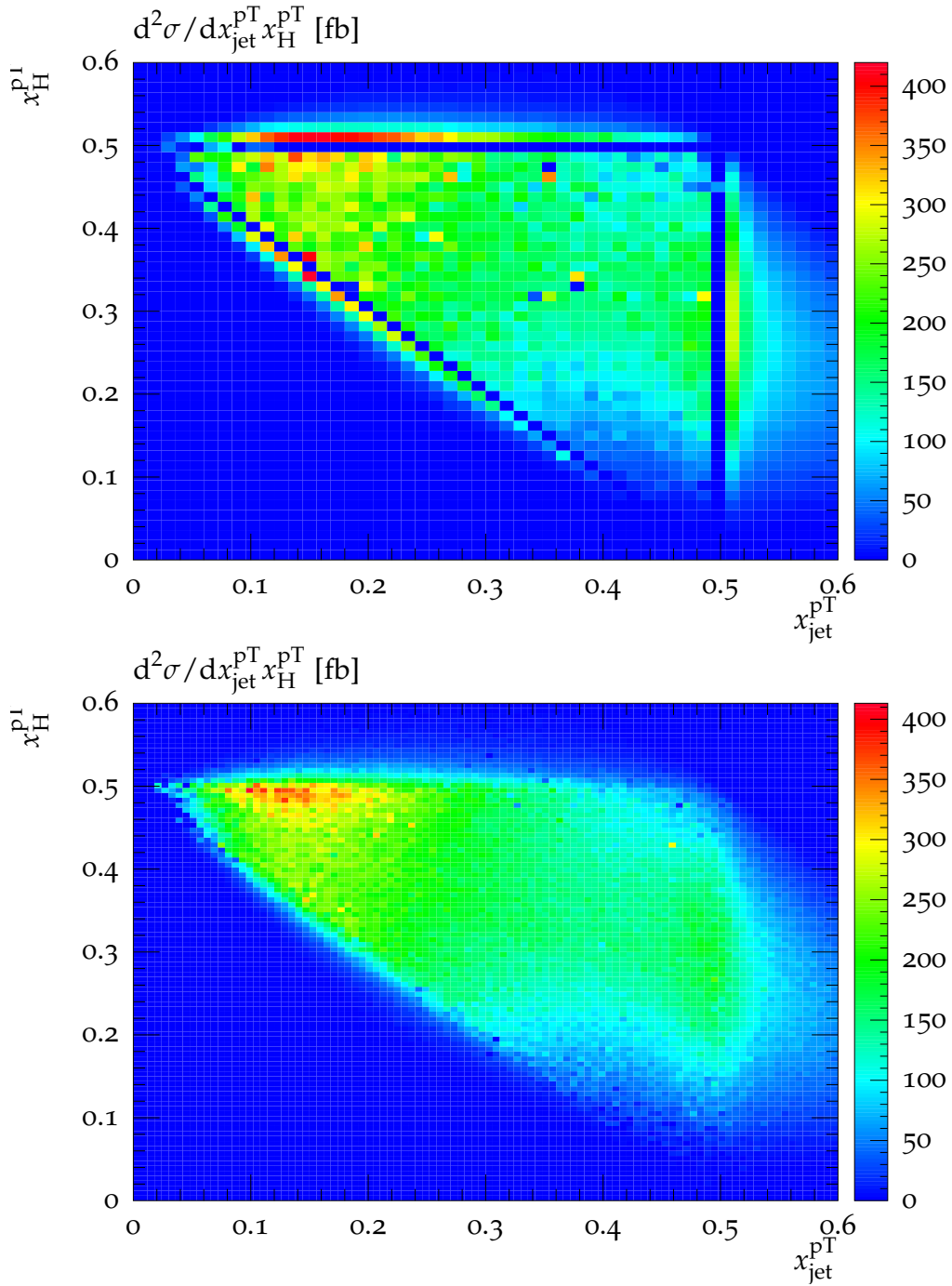


Figure 6.6: The x_{jet} , x_H distribution using p_T is shown for WHj at NLO using Herwig 7 interfaced to MadGraph5 aMC@NLO. The p_T definition of x_{jet} (top) leads to artifacts at the boundaries close to $x_i = 0.5$. Applying a parton shower (bottom) smears out those artifacts and overall leads to less numerical instabilities at these edges. These plots are taken from [226].

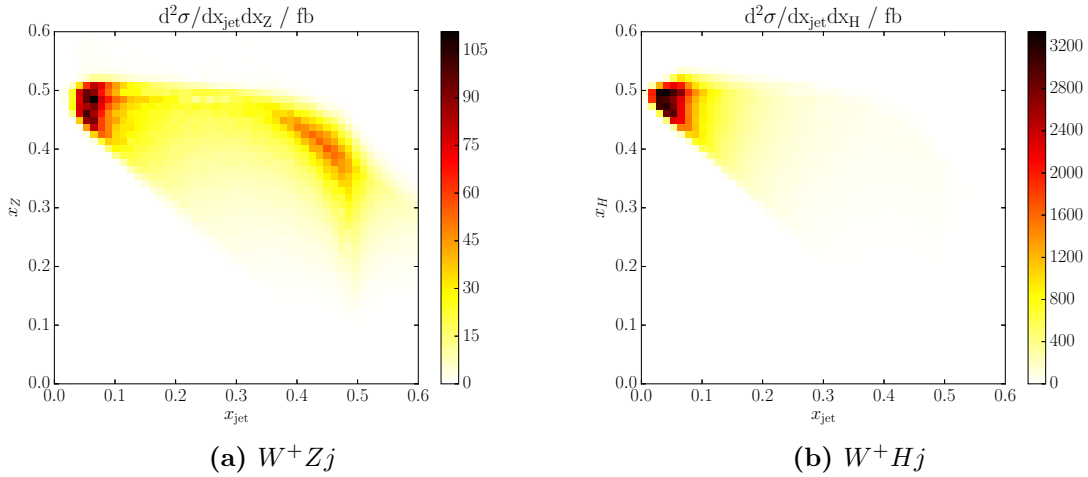


Figure 6.7: The $x_{\text{jet}}-x_Z$ (x_H) double differential distribution is shown as in Fig. 6.5, but for anomalous couplings of $f_W/\Lambda^2 = -10 \text{ TeV}^{-2}$. The boosted cuts are applied. These plots are also published in [219].

6.3.5. Applying x_{jet} to Anomalous Couplings

The goal of the x_{jet} observable introduced in Section 6.3.3 is to improve sensitivity in searches for anomalous couplings and understand the effect of additional jet radiation. To achieve this, the effect of anomalous couplings on the previously introduced distributions is investigated.

The $x_{\text{jet}}-x_Z$ distribution is shown for an anomalous coupling value of $f_W/\Lambda^2 = -10 \text{ TeV}^{-2}$ in Fig. 6.7. As in the SM case, shown in Fig. 6.5, there are still two contributing regions visible for WZj production. The overall shape is comparable to the SM case, since it is limited by kinematical constraints. The relative contribution of the two identified regions is significantly changed. Including modified triple gauge couplings, the region at large x_{jet} has a smaller relative contribution to the cross section than the region of small x_{jet} values.

Since the most significant differentiation between the kinematical configurations comes from the x_{jet} variable, the cross section distribution in this variable is shown in Fig. 6.8. The SM value shows the double peak for x_{jet} in WZj production that was already visible in the 2D plot. In addition, different coupling values for the anomalous coupling are shown. For x_{jet} around 0.5 there is nearly no change due to AC, while for small x_{jet} values a strong dependence on the AC value can be seen that reaches a factor two enhancement. For small anomalous coupling values the leading contribution is from the interference given in Eq. (3.24) and depends on the coupling sign. A positive sign leads to destructive, a negative one to constructive interference. For couplings around 10 TeV^{-2} the squared term becomes dominant, such that the destructive interference is no longer apparent. The interference effects will be more visible in p_T distributions, which will be discussed in Section 6.4.3.

For WHj the double peak in the SM is less pronounced. Nevertheless, anomalous couplings favor small x_{jet} values and the ratio $\sigma_{\text{AC}}/\sigma_{\text{SM}}$ grows towards small x_{jet} values. This confirms that x_{jet} can be used as a discriminator in searches for anomalous couplings.

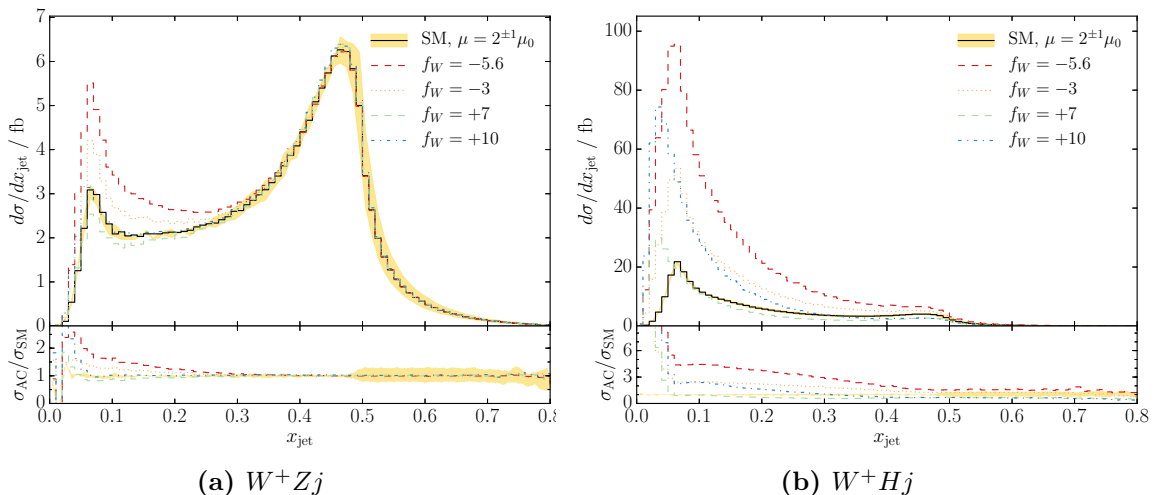


Figure 6.8: The x_{jet} dependence of the WZj and WHj production cross section is shown for the SM and different coupling values of the operator \mathcal{O}_W . For the SM prediction a band is given that corresponds to the variation of the scale $\mu = \mu_F = \mu_R$ by a factor of 2. The anomalous couplings are given dimensionless and an AC scale $\Lambda = 1$ TeV is assumed. These plots are also published in [219].

6.4. Jet Veto

To increase sensitivity to AC, additional jet radiation should be suppressed. In this way the phase space region where the leading vector boson recoils against another vector boson can be enhanced and the potential recoil against a jet reduced, as introduced in Fig. 6.2. The suppression of additional radiation is called a jet veto. This veto depends significantly on the jet definition (p_T , R , algorithm), but there are further choices that will be discussed in the following.

6.4.1. Fixed Jet Veto

The standard way to veto jets is based on a *fixed* p_T value [227]. Jets are reconstructed with a certain jet algorithm and clustering parameters. An event is rejected if it has additional radiation above the threshold $p_{T\text{veto}}$, which is typically on the order of 30 to 50 GeV. This procedure is equivalent to first grouping events in jet bins and then considering only the lowest bin. These jet bins correspond to the n_{jet} value shown in Table 6.1.

The fixed jet veto has drawbacks. In calculations of cross sections, the introduction of the veto scale leads to logarithms of the form $\alpha_s \ln^2(\mu^2/p_{T\text{veto}}^2)$. Here, μ is a process dependent scale. In the tails of distributions, like m_{VV} , which show the largest sensitivity to anomalous couplings, the difference between $p_{T\text{veto}}$ and m_{VV} will be large, such that the logarithmic corrections due to the veto become important. The logarithmic growth can, for example, be seen as a widening of scale bands in distributions. Similar results were obtained for a fixed veto in combination with LoopSim in [173, 174].

The arising logs can compensate the additional coupling factor and thereby delay the convergence of the perturbative series. This effect is known and can be cured by resumming the appearing logarithms to all orders [228–230]. A recent example includes the $N^3\text{LL}$ resummation for a jet veto in W^+W^- production [231]. Depending on the process the resummation can be improved by imposing a veto not on the p_T , but on beam thrust \mathcal{T}_{cm} [232]. Without

resummation, the jet veto dependency dominates the renormalization scale dependence at large invariant masses.

Additionally, the jet veto leads to an apparent reduction of the scale dependence. This behavior has been studied e.g. in [233, 234] for the NNLO corrections to Higgs boson production. As discussed there, one can construct a better uncertainty estimate than the naive scale variation, by projecting the scale dependence of the inclusive process on the vetoed cross section. Using these elaborate techniques, reliable predictions using fixed jet vetoes can be obtained.

Besides the theoretical downsides of a fixed jet veto, there is also phenomenological motivation to consider an alternative. A typical event of interest for an AC search has a diboson invariant mass of 1 TeV. As discussed in Section 6.2, these high-energy events are often accompanied by QCD radiation. At these high invariant diboson masses, jets up several hundred GeV are still soft in comparison to the scale of the event and should be allowed. A low fixed jet veto therefore removes a significant fraction of diboson events where the additional radiation is soft relative to the electroweak bosons, but hard in absolute terms of the veto. This removed phase space reduces the cross section in the tails which are already statistically limited. Typical events with $m_{WZ} > 1$ TeV will have a peak of jet radiation at a p_T of 50 to 100 GeV. Keeping a certain amount of this additional radiation improves the statistical uncertainty and thus the sensitivity in this phase space region.

6.4.2. Dynamical Jet Veto

A fixed jet veto introduces a jet veto scale, which induces logarithms of scale ratios. This can be avoided by adjusting the veto based on the kinematical scales present in the event. We call this a *dynamical jet veto*. As discussed in Section 6.3.1, the energy scale of an event is not uniquely identified. The choice of scale determines the effect of a constructed dynamical jet veto and how it affects other observables.

A dynamical jet veto rejects all jets above a threshold which scales with the energy in the event. Stated as a cut, this corresponds to

$$p_{T\text{jet}} < C (p_{TW} + p_{TZ}) . \quad (6.30)$$

Instead of the average p_T , other constructions like the maximum/minimum p_T of a certain particle class could be used or E_T , m_T , etc. The factor C can be adjusted to make the veto more or less restrictive. In this veto construction, $C = 0$ forbids any jet activity and corresponds to a fixed jet veto where the veto scale is identical to the jet resolution scale. $C \rightarrow \infty$ removes the jet veto and allows all additional radiation, including dijet events with soft vector bosons.

Instead of using only scalar values to determine the jet veto, one can use more information about the structure of the event. In a study of electroweak Sudakov logarithm at high transverse momenta [235], the following dynamical veto is introduced:

$$\left| \sum_i \vec{l}_{i,T} + \vec{p}_{T,\text{miss}} \right| < \rho \left(\sum_i |\vec{l}_{i,T}| + |\vec{p}_{T,\text{miss}}| \right) . \quad (6.31)$$

By comparing the vector sum of p_T to the scalar sum, an estimate is generated to find out, whether the vectors are “back-to-back”. When the vector sum has large absolute value, the vectors all point in a similar direction. For a small vector sum, there are cancellations which hint towards a “back-to-back” configuration. In [235] $\rho = 0.3$ has been chosen for the analysis. However, the distribution in ρ is continuously rising such that there is no obvious cut value.

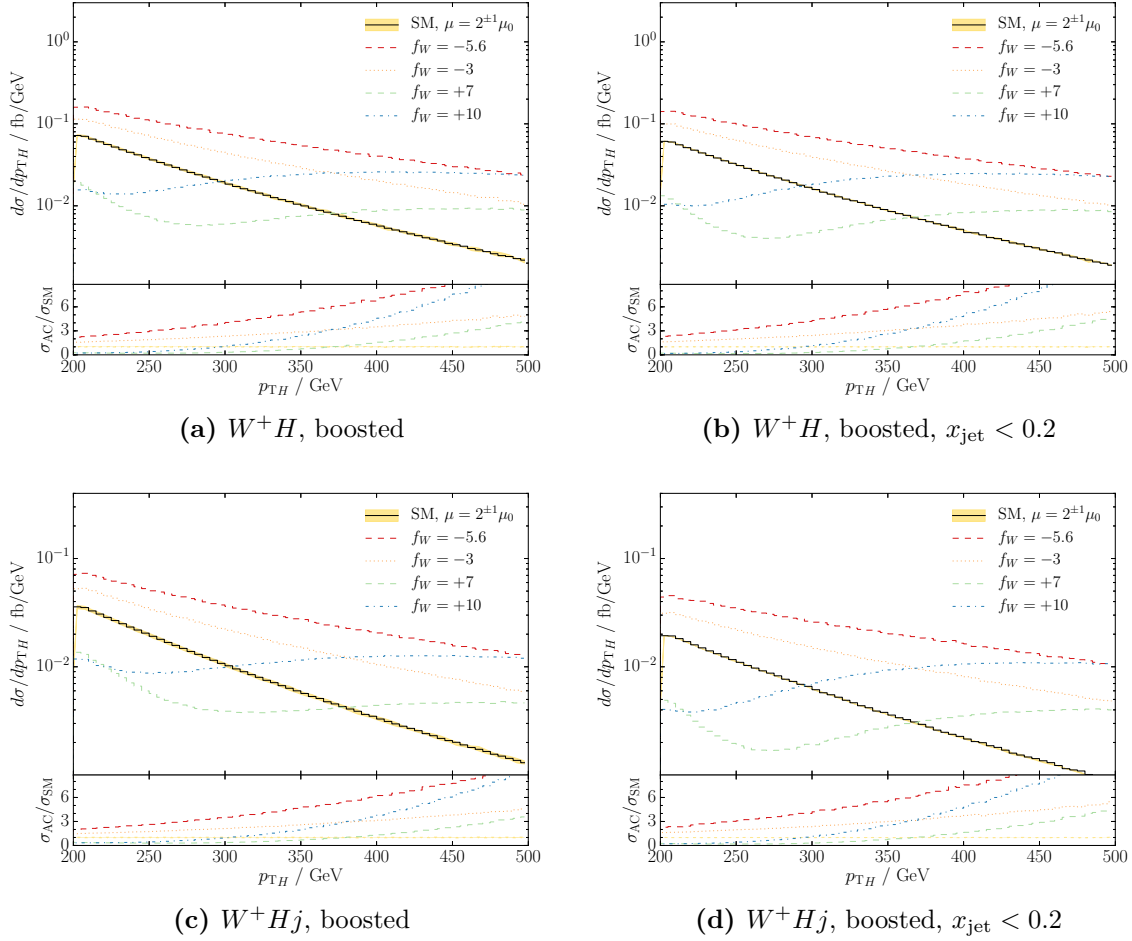


Figure 6.9: The Higgs boson transverse momentum is shown for the full sample (left) and with the jet veto of $x_{\text{jet}} < 0.2$ (right). The top row shows W^+H production at NLO, the bottom row W^+Hj production, where at least one jet passes the cuts. Both are calculated at NLO QCD. These plots are also published in [219].

6.4.3. Jet Veto based on x_{jet}

We want to use a veto based on the x_{jet} observable. x_{jet} is a measure of the jet activity in an event and is able to discriminate between recoils against a jet or against another electroweak boson. Since it is a ratio of transverse energies, it does not introduce a new scale and thus is not expected to generate large logarithmic corrections. Logarithmic enhancements are expected on the order of $\ln(x_{\text{jet}}) = O(1)$.

Based on the x_{jet} distribution shown in Fig. 6.8, a jet veto is introduced as requiring

$$x_{\text{jet}} < 0.2. \quad (6.32)$$

Depending on the analysis, the value of the cut has to be optimized. This value is well below 0.5 and thus not affected by higher order corrections and fixed-order artifacts, which appear for large x_{jet} values.

Figure 6.9 shows the effect of the jet veto on p_T distributions for WH production for both the SM and different AC values. In p_{T_H} the interference region and destructive interference

for positive coupling signs are clearly visible. For the shown coupling values, the destructive interference reaches its maximum at p_{TH} between 200 GeV and 300 GeV. For larger p_T values, the squared term dominates and there is no more dependence on the sign and the anomalous coupling effect increases. The x_{jet} veto is applied both to WH production and to WHj production, both computed at NLO QCD. In the first case it is applied to additional radiation from higher order corrections and in the second case the leading order already has one jet, such that the veto is applied to events with either one or two jets. Applying the veto leads to a small improvement of the ratio σ_{AC}/σ_{SM} . As shown in previous distributions in WH production, there is only a small amount of additional hard radiation. This is also visible in the only minuscule reduction of the cross section when the veto is applied.

In contrast to WH production, additional jet radiation has a greater impact on WZ production. Figure 6.10 shows the transverse momentum distributions for the W and Z boson in $WZ(j)$ production. The jet veto improves the sensitivity to anomalous couplings. For example in WZ production for p_{TZ} at 500 GeV the ratio σ_{AC}/σ_{SM} increases from 1.6 to 3 due to the veto. In WZj production (Figs. 6.10c and 6.10d) there is even more jet radiation, such that σ_{AC}/σ_{SM} in the p_{TZ} tail is around 1.3 without the veto and can be improved to more than 2 in the vetoed sample.

The interplay of kinematical limits and AC sensitive regions is visible in p_{TW} in Figs. 6.10e and 6.10f. For boosted cuts as given in Eq. (6.3), the Z boson is required to have $p_T > 200$ GeV. Then, the other particles in the event have to collectively provide a recoil of this amount. In the region of low W boson transverse momenta an additional high- p_T jet is required such that overall there is little AC sensitivity, as can be seen in Fig. 6.10e. Only for larger p_{TW} values the AC effects appear. On the other hand, the jet veto removes the region of low p_{TW} since it cuts away hard jets that could recoil. The veto reduces the absolute cross section significantly, but keeps most of the excess due to AC. For example at $p_{TW} = 250$ GeV the excess of AC over SM is $1 \cdot 10^{-3}$ fb/GeV both for the complete and the vetoed selection, while the SM cross section is reduced from $3.4 \cdot 10^{-3}$ fb/GeV to $1.7 \cdot 10^{-3}$ fb/GeV. The relative contribution of anomalous couplings σ_{AC}/σ_{SM} for $f_W = -5.6 \text{ TeV}^{-2}$ improves for p_{TW} from 1.3 to 1.5 at 250 GeV and from 1.7 to 2.8 at 500 GeV. Similarly for the transverse momentum values in p_{TZ} , the increase is from 1.1 to 1.5 and from 1.3 to 2.4, respectively.

The scale band remains narrow for the vetoed sample. It does not show the characteristic widening of a fixed jet veto. Nevertheless, the scale band is expected to underestimate higher corrections in the same way as discussed in Section 6.4.1 for the fixed jet veto.

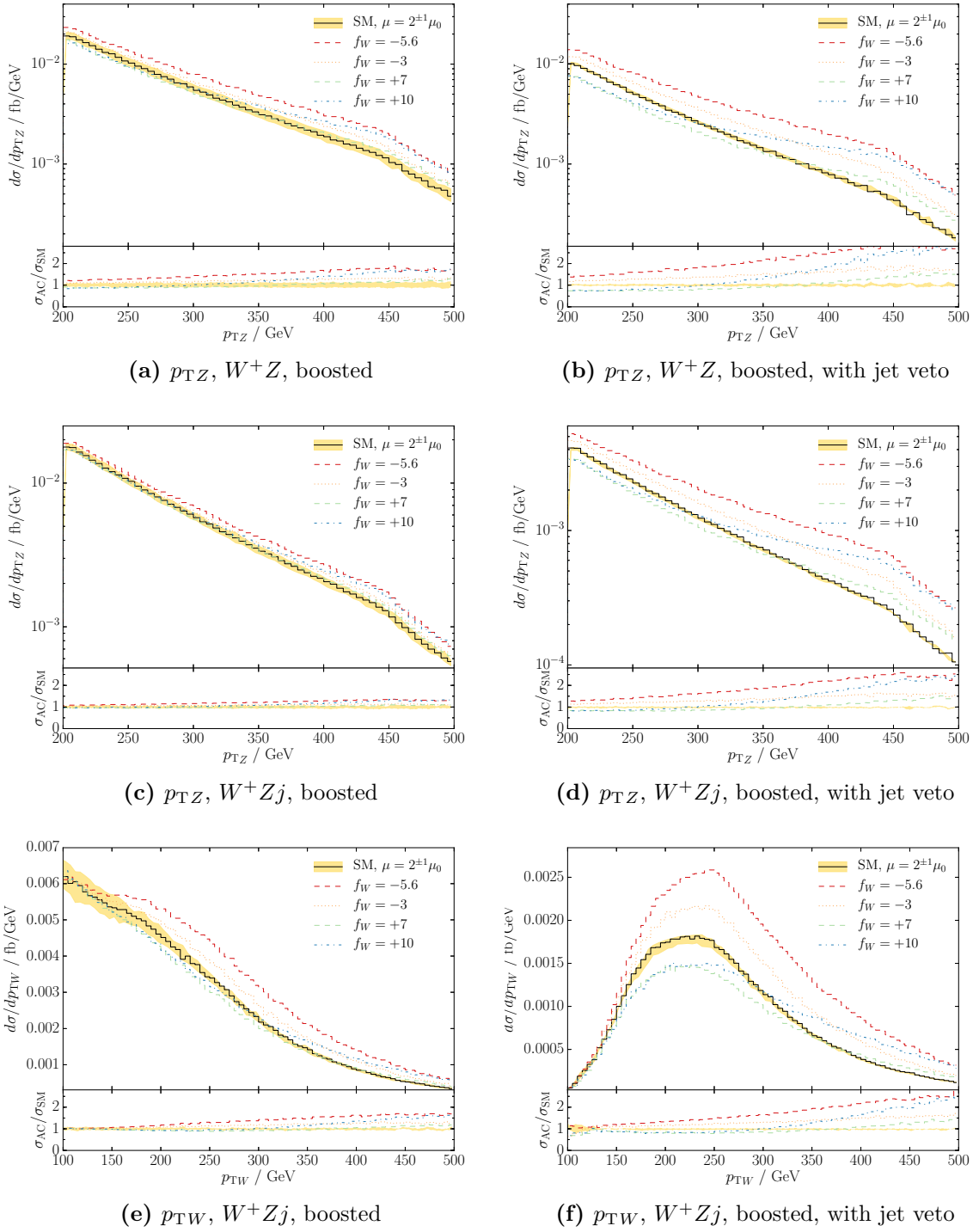


Figure 6.10: The transverse momenta of the Z and W boson in WZ and WZj production are shown for the inclusive sample (left) and with the jet veto (right). These plots are also published in [219].

6.5. Anomalous Couplings and \bar{n} NLO QCD in WZ Production

Additional radiation and its treatment are relevant for anomalous coupling studies in WZ production. This makes higher order corrections to jet emission relevant and LoopSim corrections at \bar{n} NLO provide an improved prediction in the relevant phase space region. This allows to study corrections to the x_{jet} observable and anomalous couplings. This analysis and the plots shown in this section were published in [92].

6.5.1. Numerical Setup

For this analysis, the input values are used as defined in Section 6.1. The cuts are modified slightly compared to Eq. (6.2):

$$\begin{aligned} p_{Tl} &> 15 \text{ GeV}, & p_{Tj} &> 30 \text{ GeV}, & \cancel{p}_T &> 30 \text{ GeV}, \\ |y_j| &< 4.5, & |\eta| &< 2.5, & R_{lj} &> 0.4, \\ 120 \text{ GeV} &> m_{ll} &> 60 \text{ GeV}. \end{aligned} \tag{6.33}$$

The R_{ll} cut is removed as argued in Section 6.3.2 and the other cuts updated to the values used by the most recent experimental analyses. The center of mass energy is 13 TeV and NNPDF23 [36] is used as parton distribution function. The renormalization and factorization scale is chosen to be $\mu_0 = H_T$ as given in Eq. (6.21). The theoretical uncertainty band is constructed by a variation of both scales by a factor of 2: $\mu_R = \mu_F = \{0.5, 2\}\mu_0$.

6.5.2. WZ production at \bar{n} NLO QCD

First results for WZ production at \bar{n} NLO QCD were presented in [173]. As shown there, the corrections at \bar{n} NLO can be sizable and depend on the selected phase space region.

Corrections are on the order of 25% for distributions of typical inclusive observables. For example, the p_T of the hardest lepton in the event (called $p_{Tl,\text{max}}$ in the following), is enhanced by 25% at 300 GeV, as can be seen in Fig. 6.11 on the left.

Observables that are sensitive to the number of final state jets and thus enhanced by extra radiation can get more sizeable corrections. For example, $H_{T,\text{jets}}$ at 1 TeV gets a five-fold increase as visible in Fig. 6.11 on the right. In general, the scale variation at NLO does not cover the \bar{n} NLO result. Relying on scale variation as an estimate for higher order corrections is not always sufficient. In WZ production at \bar{n} NLO new topologies appear, which are not present at NLO. Most notably this includes dijet production with two soft vector bosons. Adding radiation beyond \bar{n} NLO does not lead to new topologies and should therefore give smaller corrections.

6.5.3. \bar{n} NLO QCD Corrections with Anomalous Couplings

LoopSim is independent of the specifics of the electroweak part of the calculation and can therefore also be applied to processes involving anomalous couplings. The full amplitude, including the $\mathcal{M}_{\text{SM}}^* \mathcal{M}_{\text{AC}}$ and $|\mathcal{M}_{\text{AC}}|^2$ terms, is passed along to LoopSim. The two terms can be disentangled by separating the linear and squared dependence on the AC coupling value.

The relative contribution to the cross section of these two terms can be observed by choosing the coupling sign such that the interference is destructive. The $|\mathcal{M}_{\text{AC}}|^2$ term always interferes constructively and cancels the destructive interference once its size becomes competitive.

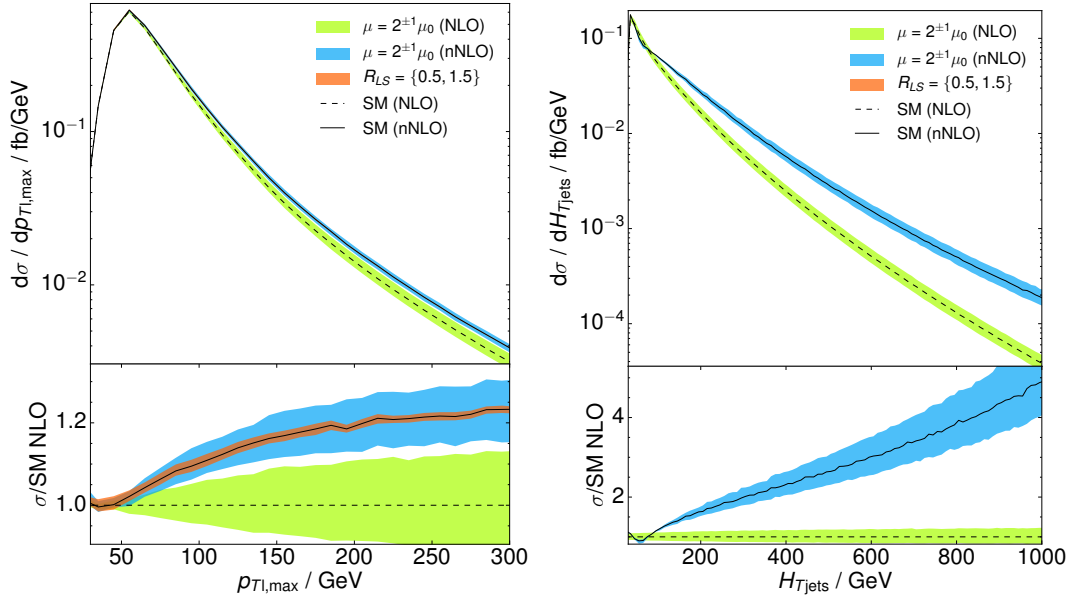


Figure 6.11: For WZ production two representative distributions are shown. For this and the following plots, cross sections at NLO in QCD are dashed, while \bar{n} NLO QCD is shown as solid lines. \bar{n} NLO effects range from 25% or below as seen on the left for the p_T of the hardest lepton ($p_{T1,max}$) to a five-fold increase in the tail of $H_{T,jets}$. The scale variation by a factor of two is given as a band for NLO (green) and \bar{n} NLO (blue). In general, the NLO scale variation band does not cover the \bar{n} NLO prediction. At \bar{n} NLO there is an additional parameter (R_{LS}) in the LoopSim clustering procedure that can approximate uncertainties in the LoopSim procedure. The variation of this parameter is shown as an orange band. The dependence is small for most observables and phase space regions and is only relevant for observables that are particularly sensitive to extra radiation. A large dependence on R_{LS} would hint towards relevant contributions from the finite piece of the virtual corrections. From [92].

The interference as shown in Fig. 6.12 is dominant around 150 GeV. The squared term dominates starting at around 300 GeV. This scale is where

$$\frac{f}{\Lambda^2} \cdot p_T^2 \approx 1. \quad (6.34)$$

For $f_W/\Lambda^2 = 10 \text{ TeV}^{-2}$ this happens at $p_T \approx 300 \text{ GeV}$.

Comparing Figs. 6.11 and 6.12, one can see that the effect of anomalous couplings is of a comparable size and appears in a similar phase space region as the \bar{n} NLO corrections. This is shown in Fig. 6.13 where both the SM at \bar{n} NLO and AC with NLO corrections are shown. Therefore NLO QCD might be insufficient to put limits on AC. A SM description beyond NLO is necessary.

VBFNLO interfaced to LoopSim can be used to compute AC cross sections at \bar{n} NLO QCD accuracy. QCD corrections do not factorize from AC and can thus lead to non-trivial changes to AC limits derived in experiments. Figure 6.14 shows the \bar{n} NLO/NLO K-factor for several values of anomalous couplings and the SM. In the high- p_T region, where LoopSim is a good approximation, the K-factor varies between 1.1 and 1.3 depending on the anomalous coupling value. Due to this dependence, a factorization of QCD corrections and AC contributions is not accurate and the full QCD+AC amplitude has to be calculated.

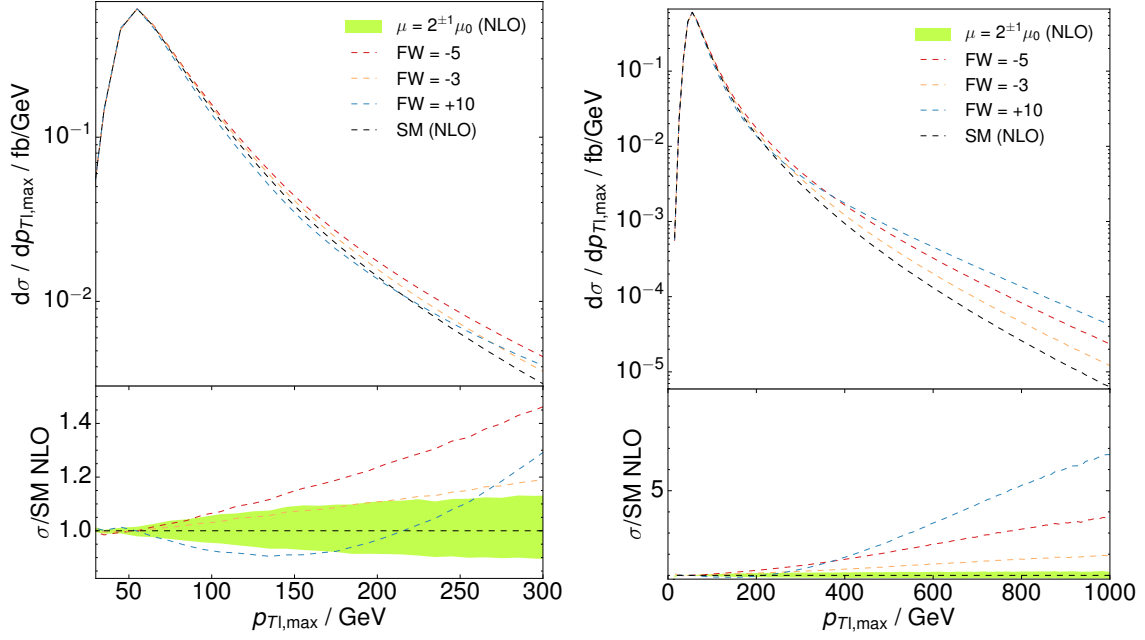


Figure 6.12: The p_T of the hardest lepton in WZ production at NLO QCD is shown for the SM (black) and the \mathcal{O}_W operator with different couplings (colored) as a typical representative of AC at different momentum scales. The AC contribution grows with the momentum and leads to most sizeable differences in the tail of this distribution. At 1 TeV (right) the difference to the SM can be a factor of 5. At small $p_{T1,max}$ values (left), the contribution of the interference term is visible. From [92].

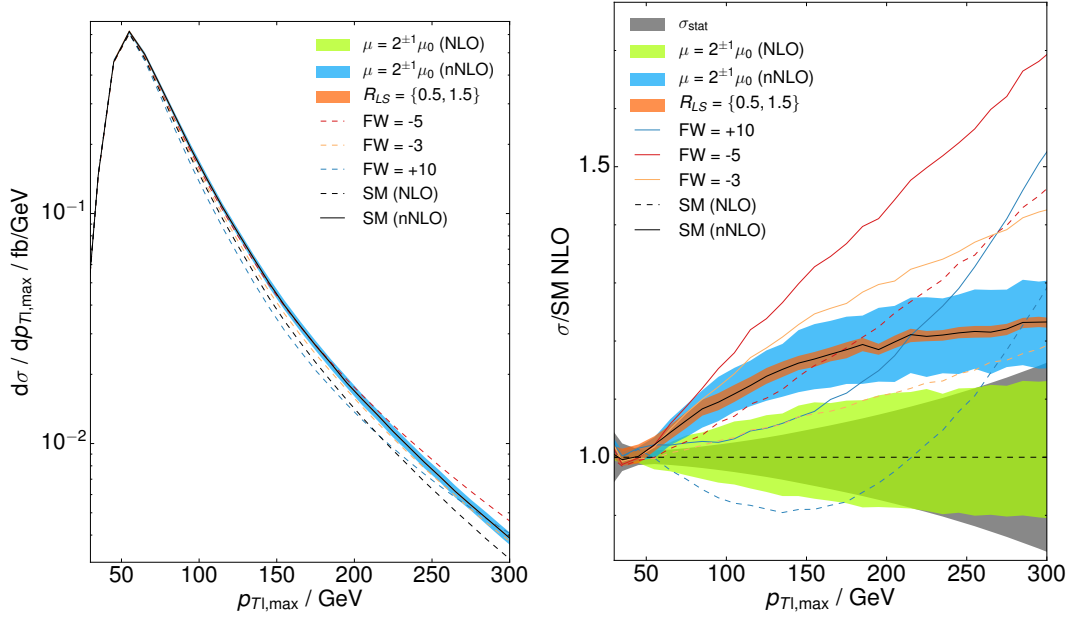


Figure 6.13: Combining Figs. 6.11 and 6.12, the p_T of the hardest lepton is shown for the SM at \bar{n} NLO (solid black) and for AC at NLO (colored dashed) on the left. The right shows the same distribution, but normalized to the SM NLO prediction to better visualize the ratios of the individual lines. Both \bar{n} NLO and AC can lead to deviations from the SM on the order of 25% in this observable and phase space region. The AC prediction is shown at \bar{n} NLO QCD as solid colored lines. From [92].

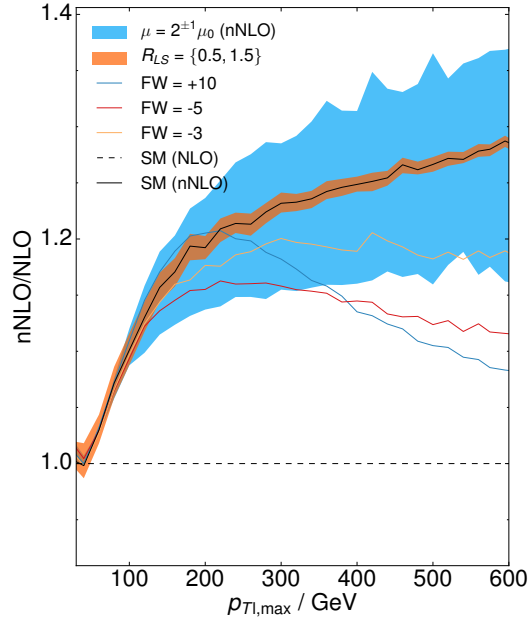


Figure 6.14: For the SM and several AC coupling values, the K-factor \bar{n} NLO/NLO is shown for the observable $p_{T1,max}$. This K-factor depends significantly on the AC value and reaches values between 1.1 and 1.3 for $p_{T1,max} = 600$ GeV. Fluctuations visible in this plot are due to the numerical Monte Carlo integration. From [92].

6.5.4. Dynamical Jet Veto

To improve the sensitivity to AC, also at \bar{n} NLO, the dynamical jet veto introduced in Section 6.3.3 can be used. For this analysis x_{jet} as defined in Eq. (6.25) based on E_T is used:

$$x_{jet} = \frac{E_{T,jets}}{E_{T,jets} + E_{T,W} + E_{T,Z}}, \text{ where } E_T = E \frac{|\vec{p}_T|}{|\vec{p}|}. \quad (6.35)$$

At \bar{n} NLO there are events with 0, 1 and 2 partons/jets. LoopSim moves events between all three of these configurations depending on the momentum configuration, such that we expect the x_{jet} observables to receive corrections at \bar{n} NLO.

The distribution in x_{jet} at NLO and \bar{n} NLO is shown in Fig. 6.15 for the SM and AC. The \bar{n} NLO corrections are non-flat as a function of x_{jet} and rise to 1.3 at $x_{jet} = 0.4$. As discussed in Section 6.3, the region above $x_{jet} = 0.5$ can only be reached by dijet events. In addition to the previous study, the LoopSim description also fills the $x_{jet} = 0$ bin with events without resolved jets.

AC increase the cross section at small x_{jet} values, while they align with the SM prediction for large x_{jet} values. Introducing a cut $x_{jet} < 0.2$ removes most of the jet-recoil type events that are not sensitive to anomalous couplings and at the same time removes the phase space region with the largest \bar{n} NLO corrections. The \bar{n} NLO sample allows to study jet vetoes on a combination of 0-, 1- and 2-jet events, which gives a more complete picture on the increases in sensitivity than only considering the 0-jet or 1-jet process at NLO.

In Fig. 6.16, a veto based on x_{jet} is applied to improve the sensitivity to anomalous couplings. This veto cuts away jet dominated events and reduces the \bar{n} NLO corrections. Compared to the +25% corrections in the inclusive case, for $x_{jet} < 0.2$ (left) the \bar{n} NLO corrections are even

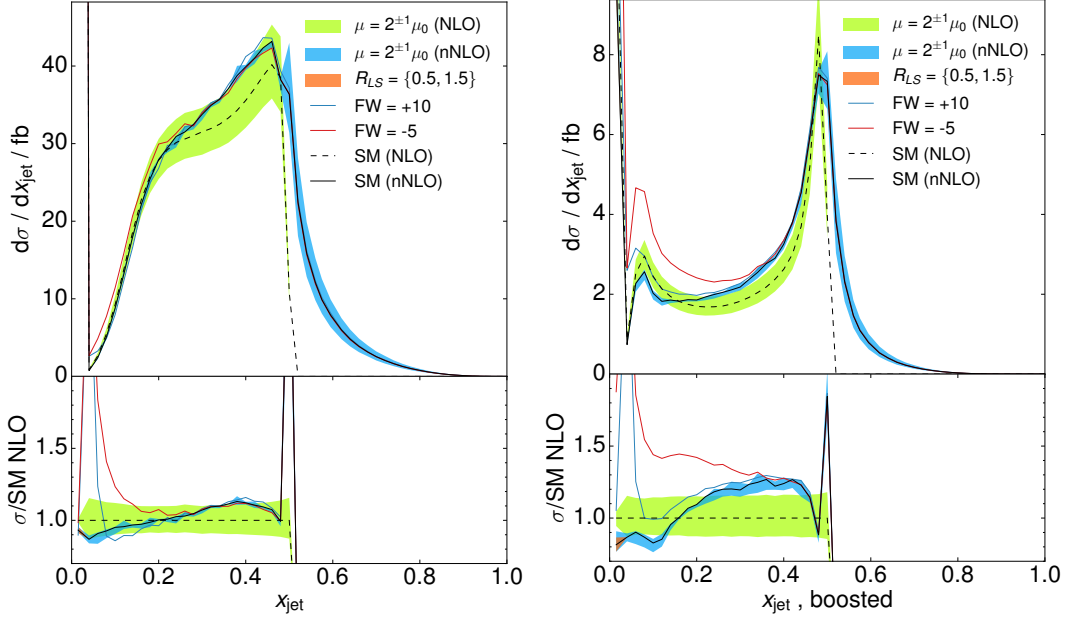


Figure 6.15: For WZ production at NLO, x_{jet} is shown, as given in Eq. (6.35), for inclusive cuts (left) and boosted cuts (right). For boosted cuts $p_{TZ} > 200$ GeV is required. Especially in the boosted region the division in two regions is visible. Events have two recoiling vector bosons for small x_{jet} values, while for $x_{\text{jet}} \approx 0.5$ the boosted vector boson recoils against a jet. The latter configuration is less sensitive to AC, such that to increase the sensitivity a cut, $x_{\text{jet}} < 0.2$ to 0.3 , can be introduced. From [92].

negative (-10%), while for $x_{\text{jet}} < 0.4$ (right) \bar{n} NLO falls nearly on top of NLO. In general, vetoing resolved jet emissions will result in a decrease of higher order corrections, which explicitly generate resolved emissions.

The veto also reduces the scale dependence. This is a known artifact of jet vetoed cross sections and shows that scale variation is, in this case, not a suitable approximation of the theoretical uncertainties. A more elaborate construction of an uncertainty estimate was discussed in Section 6.4.1.

To compare the deviations due to anomalous couplings to the potential experimental reach, an estimate of the statistical uncertainty is shown. For this, an integrated luminosity of 300 fb^{-1} is assumed and a factor 4 multiplied to the cross section to cover all lepton flavor combinations in the decays. The correct factor is not exactly 4, since in final states like $\mu^+ \nu_\mu \mu^+ \mu^-$ the Z boson can be reconstructed from two potential combinations of muons, which will lead to some reconstruction uncertainty. The shown band is only a rough and rather optimistic estimate of the experimental accuracy, since there are also systematic uncertainties and many of the technical intricacies of a real analysis are neglected here.

For $p_{T1,\text{max}}$ the \bar{n} NLO corrections both in size and shape depend significantly on the AC value as shown in Fig. 6.14. Therefore, approximating QCD corrections to AC predictions by rescaling them with a constant K-factor derived from the SM is insufficient.

In Fig. 6.17 the differential K-factor for x_{jet} is shown, which does not depend on the AC value. Therefore one could try to factorize AC and \bar{n} NLO corrections and, for example, apply a K-factor derived for the SM to AC predictions by binning it in x_{jet} . Nevertheless, the best overall description would be a NNLO calculation including anomalous couplings.

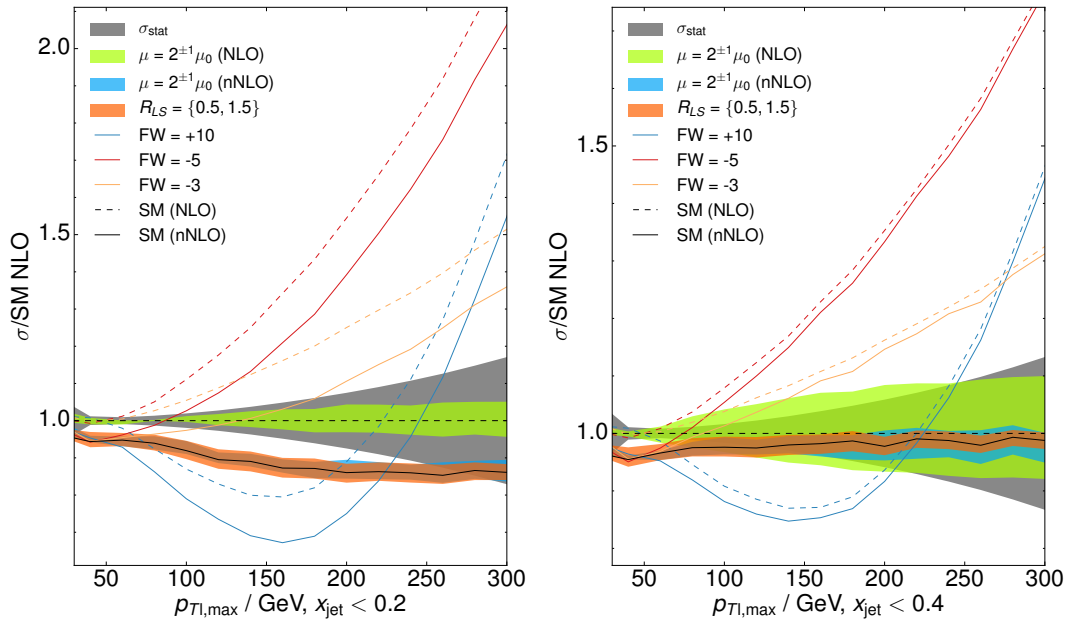


Figure 6.16: The cross section differential in $p_{T1,max}$ is shown for several anomalous coupling values at NLO and \bar{n} NLO normalized to the SM prediction at NLO. A dynamical jet veto of $x_{jet} < 0.2$ (left) and $x_{jet} < 0.4$ (right) is applied. Scale variation bands are given at NLO (green) and \bar{n} NLO (blue) as well as the R_{LS} dependence in orange. As a rough comparison to the potential experimental reach, the statistical uncertainty is shown as a gray band. From [92].

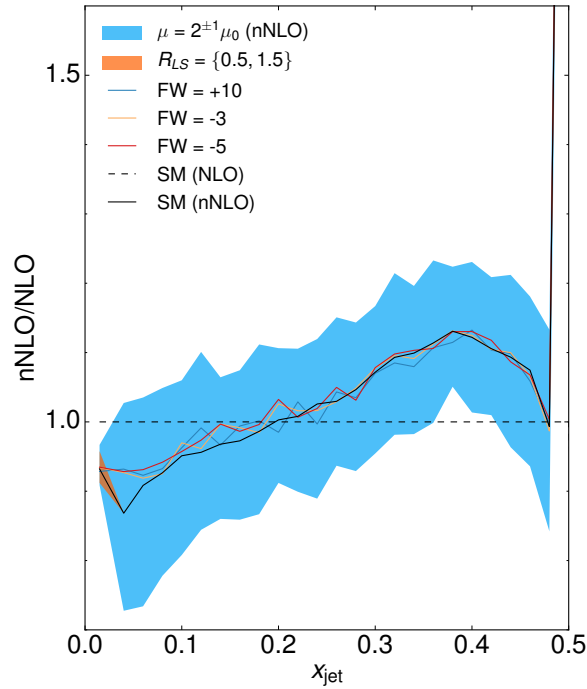


Figure 6.17: The ratio of \bar{n} NLO over NLO is shown for x_{jet} for the SM and several AC values. The K-factor depends on the value of x_{jet} but is independent of the used AC value. From [92].

Summary and Conclusion

In this thesis, diboson production at the LHC based on the example of WZ and WH production is discussed. While predictions are commonly based on NLO calculations, this thesis uses \bar{n} NLO corrections to distributions using the LoopSim approach in combination with VBFNLO. These corrections are especially relevant for events with high transverse momentum where the corrections can be large and outside the NLO scale variation band.

Anomalous couplings using an Effective Field Theory approach are a useful tool to parametrize general deviations from the SM. Diboson production is an interesting channel to study triple gauge couplings and allows to set competitive limits compared to global fits. However, Effective Field Theories have a limited range of validity and current limits push them to the edge of their applicability, such that detailed understanding of anomalous coupling effects is necessary.

To improve the sensitivity of anomalous coupling searches, events with hard jet radiation should be removed. This thesis introduces a description of the transverse event shape of the WZj final state using newly constructed variables x_{jet} , x_Z and x_W to better understand QCD radiation patterns. x_{jet} is defined as the relative contribution of the jet transverse energy to the sum of transverse energies of jet, W and Z boson:

$$x_{\text{jet}} = \frac{E_{T,\text{jets}}}{E_{T,\text{jets}} + E_{T,W} + E_{T,Z}}. \quad (7.1)$$

x_Z and x_W are constructed similarly. The dependence of the cross section on a pair of these variables, x_{jet} and x_Z , can be visualized in a Dalitz-like 2D plot and allows to distinguish between jet and electroweak dominated event topologies. In WZ production a large fraction of events has a hard jet recoiling against a boosted vector boson. In contrast, the contribution of this topology is smaller in WH production. There the W and Higgs boson are produced via an intermediate W boson, while in WZ production both bosons can be connected to a quark line, which leads to logarithmic enhancements of the vector boson emission from a hard jet.

Additional jet radiation is often removed using a fixed- p_T jet veto. In this thesis, a dynamical jet veto based on x_{jet} is introduced and studied in WZ and WH production. The dynamical jet veto is theoretically better behaved than a fixed veto and scales with energy in the event. It thereby includes more phase space for jet emissions in highly boosted events. Especially for WZ production the veto improves the sensitivity to anomalous couplings. Using this veto, one can also study the interference region of anomalous couplings with the SM. This region can be competitive in a high-luminosity scenario at the LHC.

Higher order corrections at \bar{n} NLO and anomalous coupling effects are of a comparable size in the anomalous coupling search region. Therefore, a combined analysis is necessary. Since both

corrections grow with increasing transverse momentum, not-included higher order corrections might be mistaken for anomalous couplings. Higher order corrections depend on the anomalous coupling value, such that for general observables, like transverse momenta, corrections to the SM can not be extrapolated to anomalous coupling predictions. However, corrections to the x_{jet} variable show negligible dependence on the anomalous coupling value, such that x_{jet} might also be of interest when mapping higher order corrections from the SM to scenarios beyond the SM.

In addition, parallelization using MPI was implemented in VBFNLO to improve the runtime of the cross section calculation for complex processes and improve the convergence and phase space coverage for these cases. The implementation was validated against the previous code version and shows good scaling with the number of cores. Using MPI the calculation can in principle scale to running a single job on a complete cluster, although for parallel calculations on a heterogeneous cluster additional work is needed. As part of the implementation new choices for the random number generator were introduced and the VEGAS implementation optimized, which improves the runtime also for non-parallel calculations.

The recent achievements in NNLO calculations as well as in merging multiple fixed order calculations and matching them to parton showers will improve the precision of predictions for LHC cross sections. At the same time, the LHC experiments are able to measure distributions in diboson production at higher energies while also increasing the sensitivity to interference effect at smaller energies. This combination makes the LHC an invaluable tool to set limits on and potentially discover New Physics in triple gauge couplings.

Future analyses of diboson production could go beyond NNLO in the description of diboson events by including the existing NLO calculations of $VVjj$ production or matching to a parton shower, which improves the description of x_{jet} . Further studies could also consider corrections to the semileptonic decays and their sensitivity to anomalous couplings. Another aspect is the study of decay angles which give insight into vector boson helicities and are particularly sensitive to New Physics.

Appendix

A. LoopSim events

LoopSim is interfaced to VBFNLO using LHE files. This interface is introduced in Section 5.6. Additional information in the form of comments is passed along to signal which events correspond to virtual corrections or the real emission. In the real emission an index connects the subtraction terms which belong to a certain event and have to be treated together to ensure a correct error estimate in distributions. For WZj production example outputs are shown for the virtual corrections in Listing 7.1 and the real corrections in Listing 7.2.

```

<LesHouchesEvents version="1.0">
<!--
File generated with VBFNLO - parton level MC program (LO)
-->
<init>
  2212    2212  7.000000E+03  7.000000E+03      0      0    21200    21200
    ↪ 2      1
  2.785467E-02  2.126556E-03  0.000000E+00  640
</init>
<event>
  9   640 -7.929671E-03  8.375747E+01  7.556254E-03  1.185817E-01
  81  -1   0   0   0   0  0.0000000000000000E+00  0.0000000000000000E+00
    ↪  1.759863609218195E+02  1.759863609218195E+02  0.0000000000000000E+00  0.0E+00
    ↪  9.0E+00
  81  -1   0   0   0   0  0.0000000000000000E+00  0.0000000000000000E+00
    ↪ -1.689720569845746E+02  1.689720569845746E+02  0.0000000000000000E+00  0.0E+00
    ↪  9.0E+00
  81   1   0   0   0   0 -4.658829641120308E+01  1.303163355277379E+02
    ↪ -1.203272434380624E+01  1.389158130775978E+02  0.0000000000000000E+00  0.0E+00
    ↪  9.0E+00
  24   0   0   0   0   0 -1.116535864138272E+01 -2.503071915152502E+01
    ↪ -1.999210739784107E+01  4.599421054477074E+01  3.105770291886808E+01  0.0E+00
    ↪  0.0E+00
  23   0   0   0   0   0  5.775365505258581E+01 -1.052856163762128E+02
    ↪  3.903913567889218E+01  1.600483942840255E+02  9.834067678579302E+01  0.0E+00
    ↪  0.0E+00
 -11   1   0   0   0   0  3.160780453972312E+00 -2.207466387926429E+01
    ↪ -2.188446633859767E+01  3.124437846054748E+01  0.0000000000000000E+00  0.0E+00
    ↪  0.0E+00
  12   1   0   0   0   0 -1.432613909535504E+01 -2.956055272260727E+00
    ↪  1.892358940756601E+00  1.474983208422325E+01  0.0000000000000000E+00  0.0E+00
    ↪  0.0E+00
 -11   1   0   0   0   0  1.689471131390520E+01 -1.789126305482286E+01
    ↪ -3.190880237294856E+01  4.029516389038458E+01  0.0000000000000000E+00  0.0E+00
    ↪  0.0E+00
  11   1   0   0   0   0  4.085894373868061E+01 -8.739435332138999E+01
    ↪  7.094793805184074E+01  1.197532303936409E+02  0.0000000000000000E+00  0.0E+00
    ↪  0.0E+00
# virt  0  1
</event>
<event>
  [...]
</event>
[...]
```

Listing 7.1: Example output for LHE events of virtual corrections with additional LoopSim annotation.

```

[...]
<event>
  10  640  1.312752E-03  1.047735E+02  7.556254E-03  1.146925E-01
  81  -1   0   0   0   0  0.000000000000000E+00  0.000000000000000E+00
    ↪  1.028208124435631E+02  1.028208124435631E+02  0.000000000000000E+00  0.0E+00
    ↪  9.0E+00
  81  -1   0   0   0   0  0.000000000000000E+00  0.000000000000000E+00
    ↪ -2.009333226847219E+03  2.009333226847219E+03  0.000000000000000E+00  0.0E+00
    ↪  9.0E+00
  81   1   0   0   0   0 -1.331871562018235E+01 -1.564577471007879E+01
    ↪ -4.272971623498581E+02  4.277908874722447E+02  0.000000000000000E+00  0.0E+00
    ↪  9.0E+00
  81   1   0   0   0   0  3.642659451635352E+01  1.125965643240243E+02
    ↪ -1.360228939633365E+03  1.365367222142725E+03  0.000000000000000E+00  0.0E+00
    ↪  9.0E+00
  24   0   0   0   0   0  1.892243464211417E+01 -4.076712454409633E+01
    ↪ -1.919798467911598E+01  1.680535181098962E+02  1.607899417158756E+02  0.0E+00
    ↪  0.0E+00
  [...]
  11   1   0   0   0   0 -1.340869002367992E+01 -7.482983087600350E+01
    ↪ -8.405486681574227E+01  1.133336542801587E+02  0.000000000000000E+00  0.0E+00
    ↪  0.0E+00
# real  0  1
</event>
<event>
  10  640 -8.240591E-07  1.047735E+02  7.556254E-03  1.146925E-01
  81  -1   0   0   0   0  0.000000000000000E+00  0.000000000000000E+00
    ↪  1.013918940402587E+02  1.013918940402587E+02  0.000000000000000E+00  0.0E+00
    ↪  9.0E+00
  81  -1   0   0   0   0  0.000000000000000E+00  0.000000000000000E+00
    ↪ -2.009333226847219E+03  2.009333226847219E+03  0.000000000000000E+00  0.0E+00
    ↪  9.0E+00
  81   1   0   0   0   0  2.310787889617117E+01  9.695078961394546E+01
    ↪ -1.788955020386528E+03  1.791729191211666E+03  0.000000000000000E+00  0.0E+00
    ↪  9.0E+00
  81   1   0   0   0   0  0.000000000000000E+00  0.000000000000000E+00
    ↪  0.000000000000000E+00  0.000000000000000E+00  0.000000000000000E+00  0.0E+00
    ↪  9.0E+00
  24   0   0   0   0   0  1.892243464211417E+01 -4.076712454409633E+01
    ↪ -1.919798467911598E+01  1.680535181098962E+02  1.607899417158756E+02  0.0E+00
    ↪  0.0E+00
  [...]
  11   1   0   0   0   0 -1.340869002367992E+01 -7.482983087600350E+01
    ↪ -8.405486681574227E+01  1.133336542801587E+02  0.000000000000000E+00  0.0E+00
    ↪  0.0E+00
# real  1  1
</event>
<event>
  [...]
# real  2  1
</event>
  [...]
<event>
  [...]
# real  10  1
</event>

```

Listing 7.2: Example output for LHE events of real emission and subtraction events with additional LoopSim annotation. For subtraction terms the additional emission is listed with zero momentum and redistributed according to the prescription by Catani and Seymour Section 2.3.

Bibliography

- [1] **ATLAS**, G. Aad *et al.*, “Observation of a new particle in the search for the Standard Model Higgs boson with the ATLAS detector at the LHC,” *Phys. Lett.* **B716** (2012) 1–29, [arXiv:1207.7214 \[hep-ex\]](#).
- [2] **CMS**, S. Chatrchyan *et al.*, “Observation of a new boson at a mass of 125 GeV with the CMS experiment at the LHC,” *Phys. Lett.* **B716** (2012) 30–61, [arXiv:1207.7235 \[hep-ex\]](#).
- [3] H. D. Politzer, “Reliable Perturbative Results for Strong Interactions?,” *Phys. Rev. Lett.* **30** (1973) 1346–1349.
- [4] D. J. Gross and F. Wilczek, “Ultraviolet Behavior of Nonabelian Gauge Theories,” *Phys. Rev. Lett.* **30** (1973) 1343–1346.
- [5] H. Fritzsch, M. Gell-Mann, and H. Leutwyler, “Advantages of the Color Octet Gluon Picture,” *Phys. Lett.* **B47** (1973) 365–368.
- [6] M. Gell-Mann, “A Schematic Model of Baryons and Mesons,” *Phys. Lett.* **8** (1964) 214–215.
- [7] S. Weinberg, “A Model of Leptons,” *Phys. Rev. Lett.* **19** (1967) 1264–1266.
- [8] A. Salam and J. C. Ward, “Weak and electromagnetic interactions,” *Il Nuovo Cimento* **11** no. 4, (1959) 568–577.
- [9] A. Salam, “Weak and Electromagnetic Interactions,” *Conf. Proc.* **C680519** (1968) 367–377.
- [10] S. L. Glashow, “Partial Symmetries of Weak Interactions,” *Nucl. Phys.* **22** (1961) 579–588.
- [11] F. Englert and R. Brout, “Broken Symmetry and the Mass of Gauge Vector Mesons,” *Physical Review Letters* **13** no. 9, (1964) 321–323.
- [12] P. Higgs, “Broken Symmetries and the Masses of Gauge Bosons,” *Physical Review Letters* **13** no. 16, (1964) 508–509.
- [13] P. Higgs, “Broken symmetries, massless particles and gauge fields,” *Phys. Lett.* **12** (1964) 132–133.
- [14] D. Hanneke, S. F. Hoogerheide, and G. Gabrielse, “Cavity Control of a Single-Electron Quantum Cyclotron: Measuring the Electron Magnetic Moment,” *Phys. Rev.* **A83** (2011) 052122, [arXiv:1009.4831 \[physics.atom-ph\]](#).
- [15] **Muon g-2**, G. W. Bennett *et al.*, “Final Report of the Muon E821 Anomalous Magnetic Moment Measurement at BNL,” *Phys. Rev.* **D73** (2006) 072003, [arXiv:hep-ex/0602035 \[hep-ex\]](#).

- [16] T. Blum *et al.*, “The Muon ($g-2$) Theory Value: Present and Future,” [arXiv:1311.2198 \[hep-ph\]](#).
- [17] **CMS**, “Search for new physics in high mass diphoton events in proton-proton collisions at 13TeV,” Tech. Rep. CMS-PAS-EXO-15-004, 2015.
- [18] **ATLAS**, “Search for resonances decaying to photon pairs in 3.2 fb^{-1} of pp collisions at $\sqrt{s} = 13 \text{ TeV}$ with the ATLAS detector,” Tech. Rep. ATLAS-CONF-2015-081, 2015.
- [19] **CMS**, “Search for new physics in high mass diphoton events in 3.3 fb^{-1} of proton-proton collisions at $\sqrt{s} = 13 \text{ TeV}$ and combined interpretation of searches at 8 TeV and 13 TeV,” Tech. Rep. CMS-PAS-EXO-16-018, 2016.
- [20] **ATLAS**, “Search for resonances in diphoton events with the ATLAS detector at $\sqrt{s} = 13 \text{ TeV}$,” Tech. Rep. ATLAS-CONF-2016-018, 2016.
- [21] **ATLAS**, G. Aad *et al.*, “Search for high-mass diboson resonances with boson-tagged jets in proton-proton collisions at $\sqrt{s} = 8 \text{ TeV}$ with the ATLAS detector,” *JHEP* **12** (2015) 055, [arXiv:1506.00962 \[hep-ex\]](#).
- [22] **CMS**, “Updated measurements of Higgs boson production in the diphoton decay channel at $\sqrt{s} = 13 \text{ TeV}$ in pp collisions at CMS,” Tech. Rep. CMS-PAS-HIG-16-020, 2016.
- [23] **ATLAS**, “Measurement of fiducial, differential and production cross sections in the $H \rightarrow \gamma\gamma$ decay channel with 13.3 fb^{-1} of 13 TeV proton-proton collision data with the ATLAS detector,” Tech. Rep. ATLAS-CONF-2016-067, 2016.
- [24] **CMS**, “Measurements of properties of the Higgs boson decaying into four leptons in pp collisions at $\sqrt{s} = 13 \text{ TeV}$,” Tech. Rep. CMS-PAS-HIG-16-041, 2017.
- [25] **ATLAS**, “Study of the Higgs boson properties and search for high-mass scalar resonances in the $H \rightarrow ZZ^* \rightarrow 4\ell$ decay channel at $\sqrt{s} = 13 \text{ TeV}$ with the ATLAS detector,” Tech. Rep. ATLAS-CONF-2016-079, 2016.
- [26] M. Rubin, G. P. Salam, and S. Sapeta, “Giant QCD K-factors beyond NLO,” *JHEP* **09** (2010) 084, [arXiv:1006.2144 \[hep-ph\]](#).
- [27] K. Arnold *et al.*, “VBFNLO: A Parton level Monte Carlo for processes with electroweak bosons,” *Comput. Phys. Commun.* **180** (2009) 1661–1670, [arXiv:0811.4559 \[hep-ph\]](#).
- [28] K. Arnold *et al.*, “VBFNLO: A Parton Level Monte Carlo for Processes with Electroweak Bosons – Manual for Version 2.5.0,” [arXiv:1107.4038 \[hep-ph\]](#).
- [29] J. Baglio *et al.*, “Release Note - VBFNLO 2.7.0,” [arXiv:1404.3940 \[hep-ph\]](#).
- [30] **Particle Data Group**, C. Patrignani *et al.*, “Review of Particle Physics,” *Chin. Phys.* **C40** no. 10, (2016) 100001.
- [31] P. Skands, “Introduction to QCD,” in *Proceedings, Theoretical Advanced Study Institute in Elementary Particle Physics: Searching for New Physics at Small and Large Scales (TASI 2012): Boulder, Colorado, June 4-29, 2012*, pp. 341–420. [arXiv:1207.2389 \[hep-ph\]](#).

- [32] User:TriTertButoxy, User:Stannered, “Elementary particle interactions.” https://commons.wikimedia.org/wiki/File:Elementary_particle_interactions.svg, accessed 2017-04-24.
- [33] M. E. Peskin and D. V. Schroeder, *An Introduction to quantum field theory*. 1995.
- [34] A. Pich, “The Standard model of electroweak interactions,” in *2004 European School of High-Energy Physics, Sant Feliu de Guixols, Spain, 30 May - 12 June 2004*, pp. 1–48. [arXiv:hep-ph/0502010](https://arxiv.org/abs/hep-ph/0502010) [hep-ph].
- [35] CMS, “Total integrated luminosity in 2016.” https://twiki.cern.ch/twiki/bin/view/CMSPublic/LumiPublicResults#2016_Proton_Proton_13_TeV_Collis, accessed 2017-04-24.
- [36] R. D. Ball *et al.*, “Parton distributions with LHC data,” *Nucl. Phys.* **B867** (2013) 244–289, [arXiv:1207.1303](https://arxiv.org/abs/1207.1303) [hep-ph].
- [37] J. Pumplin *et al.*, “New generation of parton distributions with uncertainties from global QCD analysis,” *JHEP* **07** (2002) 012, [arXiv:hep-ph/0201195](https://arxiv.org/abs/hep-ph/0201195) [hep-ph].
- [38] H.-L. Lai *et al.*, “New parton distributions for collider physics,” *Phys. Rev.* **D82** (2010) 074024, [arXiv:1007.2241](https://arxiv.org/abs/1007.2241) [hep-ph].
- [39] T. Kinoshita, “Mass singularities of Feynman amplitudes,” *J. Math. Phys.* **3** (1962) 650–677.
- [40] T. D. Lee and M. Nauenberg, “Degenerate Systems and Mass Singularities,” *Phys. Rev.* **133** (1964) B1549–B1562.
- [41] S. Catani and M. H. Seymour, “Jet cross-sections at next-to-leading order,” *Acta Phys. Polon.* **B28** 863–881, [arXiv:hep-ph/9612236](https://arxiv.org/abs/hep-ph/9612236) [hep-ph].
- [42] S. Catani and M. Seymour, “A General algorithm for calculating jet cross-sections in NLO QCD,” *Nucl. Phys.* **B485** (1997) 291–419, [arXiv:hep-ph/9605323](https://arxiv.org/abs/hep-ph/9605323) [hep-ph].
- [43] T. Binoth *et al.*, “A Proposal for a standard interface between Monte Carlo tools and one-loop programs,” *Comput. Phys. Commun.* **181** 1612–1622, [arXiv:1001.1307](https://arxiv.org/abs/1001.1307) [hep-ph].
- [44] S. Alioli *et al.*, “Update of the Binoth Les Houches Accord for a standard interface between Monte Carlo tools and one-loop programs,” *Comput. Phys. Commun.* **185** (2014) 560–571, [arXiv:1308.3462](https://arxiv.org/abs/1308.3462) [hep-ph].
- [45] M. Rauch and S. Plätzer, “Parton Shower Matching Systematics in Vector-Boson-Fusion WW Production,” *Eur. Phys. J.* **C77** no. 5, (2017) 293, [arXiv:1605.07851](https://arxiv.org/abs/1605.07851) [hep-ph].
- [46] J. Bellm, S. Gieseke, and S. Plätzer, “Merging NLO Multi-jet Calculations with Improved Unitarization,” [arXiv:1705.06700](https://arxiv.org/abs/1705.06700) [hep-ph].
- [47] T. Sjöstrand, “Status and developments of event generators,” *PoS LHCP2016* 007, [arXiv:1608.06425](https://arxiv.org/abs/1608.06425) [hep-ph].
- [48] V. V. Sudakov, “Vertex parts at very high-energies in quantum electrodynamics,” *Sov. Phys. JETP* **3** (1956) 65–71.

- [49] R. Jackiw, “Dynamics at high momentum and the vertex function of spinor electrodynamics,” *Annals Phys.* **48** (1968) 292–321.
- [50] M. Rubin, *A new LHC search channel for a light Higgs boson and associated QCD calculations*. PhD thesis, Paris, LPTHE, 2010.
- [51] S. Catani, F. Krauss, R. Kuhn, and B. R. Webber, “QCD matrix elements + parton showers,” *JHEP* **11** (2001) 063, [arXiv:hep-ph/0109231 \[hep-ph\]](#).
- [52] Y. L. Dokshitzer, G. D. Leder, S. Moretti, and B. R. Webber, “Better jet clustering algorithms,” *JHEP* **08** (1997) 001, [arXiv:hep-ph/9707323 \[hep-ph\]](#).
- [53] M. Wobisch and T. Wengler, “Hadronization corrections to jet cross-sections in deep inelastic scattering,” in *Monte Carlo generators for HERA physics. Proceedings, Workshop, Hamburg, Germany, 1998-1999*, pp. 270–279. [arXiv:hep-ph/9907280 \[hep-ph\]](#).
- [54] M. Rubin, G. P. Salam, and S. Sapeta, “Loopsim library.” <https://loopsim.hepforge.org>, 2015.
- [55] M. Cacciari, G. P. Salam, and G. Soyez, “FastJet User Manual,” *Eur. Phys. J.* **C72** (2012) 1896, [arXiv:1111.6097 \[hep-ph\]](#).
- [56] T. Appelquist and J. Carazzone, “Infrared Singularities and Massive Fields,” *Phys. Rev.* **D11** (1975) 2856.
- [57] J. Ambjorn, “On the Decoupling of Massive Particles in Field Theory,” *Commun. Math. Phys.* **67** (1979) 109.
- [58] E. B. Manoukian, “Generalized decoupling theorem in quantum field theory,” *J. Math. Phys.* **22** (1981) 2258–2262.
- [59] E. B. Manoukian, “On the decoupling theorem in field theory,” *J. Math. Phys.* **22** (1981) 572–573.
- [60] J. Brehmer, A. Freitas, D. Lopez-Val, and T. Plehn, “Pushing Higgs Effective Theory to its Limits,” *Phys. Rev.* **D93** no. 7, (2016) 075014, [arXiv:1510.03443 \[hep-ph\]](#).
- [61] E. Fermi, “Trends to a Theory of beta Radiation. (In Italian),” *Nuovo Cim.* **11** (1934) 1–19.
- [62] F. L. Wilson, “Fermi’s Theory of Beta Decay,” *Am. J. Phys.* **36** no. 12, (1968) 1150–1160.
- [63] **Gargamelle Neutrino**, F. J. Hasert *et al.*, “Observation of Neutrino Like Interactions Without Muon Or Electron in the Gargamelle Neutrino Experiment,” *Phys. Lett.* **46B** (1973) 138–140.
- [64] **UA1**, G. Arnison *et al.*, “Experimental Observation of Isolated Large Transverse Energy Electrons with Associated Missing Energy at $\sqrt{s} = 540$ GeV,” *Phys. Lett.* **122B** 103–116.
- [65] **UA1**, G. Arnison *et al.*, “Experimental Observation of Lepton Pairs of Invariant Mass Around 95 GeV/ c^2 at the CERN SPS Collider,” *Phys. Lett.* **126B** (1983) 398–410.

- [66] H. M. Georgi, S. L. Glashow, M. E. Machacek, and D. V. Nanopoulos, “Higgs Bosons from Two Gluon Annihilation in Proton Proton Collisions,” *Phys. Rev. Lett.* **40** (1978) 692.
- [67] M. Spira, A. Djouadi, D. Graudenz, and P. M. Zerwas, “Higgs boson production at the LHC,” *Nucl. Phys.* **B453** (1995) 17–82, [arXiv:hep-ph/9504378](#) [hep-ph].
- [68] S. Bentvelsen, E. Laenen, and P. Motylinski, “Higgs production through gluon fusion at leading order,” Tech. Rep. NIKHEF 007, 2005.
- [69] C. Anastasiou, C. Duhr, F. Dulat, F. Herzog, and B. Mistlberger, “Higgs Boson Gluon-Fusion Production in QCD at Three Loops,” *Phys. Rev. Lett.* **114** (2015) 212001, [arXiv:1503.06056](#) [hep-ph].
- [70] S. Weinberg, “Varieties of Baryon and Lepton Nonconservation,” *Phys. Rev.* **D22** (1980) 1694.
- [71] B. Henning, X. Lu, T. Melia, and H. Murayama, “2, 84, 30, 993, 560, 15456, 11962, 261485, ...: Higher dimension operators in the SM EFT,” [arXiv:1512.03433](#) [hep-ph].
- [72] W. Buchmuller and D. Wyler, “Effective Lagrangian Analysis of New Interactions and Flavor Conservation,” *Nucl. Phys.* **B268** (1986) 621–653.
- [73] B. Grzadkowski, M. Iskrzynski, M. Misiak, and J. Rosiek, “Dimension-Six Terms in the Standard Model Lagrangian,” *JHEP* **1010** (2010) 085, [arXiv:1008.4884](#) [hep-ph].
- [74] Z. Zhang, “Time to Go Beyond Triple-Gauge-Boson-Coupling Interpretation of W Pair Production,” *Phys. Rev. Lett.* **118** no. 1, (2017) 011803, [arXiv:1610.01618](#) [hep-ph].
- [75] T. Corbett, O. J. P. Éboli, and M. C. Gonzalez-Garcia, “Unitarity Constraints on Dimension-six Operators II: Including Fermionic Operators,” [arXiv:1705.09294](#) [hep-ph].
- [76] S. R. Coleman, J. Wess, and B. Zumino, “Structure of phenomenological Lagrangians,” *Phys. Rev.* **177** (1969) 2239–2247.
- [77] I. Brivio, “Higgs physics beyond the SM: the non-linear EFT approach,” *Nuovo Cim.* **C38** no. 4, 150, [arXiv:1505.00637](#) [hep-ph].
- [78] F. Feruglio, “The Chiral approach to the electroweak interactions,” *Int. J. Mod. Phys.* **A8** (1993) 4937–4972, [arXiv:hep-ph/9301281](#) [hep-ph].
- [79] T. Corbett, O. Eboli, J. Gonzalez-Fraile, and M. Gonzalez-Garcia, “Robust Determination of the Higgs Couplings: Power to the Data,” *Phys. Rev.* **D87** (2013) 015022, [arXiv:1211.4580](#) [hep-ph].
- [80] **CMS**, A. M. Sirunyan *et al.*, “Search for anomalous couplings in boosted $WW/WZ \rightarrow \ell\nu q\bar{q}$ production in proton-proton collisions at $\sqrt{s} = 8$ TeV,” [arXiv:1703.06095](#) [hep-ex].
- [81] K. Hagiwara, S. Ishihara, R. Szalapski, and D. Zeppenfeld, “Low-energy effects of new interactions in the electroweak boson sector,” *Phys. Rev.* **D48** (1993) 2182–2203.

- [82] V. Hankele, G. Klamke, D. Zeppenfeld, and T. Figy, “Anomalous Higgs boson couplings in vector boson fusion at the CERN LHC,” *Phys. Rev.* **D74** (2006) 095001, [arXiv:hep-ph/0609075](#) [hep-ph].
- [83] K. J. F. Gaemers and G. J. Gounaris, “Polarization Amplitudes for $e^+ e^- \rightarrow W^+ W^-$ and $e^+ e^- \rightarrow Z Z$,” *Z. Phys.* **C1** (1979) 259.
- [84] K. Hagiwara, R. D. Peccei, D. Zeppenfeld, and K. Hikasa, “Probing the Weak Boson Sector in $e^+ e^- \rightarrow W^+ W^-$,” *Nucl. Phys.* **B282** (1987) 253–307.
- [85] K. Hagiwara, J. Woodside, and D. Zeppenfeld, “Measuring the WWZ Coupling at the Tevatron,” *Phys. Rev.* **D41** (1990) 2113–2119.
- [86] R. S. Gupta, A. Pomarol, and F. Riva, “BSM Primary Effects,” *Phys. Rev.* **D91** no. 3, (2015) 035001, [arXiv:1405.0181](#) [hep-ph].
- [87] K. Hagiwara, S. Ishihara, R. Szalapski, and D. Zeppenfeld, “Low-energy constraints on electroweak three gauge boson couplings,” *Phys. Lett.* **B283** (1992) 353–359.
- [88] o. Degrande, “Effective Field Theory: A Modern Approach to Anomalous Couplings,” *Annals Phys.* **335** (2013) 21–32, [arXiv:1205.4231](#) [hep-ph].
- [89] O. Schlimpert, *Anomale Kopplungen bei der Streuung schwacher Eichbosonen*. Diploma thesis, KIT, 2013. https://www.itp.kit.edu/prep/diploma/PSFiles/Diplom_Schlimpert.pdf.
- [90] B. Feigl, *Anomale Vier-Vektorboson-Kopplungen bei der Produktion von drei Vektorbosonen am LHC*. Diploma thesis, KIT, 2009. https://www.itp.kit.edu/prep/diploma/PSFiles/Diplom_Feigl.pdf.
- [91] R. Contino, A. Falkowski, F. Goertz, C. Grojean, and F. Riva, “On the Validity of the Effective Field Theory Approach to SM Precision Tests,” *JHEP* **07** (2016) 144, [arXiv:1604.06444](#) [hep-ph].
- [92] F. Campanario, R. Roth, S. Sapeta, and D. Zeppenfeld, “Anomalous couplings in WZ production beyond NLO QCD,” *PoS LHCP2016* (2016) 141, [arXiv:1612.03577](#) [hep-ph].
- [93] A. Azatov, R. Contino, C. S. Machado, and F. Riva, “Helicity selection rules and noninterference for BSM amplitudes,” *Phys. Rev.* **D95** no. 6, (2017) 065014, [arXiv:1607.05236](#) [hep-ph].
- [94] A. Falkowski *et al.*, “Rosetta: an operator basis translator for Standard Model effective field theory,” *Eur. Phys. J.* **C75** no. 12, (2015) 583, [arXiv:1508.05895](#) [hep-ph].
- [95] G. F. Giudice, C. Grojean, A. Pomarol, and R. Rattazzi, “The Strongly-Interacting Light Higgs,” *JHEP* **06** (2007) 045, [arXiv:hep-ph/0703164](#) [hep-ph].
- [96] **LHC Higgs Cross Section Working Group**, D. de Florian *et al.*, “Handbook of LHC Higgs Cross Sections: 4. Deciphering the Nature of the Higgs Sector,” [arXiv:1610.07922](#) [hep-ph].
- [97] R. Alonso, E. E. Jenkins, A. V. Manohar, and M. Trott, “Renormalization Group Evolution of the Standard Model Dimension Six Operators III: Gauge Coupling Dependence and Phenomenology,” *JHEP* **04** (2014) 159, [arXiv:1312.2014](#) [hep-ph].

- [98] C. F. Perdrisat, V. Punjabi, and M. Vanderhaeghen, “Nucleon Electromagnetic Form Factors,” *Prog. Part. Nucl. Phys.* **59** (2007) 694–764, [arXiv:hep-ph/0612014](#) [hep-ph].
- [99] “VBFNLO utility to calculate form factors, version 1.3.0.” <https://www.itp.kit.edu/~vbfnlweb/wiki/doku.php?id=download:formfactor>, 2014.
- [100] B. Jager, L. Salfelder, M. Worek, and D. Zeppenfeld, “Physics Opportunities for Vector-Boson Scattering at a Future 100 TeV Hadron Collider,” [arXiv:1704.04911](#) [hep-ph].
- [101] A. Alboteanu, W. Kilian, and J. Reuter, “Resonances and Unitarity in Weak Boson Scattering at the LHC,” *JHEP* **11** (2008) 010, [arXiv:0806.4145](#) [hep-ph].
- [102] F. Campanario, M. Kerner, and D. Zeppenfeld, “ZA production in vector-boson scattering at next-to-leading order QCD,” [arXiv:1704.01921](#) [hep-ph].
- [103] M. Löschner, *Unitarisation of anomalous couplings in vector boson scattering*. Master thesis, KIT, 2014. https://www.itp.kit.edu/prep/diploma/PSFiles/Master_Max.pdf.
- [104] W. Kilian, T. Ohl, J. Reuter, and M. Sekulla, “High-Energy Vector Boson Scattering after the Higgs Discovery,” *Phys. Rev.* **D91** (2015) 096007, [arXiv:1408.6207](#) [hep-ph].
- [105] **ALEPH**, R. Barate *et al.*, “Measurement of the W pair cross-section in e+ e- collisions at 172-GeV,” *Phys. Lett.* **B415** (1997) 435–444.
- [106] **DELPHI, OPAL, LEP Electroweak, ALEPH, L3**, S. Schael *et al.*, “Electroweak Measurements in Electron-Positron Collisions at W-Boson-Pair Energies at LEP,” *Phys. Rept.* **532** (2013) 119–244, [arXiv:1302.3415](#) [hep-ex].
- [107] **D0**, V. M. Abazov *et al.*, “Measurement of the $p\bar{p} \rightarrow WZ + X$ cross-section at $\sqrt{s} = 1.96$ -TeV and limits on WWZ trilinear gauge couplings,” *Phys. Rev.* **D76** (2007) 111104, [arXiv:0709.2917](#) [hep-ex].
- [108] **CDF**, A. Abulencia *et al.*, “Observation of WZ Production,” *Phys. Rev. Lett.* **98** (2007) 161801, [arXiv:hep-ex/0702027](#) [hep-ex].
- [109] **CDF**, T. Aaltonen *et al.*, “Measurement of the WZ Cross Section and Triple Gauge Couplings in $p\bar{p}$ Collisions at $\sqrt{s} = 1.96$ TeV,” *Phys. Rev.* **D86** (2012) 031104, [arXiv:1202.6629](#) [hep-ex].
- [110] **D0**, V. M. Abazov *et al.*, “A measurement of the WZ and ZZ production cross sections using leptonic final states in 8.6 fb⁻¹ of $p\bar{p}$ collisions,” *Phys. Rev.* **D85** (2012) 112005, [arXiv:1201.5652](#) [hep-ex].
- [111] **CDF, D0**, T. Aaltonen *et al.*, “Evidence for a particle produced in association with weak bosons and decaying to a bottom-antibottom quark pair in Higgs boson searches at the Tevatron,” *Phys. Rev. Lett.* **109** (2012) 071804, [arXiv:1207.6436](#) [hep-ex].
- [112] **D0**, V. M. Abazov *et al.*, “Measurements of WW and WZ production in W + jets final states in $p\bar{p}$ collisions,” *Phys. Rev. Lett.* **108** (2012) 181803, [arXiv:1112.0536](#) [hep-ex].

- [113] **CDF**, T. Aaltonen *et al.*, “First Observation of Vector Boson Pairs in a Hadronic Final State at the Tevatron Collider,” *Phys. Rev. Lett.* **103** (2009) 091803, [arXiv:0905.4714](#) [hep-ex].
- [114] **ATLAS**, “Summary of standard model cross section measurements with fiducial cross section measurements and limits, compared to theory.” <https://twiki.cern.ch/twiki/bin/view/AtlasPublic/StandardModelPublicResults>, accessed 2017-04-24.
- [115] **ATLAS**, G. Aad *et al.*, “Measurement of WZ production in proton-proton collisions at $\sqrt{s} = 7$ TeV with the ATLAS detector,” *Eur. Phys. J.* **C72** (2012) 2173, [arXiv:1208.1390](#) [hep-ex].
- [116] **ATLAS**, G. Aad *et al.*, “Search for WZ resonances in the fully leptonic channel using pp collisions at $\sqrt{s} = 8$ TeV with the ATLAS detector,” *Phys. Lett.* **B737** (2014) 223–243, [arXiv:1406.4456](#) [hep-ex].
- [117] **ATLAS**, G. Aad *et al.*, “Measurements of $W^{\pm}Z$ production cross sections in pp collisions at $\sqrt{s} = 8$ TeV with the ATLAS detector and limits on anomalous gauge boson self-couplings,” *Phys. Rev.* **D93** no. 9, (2016) 092004, [arXiv:1603.02151](#) [hep-ex].
- [118] **ATLAS**, M. Aaboud *et al.*, “Measurement of the $W^{\pm}Z$ boson pair-production cross section in pp collisions at $\sqrt{s} = 13$ TeV with the ATLAS Detector,” *Phys. Lett.* **B762** (2016) 1–22, [arXiv:1606.04017](#) [hep-ex].
- [119] **CMS**, V. Khachatryan *et al.*, “Measurement of the WZ production cross section in pp collisions at $\sqrt{s} = 13$ TeV,” *Phys. Lett.* **B766** (2017) 268–290, [arXiv:1607.06943](#) [hep-ex].
- [120] **CMS**, V. Khachatryan *et al.*, “Measurement of the WZ production cross section in pp collisions at $\sqrt{s} = 7$ and 8 TeV and search for anomalous triple gauge couplings at $\sqrt{s} = 8$ TeV,” *Eur. Phys. J.* **C77** no. 4, (2017) 236, [arXiv:1609.05721](#) [hep-ex].
- [121] **CMS**, S. Chatrchyan *et al.*, “Measurement of the sum of WW and WZ production with W +dijet events in pp collisions at $\sqrt{s} = 7$ TeV,” *Eur. Phys. J.* **C73** no. 2, (2013) 2283, [arXiv:1210.7544](#) [hep-ex].
- [122] **ATLAS**, G. Aad *et al.*, “Search for resonant diboson production in the $WW/WZ \rightarrow l\nu jj$ decay channels with the ATLAS detector at $\sqrt{s} = 7$ TeV,” *Phys. Rev.* **D87** no. 11, (2013) 112006, [arXiv:1305.0125](#) [hep-ex].
- [123] **ATLAS**, G. Aad *et al.*, “Measurement of the $WW + WZ$ cross section and limits on anomalous triple gauge couplings using final states with one lepton, missing transverse momentum, and two jets with the ATLAS detector at $\sqrt{s} = 7$ TeV,” *JHEP* **01** (2015) 049, [arXiv:1410.7238](#) [hep-ex].
- [124] **CMS**, S. Chatrchyan *et al.*, “Measurement of WZ and ZZ production in pp collisions at $\sqrt{s} = 8$ TeV in final states with b-tagged jets,” *Eur. Phys. J.* **C74** no. 8, (2014) 2973, [arXiv:1403.3047](#) [hep-ex].
- [125] **ATLAS**, M. Aaboud *et al.*, “Measurement of $WW/WZ \rightarrow l\nu qq'$ production with the hadronically decaying boson reconstructed as one or two jets in pp collisions at $\sqrt{s} = 8$

- TeV with ATLAS, and constraints on anomalous gauge couplings,” [arXiv:1706.01702](#) [hep-ex].
- [126] **CMS**, S. Chatrchyan *et al.*, “Search for exotic resonances decaying into WZ/ZZ in pp collisions at $\sqrt{s} = 7$ TeV,” *JHEP* **02** (2013) 036, [arXiv:1211.5779](#) [hep-ex].
- [127] **CMS**, S. Chatrchyan *et al.*, “Search for a W' or Techni- ρ Decaying into WZ in pp Collisions at $\sqrt{s} = 7$ TeV,” *Phys. Rev. Lett.* **109** (2012) 141801, [arXiv:1206.0433](#) [hep-ex].
- [128] **ATLAS**, “Searches for heavy ZZ and ZW resonances in the $llqq$ and $vvqq$ final states in pp collisions at $\sqrt{s} = 13$ TeV with the ATLAS detector,” Tech. Rep. ATLAS-CONF-2016-082, 2016.
- [129] **CMS**, V. Khachatryan *et al.*, “Search for new resonances decaying via WZ to leptons in proton-proton collisions at $\sqrt{s} = 8$ TeV,” *Phys. Lett.* **B740** (2015) 83–104, [arXiv:1407.3476](#) [hep-ex].
- [130] **CMS**, A. M. Sirunyan *et al.*, “Search for massive resonances decaying into WW , WZ or ZZ bosons in proton-proton collisions at $\sqrt{s} = 13$ TeV,” *JHEP* **03** (2017) 162, [arXiv:1612.09159](#) [hep-ex].
- [131] **CMS**, A. M. Sirunyan *et al.*, “Combination of searches for heavy resonances decaying to WW , WZ , ZZ , WH , and ZH boson pairs in proton-proton collisions at $\sqrt{s} = 8$ and 13 TeV,” [arXiv:1705.09171](#) [hep-ex].
- [132] E. Masso and V. Sanz, “Limits on Anomalous Couplings of the Higgs to Electroweak Gauge Bosons from LEP and LHC,” *Phys. Rev.* **D87** no. 3, (2013) 033001, [arXiv:1211.1320](#) [hep-ph].
- [133] J. Ellis, V. Sanz, and T. You, “Complete Higgs Sector Constraints on Dimension-6 Operators,” *JHEP* **1407** (2014) 036, [arXiv:1404.3667](#) [hep-ph].
- [134] A. Butter, *et al.*, “The Gauge-Higgs Legacy of the LHC Run I,” *JHEP* **07** (2016) 152, [arXiv:1604.03105](#) [hep-ph].
- [135] G. P. Salam, “Perturbative QCD for the LHC,” *PoS ICHEP2010* 556, [arXiv:1103.1318](#) [hep-ph].
- [136] F. Campanario, M. Kerner, L. D. Ninh, and D. Zeppenfeld, “NLO QCD corrections to $WZJJ$ production at the LHC,” in *Proceedings, 9th Rencontres du Vietnam: Windows on the Universe: Quy Nhon, Vietnam, August 11-17, 2013*, pp. 201–204. [arXiv:1310.4369](#) [hep-ph].
- [137] F. Campanario, M. Kerner, L. D. Ninh, and D. Zeppenfeld, “Next-to-leading order QCD corrections to W^+W^+ and W^-W^- production in association with two jets,” *Phys. Rev.* **D89** no. 5, (2014) 054009, [arXiv:1311.6738](#) [hep-ph].
- [138] F. Campanario, M. Kerner, L. D. Ninh, and D. Zeppenfeld, “ WZ production in association with two jets at NLO in QCD,” *Phys. Rev. Lett.* **111** (2013) 052003, [arXiv:1305.1623](#) [hep-ph].
- [139] F. Campanario, M. Kerner, L. D. Ninh, and D. Zeppenfeld, “Next-to-leading order QCD corrections to ZZ production in association with two jets,” *JHEP* **07** (2014) 148, [arXiv:1405.3972](#) [hep-ph].

- [140] F. Campanario, M. Kerner, L. D. Ninh, and D. Zeppenfeld, “Next-to-leading order QCD corrections to $W\gamma$ production in association with two jets,” *Eur. Phys. J.* **C74** no. 5, (2014) 2882, [arXiv:1402.0505 \[hep-ph\]](#).
- [141] S. Höche, Y. Li, and S. Prestel, “Drell-Yan lepton pair production at NNLO QCD with parton showers,” *Phys. Rev.* **D91** no. 7, (2015) 074015, [arXiv:1405.3607 \[hep-ph\]](#).
- [142] A. Karlberg, E. Re, and G. Zanderighi, “NNLOPS accurate Drell-Yan production,” *JHEP* **09** (2014) 134, [arXiv:1407.2940 \[hep-ph\]](#).
- [143] A. Buckley *et al.*, “General-purpose event generators for LHC physics,” *Physics Reports* **504** no. 5, (2011) 145–233, [arXiv:1101.2599](#).
- [144] J. M. Campbell, “Theory overview of electroweak physics at hadron colliders,” in *4th Large Hadron Collider Physics Conference (LHCP 2016) Lund, Sweden, June 13-18, 2016*. [arXiv:1609.00844 \[hep-ph\]](#).
- [145] J. Ohnemus, “An order α_s calculation of hadronic $W^\pm Z$ production,” *Phys. Rev.* **D44** (1991) 3477–3489.
- [146] L. J. Dixon, Z. Kunszt, and A. Signer, “Vector boson pair production in hadronic collisions at order α_s : Lepton correlations and anomalous couplings,” *Phys. Rev.* **D60** (1999) 114037, [arXiv:hep-ph/9907305 \[hep-ph\]](#).
- [147] S. Ji-Juan, M. Wen-Gan, Z. Ren-You, and G. Lei, “Next-to-leading order QCD predictions for the hadronic WH +jet production,” *Phys. Rev.* **D81** (2010) 114037, [arXiv:1006.0279 \[hep-ph\]](#).
- [148] G. Luisoni, P. Nason, C. Oleari, and F. Tramontano, “ $HW^\pm/HZ + 0$ and 1 jet at NLO with the POWHEG BOX interfaced to GoSam and their merging within MiNLO,” *JHEP* **1310** (2013) 083, [arXiv:1306.2542 \[hep-ph\]](#).
- [149] M. Grazzini, S. Kallweit, D. Rathlev, and M. Wiesemann, “ $W^\pm Z$ production at hadron colliders in NNLO QCD,” *Phys. Lett.* **B761** (2016) 179–183, [arXiv:1604.08576 \[hep-ph\]](#).
- [150] M. Grazzini, S. Kallweit, D. Rathlev, and M. Wiesemann, “ $W^\pm Z$ production at the LHC: fiducial cross sections and distributions in NNLO QCD,” *JHEP* **05** (2017) 139, [arXiv:1703.09065 \[hep-ph\]](#).
- [151] T. Gehrmann and L. Tancredi, “Two-loop QCD helicity amplitudes for $q\bar{q} \rightarrow W^\pm\gamma$ and $q\bar{q} \rightarrow Z^0\gamma$,” *JHEP* **02** (2012) 004, [arXiv:1112.1531 \[hep-ph\]](#).
- [152] T. Gehrmann, A. von Manteuffel, and L. Tancredi, “The two-loop helicity amplitudes for $q\bar{q}' \rightarrow V_1 V_2 \rightarrow 4$ leptons,” *JHEP* **09** (2015) 128, [arXiv:1503.04812 \[hep-ph\]](#).
- [153] M. Grazzini, S. Kallweit, and D. Rathlev, “ZZ production at the LHC: fiducial cross sections and distributions in NNLO QCD,” *Phys. Lett.* **B750** (2015) 407–410, [arXiv:1507.06257 \[hep-ph\]](#).
- [154] M. Grazzini, S. Kallweit, and D. Rathlev, “ $W\gamma$ and $Z\gamma$ production at the LHC in NNLO QCD,” *JHEP* **07** (2015) 085, [arXiv:1504.01330 \[hep-ph\]](#).

- [155] T. Gehrmann *et al.*, “ W^+W^- Production at Hadron Colliders in Next to Next to Leading Order QCD,” *Phys. Rev. Lett.* **113** no. 21, (2014) 212001, [arXiv:1408.5243 \[hep-ph\]](#).
- [156] F. Cascioli *et al.*, “ZZ production at hadron colliders in NNLO QCD,” *Phys. Lett.* **B735** (2014) 311–313, [arXiv:1405.2219 \[hep-ph\]](#).
- [157] M. Grazzini, S. Kallweit, D. Rathlev, and A. Torre, “ $Z\gamma$ production at hadron colliders in NNLO QCD,” *Phys. Lett.* **B731** (2014) 204–207, [arXiv:1309.7000 \[hep-ph\]](#).
- [158] M. Grazzini, S. Kallweit, S. Pozzorini, D. Rathlev, and M. Wiesemann, “ W^+W^- production at the LHC: fiducial cross sections and distributions in NNLO QCD,” *JHEP* **08** (2016) 140, [arXiv:1605.02716 \[hep-ph\]](#).
- [159] S. Alioli, F. Caola, G. Luisoni, and R. Röntsch, “ZZ production in gluon fusion at NLO matched to parton-shower,” *Phys. Rev.* **D95** no. 3, (2017) 034042, [arXiv:1609.09719 \[hep-ph\]](#).
- [160] F. Caola, M. Dowling, K. Melnikov, R. Röntsch, and L. Tancredi, “QCD corrections to vector boson pair production in gluon fusion including interference effects with off-shell Higgs at the LHC,” *JHEP* **07** (2016) 087, [arXiv:1605.04610 \[hep-ph\]](#).
- [161] F. Caola, J. M. Henn, K. Melnikov, A. V. Smirnov, and V. A. Smirnov, “Two-loop helicity amplitudes for the production of two off-shell electroweak bosons in gluon fusion,” *JHEP* **06** (2015) 129, [arXiv:1503.08759 \[hep-ph\]](#).
- [162] F. Caola, K. Melnikov, R. Röntsch, and L. Tancredi, “QCD corrections to ZZ production in gluon fusion at the LHC,” *Phys. Rev.* **D92** no. 9, (2015) 094028, [arXiv:1509.06734 \[hep-ph\]](#).
- [163] F. Caola, K. Melnikov, R. Röntsch, and L. Tancredi, “QCD corrections to W^+W^- production through gluon fusion,” *Phys. Lett.* **B754** (2016) 275–280, [arXiv:1511.08617 \[hep-ph\]](#).
- [164] F. Caola, J. M. Henn, K. Melnikov, A. V. Smirnov, and V. A. Smirnov, “Two-loop helicity amplitudes for the production of two off-shell electroweak bosons in quark-antiquark collisions,” *JHEP* **11** (2014) 041, [arXiv:1408.6409 \[hep-ph\]](#).
- [165] J. Baglio, L. D. Ninh, and M. M. Weber, “Massive gauge boson pair production at the LHC: a next-to-leading order story,” *Phys. Rev.* **D88** (2013) 113005, [arXiv:1307.4331 \[hep-ph\]](#).
- [166] A. Bierweiler, T. Kasprzik, J. H. Kühn, and S. Uccirati, “Electroweak corrections to W-boson pair production at the LHC,” *JHEP* **11** (2012) 093, [arXiv:1208.3147 \[hep-ph\]](#).
- [167] A. Bierweiler, T. Kasprzik, and J. H. Kühn, “Electroweak accuracy in V-pair production at the LHC,” *PoS ICHEP2012* 078, [arXiv:1208.3404 \[hep-ph\]](#).
- [168] A. Bierweiler, T. Kasprzik, and J. H. Kühn, “Vector-boson pair production at the LHC to $\mathcal{O}(\alpha^3)$ accuracy,” *JHEP* **12** (2013) 071, [arXiv:1305.5402 \[hep-ph\]](#).
- [169] M. Schönherr, S. Kallweit, J. M. Lindert, S. Pozzorini, and P. Maierhöfer, “NLO QCD+EW for V+jets,” in *4th Large Hadron Collider Physics Conference (LHCP 2016) Lund, Sweden, June 13-18, 2016*. [arXiv:1609.01445 \[hep-ph\]](#).

- [170] B. Biedermann, A. Denner, S. Dittmaier, L. Hofer, and B. Jäger, “Next-to-leading-order electroweak corrections to the production of four charged leptons at the LHC,” *JHEP* **01** (2017) 033, [arXiv:1611.05338 \[hep-ph\]](#).
- [171] J. M. Campbell and R. K. Ellis, “An Update on vector boson pair production at hadron colliders,” *Phys. Rev.* **D60** (1999) 113006, [arXiv:hep-ph/9905386 \[hep-ph\]](#).
- [172] J. M. Campbell and R. K. Ellis, “Radiative corrections to Z b anti-b production,” *Phys. Rev.* **D62** (2000) 114012, [arXiv:hep-ph/0006304 \[hep-ph\]](#).
- [173] F. Campanario and S. Sapeta, “WZ production beyond NLO for high-pT observables,” *Phys. Lett.* **B718** (2012) 100–104, [arXiv:1209.4595 \[hep-ph\]](#).
- [174] F. Campanario, M. Rauch, and S. Sapeta, “ W^+W^- production at high transverse momenta beyond NLO,” *Nucl. Phys.* **B879** (2014) 65–79, [arXiv:1309.7293 \[hep-ph\]](#).
- [175] F. Campanario, M. Rauch, and S. Sapeta, “ZZ production at high transverse momenta beyond NLO QCD,” *JHEP* **08** (2015) 070, [arXiv:1504.05588 \[hep-ph\]](#).
- [176] J. Baglio *et al.*, “VBFNLO 3.0.” <https://github.com/vbfnlo/vbfnlo>, 2017.
- [177] S. Weinzierl, “Introduction to Monte Carlo methods,” [arXiv:hep-ph/0006269 \[hep-ph\]](#).
- [178] G. Dahlquist and A. Björck, *Numerical Methods in Scientific Computing: Volume 1*. Society for Industrial and Applied Mathematics, Philadelphia, PA, USA, 2008.
- [179] W. H. Press, S. A. Teukolsky, W. T. Vetterling, and B. P. Flannery, *Numerical Recipes 3rd Edition: The Art of Scientific Computing*. Cambridge University Press, New York, NY, USA, 3 ed., 2007.
- [180] D. Rauch, *Automated NLO Calculations with Massive Quarks in Herwig++*. Master thesis, KIT, 2014. <https://www.itp.kit.edu/prep/diploma/PSFiles/ms-thesis-daniel-rauch.pdf>.
- [181] A. D. Duff, *Heavy Higgs boson production via electroweak gauge boson fusion in association with two and three jets*. PhD thesis, Wisconsin U., Madison, 1993.
- [182] G. P. C. U. Lepage, “VEGAS: An Adaptive Multi-dimensional Integration Program,” *Cornell Preprint* no. CLNS-80/447, (1980) 30.
- [183] G. Peter Lepage, “A new algorithm for adaptive multidimensional integration,” *Journal of Computational Physics* **27** no. 2, (1978) 192–203.
- [184] T. Hahn, “CUBA: A Library for multidimensional numerical integration,” *Comput. Phys. Commun.* **168** (2005) 78–95, [arXiv:hep-ph/0404043 \[hep-ph\]](#).
- [185] K. Hagiwara and D. Zeppenfeld, “Amplitudes for Multiparton Processes Involving a Current at e^+e^- , e^+p , and Hadron Colliders,” *Nucl. Phys.* **B313** (1989) 560.
- [186] H. Murayama, I. Watanabe, and K. Hagiwara, “HELAS: HELicity amplitude subroutines for Feynman diagram evaluations,” Tech. Rep. KEK-91-11, 1992.
- [187] J. Alwall *et al.*, “MadGraph/MadEvent v4: The New Web Generation,” *JHEP* **0709** (2007) 028, [arXiv:0706.2334 \[hep-ph\]](#).

- [188] F. Campanario, “Towards pp \rightarrow VVjj at NLO QCD: Bosonic contributions to triple vector boson production plus jet,” *JHEP* **10** (2011) 070, arXiv:1105.0920 [hep-ph].
- [189] P. L’Ecuyer and R. Simard, “TestU01: A C Library for Empirical Testing of Random Number Generators,” *ACM Trans. Math. Softw.* **33** no. 4, (2007) 22:1–22:40.
- [190] G. Marsaglia, A. Zaman, and W. W. Tsang, “Toward a universal random number generator,” *Statistics & Probability Letters* **9** no. 1, (1990) 35–39.
- [191] I. Sobol, “On the distribution of points in a cube and the approximate evaluation of integrals,” *USSR Computational Mathematics and Mathematical Physics* **7** no. 4, (1967) 86–112.
- [192] P. Bratley and B. L. Fox, “Algorithm 659: Implementing sobol’s quasirandom sequence generator,” *ACM Trans. Math. Softw.* **14** no. 1, (1988) 88–100.
- [193] S. Vigna, “Further scramblings of marsaglia’s xorshift generators,” *Journal of Computational and Applied Mathematics* **315** (2017) 175–181.
- [194] S. Vigna, “xoroshiro+ / xorshift* / xorshift+ generators and the PRNG shootout.” <http://xoroshiro.di.unimi.it/>.
- [195] G. Marsaglia, “Xorshift RNGs,” *Journal of Statistical Software* **8** (2003) 1–6.
- [196] G. Marsaglia and A. Zaman, “The KISS generator,” tech. rep., Department of Statistics, University of Florida, 1993.
- [197] W. J. Morokoff and R. E. Caflisch, “Quasi-Monte Carlo Integration,” *Journal of Computational Physics* **122** (1995) 218–230.
- [198] L. Dagum and R. Menon, “OpenMP: an industry standard API for shared-memory programming,” *Computational Science & Engineering, IEEE* **5** no. 1, (1998) 46–55.
- [199] OpenMP Architecture Review Board, “OpenMP application program interface version 3.0,” 2008.
- [200] “MPI: A Message-Passing Interface Standard,” tech. rep., 1994.
- [201] “MPI: A Message-Passing Interface Standard. Version 3.0,” tech. rep., 2015. <http://www.mpi-forum.org/docs/>, accessed 2017-04-24.
- [202] R. Kreckel, “Parallelization of adaptive MC integrator,” *Computer Physics Communications* **106** no. 3, (1997) 258–266.
- [203] W. Kahan, “Pracniques: Further remarks on reducing truncation errors,” *Commun. ACM* **8** no. 1, (1965) 40.
- [204] N. J. Higham, “The accuracy of floating point summation,” *SIAM Journal on Scientific Computing* **14** no. 4, (1993) 783–799.
- [205] E. Gabriel *et al.*, “Open MPI: Goals, concept, and design of a next generation MPI implementation,” in *Proceedings, 11th European PVM/MPI Users’ Group Meeting*, pp. 97–104. Budapest, Hungary, 2004.
- [206] J. M. Campbell, R. K. Ellis, and W. T. Giele, “A Multi-Threaded Version of MCFM,” *Eur. Phys. J.* **C75** no. 6, (2015) 246, arXiv:1503.06182 [physics.comp-ph].

- [207] W. Kilian, T. Ohl, and J. Reuter, “WHIZARD: Simulating Multi-Particle Processes at LHC and ILC,” *Eur. Phys. J.* **C71** (2011) 1742, arXiv:0708.4233 [hep-ph].
- [208] M. Moretti, T. Ohl, and J. Reuter, “O’Mega: An Optimizing matrix element generator,” arXiv:hep-ph/0102195 [hep-ph].
- [209] T. Ohl, “Vamp, version 1.0: Vegas amplified: Anisotropy, multi-channel sampling and parallelization.” https://twiki.cern.ch/twiki/bin/view/CMSPublic/LumiPublicResults#2016_Proton_Proton_13_TeV_Collis, accessed 2017-04-24.
- [210] K. Hagiwara, J. Kanzaki, Q. Li, N. Okamura, and T. Stelzer, “Fast computation of MadGraph amplitudes on graphics processing unit (GPU),” *Eur. Phys. J.* **C73** (2013) 2608, arXiv:1305.0708 [physics.comp-ph].
- [211] G. M. Amdahl, “Validity of the single processor approach to achieving large scale computing capabilities,” in *Proceedings of the April 18-20, 1967, Spring Joint Computer Conference*, AFIPS ’67 (Spring), pp. 483–485. ACM, New York, NY, USA.
- [212] C.-C. Wu, C.-T. Yang, K.-C. Lai, and P.-H. Chiu, “Designing parallel loop self-scheduling schemes using the hybrid mpi and openmp programming model for multi-core grid systems,” *The Journal of Supercomputing* **59** no. 1, (2012) 42–60.
- [213] A. T. Chronopoulos, S. Penmatsa, N. Yu, and D. Yu, “Scalable loop self-scheduling schemes for heterogeneous clusters,” *International Journal of Computational Science and Engineering* **1** no. 2-4, (2005) 110–117.
- [214] J. Bellm, *NLO-QCD-Korrekturen zur WZ- und $W\gamma$ -Produktion am LHC*. Diploma thesis, KIT, 2012. http://www.itp.kit.edu/prep/diploma/PSFiles/Diplom_Bellm.pdf.
- [215] F. Campanario, C. Englert, S. Kallweit, M. Spannowsky, and D. Zeppenfeld, “NLO QCD corrections to WZ+jet production with leptonic decays,” *JHEP* **1007** (2010) 076, arXiv:1006.0390 [hep-ph].
- [216] C. Englert, *Next-to-Leading Order Corrections to $W\gamma + jet$ and $WZ + jet$ Production at Hadron Colliders*. Phd thesis, KIT, 2010. https://www.itp.kit.edu/prep/phd/PSFiles/Diss_Englert.pdf.
- [217] M. Dobbs and J. B. Hansen, “The HepMC C++ Monte Carlo event record for High Energy Physics,” *Comput. Phys. Commun.* **134** (2001) 41–46.
- [218] J. Alwall *et al.*, “A Standard format for Les Houches event files,” *Comput. Phys. Commun.* **176** (2007) 300–304, arXiv:hep-ph/0609017 [hep-ph].
- [219] F. Campanario, R. Roth, and D. Zeppenfeld, “QCD radiation in WH and WZ production and anomalous coupling measurements,” *Phys. Rev.* **D91** (2015) 054039, arXiv:1410.4840 [hep-ph].
- [220] R. Roth, *NLO QCD corrections to WH + jet production at the LHC*. Diploma thesis, KIT, 2013. http://www.itp.kit.edu/prep/diploma/PSFiles/Diplom_Roth.pdf.
- [221] F. Campanario, C. Englert, and M. Spannowsky, “QCD corrections to non-standard WZ+jet production with leptonic decays at the LHC,” *Phys. Rev.* **D82** (2010) 054015, arXiv:1006.3090 [hep-ph].

- [222] M. Cacciari, G. P. Salam, and G. Soyez, “The Anti-k(t) jet clustering algorithm,” *JHEP* **0804** (2008) 063, [arXiv:0802.1189](#) [hep-ph].
- [223] F. Campanario, C. Englert, and M. Spannowsky, “Precise predictions for (non-standard) $W\gamma$ + jet production,” *Phys. Rev.* **D83** (2011) 074009, [arXiv:1010.1291](#) [hep-ph].
- [224] M. Cacciari and G. P. Salam, “Dispelling the N^3 myth for the k_t jet-finder,” *Phys. Lett.* **B641** (2006) 57–61, [arXiv:hep-ph/0512210](#) [hep-ph].
- [225] R. H. Dalitz, “On the analysis of tau-meson data and the nature of the tau-meson,” *Phil. Mag. Ser.7* **44** (1953) 1068–1080.
- [226] J. Nuber, *Jet-vetoets in WH/WZ production events*. Bachelor thesis, KIT, 2016.
- [227] U. Baur, T. Han, and J. Ohnemus, “QCD corrections to hadronic $W\gamma$ production with nonstandard $WW\gamma$ couplings,” *Phys. Rev.* **D48** (1993) 5140–5161, [arXiv:hep-ph/9305314](#) [hep-ph].
- [228] F. J. Tackmann, J. R. Walsh, and S. Zuberi, “Resummation Properties of Jet Vetoes at the LHC,” *Phys. Rev.* **D86** (2012) 053011, [arXiv:1206.4312](#) [hep-ph].
- [229] G. Luisoni and S. Marzani, “QCD resummation for hadronic final states,” *J. Phys.* **G42** no. 10, (2015) 103101, [arXiv:1505.04084](#) [hep-ph].
- [230] X. Liu and F. Petriello, “Resummation of jet-veto logarithms in hadronic processes containing jets,” *Phys. Rev.* **D87** no. 1, (2013) 014018, [arXiv:1210.1906](#) [hep-ph].
- [231] S. Dawson, P. Jaiswal, Y. Li, H. Ramani, and M. Zeng, “Resummation of jet veto logarithms at N^3LL_a + NNLO for W^+W^- production at the LHC,” *Phys. Rev.* **D94** no. 11, (2016) 114014, [arXiv:1606.01034](#) [hep-ph].
- [232] C. F. Berger, C. Marcantonini, I. W. Stewart, F. J. Tackmann, and W. J. Waalewijn, “Higgs Production with a Central Jet Veto at NNLL+NNLO,” *JHEP* **04** (2011) 092, [arXiv:1012.4480](#) [hep-ph].
- [233] I. W. Stewart and F. J. Tackmann, “Theory Uncertainties for Higgs and Other Searches Using Jet Bins,” *Phys. Rev.* **D85** (2012) 034011, [arXiv:1107.2117](#) [hep-ph].
- [234] A. Banfi, G. P. Salam, and G. Zanderighi, “NLL+NNLO predictions for jet-veto efficiencies in Higgs-boson and Drell-Yan production,” *JHEP* **1206** (2012) 159, [arXiv:1203.5773](#) [hep-ph].
- [235] S. Gieseke, T. Kasprzik, and J. H. Kühn, “Vector-boson pair production and electroweak corrections in HERWIG++,” *Eur. Phys. J.* **C74** no. 8, (2014) 2988, [arXiv:1401.3964](#) [hep-ph].

Acknowledgements

First and foremost, I would like to thank Prof. Dieter Zeppenfeld for the opportunity to work with him and for advising me during this work. The discussions with him were very fruitful and his experienced guidance was an invaluable contribution to this thesis. Thank you also for giving me the opportunity to present this work at international conferences and attend summer schools.

I thank Prof. Matthias Steinhauser for being the second referee of this thesis.

I'd like to thank Francisco Campanario for his collaboration and continued support throughout my PhD time. His contributions to our common publications and quick and detailed feedback was greatly appreciated.

I am thankful to Michael Rauch for answering many questions and for his comments during this work as well as his expert knowledge and support regarding VBFNLO and LoopSim.

For the work with LoopSim, Sebastian Sapeta gave many insights into the implementation and interpretation of the results, for which I want to thank him.

For proof-reading this thesis and helpful comments I am grateful to Alexander Wlotzka, Marco Sekulla, Michael Rauch and Francisco Campanario.

Many people contributed to VBFNLO and thereby enabled this work. I would like to thank the people who, in addition to those previously mentioned, introduced me to the VBFNLO codebase and whose code I reused, especially Johannes Bellm, Bastian Feigl, Matthias Kerner, Oliver Schlimpert and Christoph Englert.

I enjoyed my time at the ITP and I would like to thank all current and former colleagues for creating a pleasant atmosphere. I appreciated the many hours spent discussing physics and other topics especially also with my office mates, Alexander Wlotzka, Martin Gabelmann and Philipp Basler. I am also glad for the chance to discuss with many colleagues of the neighboring institutes and the graduate school and their valuable input. I am grateful to the current and former system administrators of ITP and TTP, who I had the honor to work with and learn from, while jointly battling bugs and trying to keep the IT-infrastructure running smoothly.

This work was partially supported by the “Graduiertenkolleg GRK 1694: Elementarteilchenphysik bei höchster Energie und höchster Präzision” and the “Landesgraduiertenförderung” of Baden-Württemberg.

All this would not have been possible without the continued support of my family, friends and especially Dorothea, who always had my back and supported me through all phases of my studies and the PhD.